Investigation of Current Induced Spin Polarization in III-V Semiconductor Epilayers

by

Marta Luengo-Kovac

A dissertation submitted in partial fulfillment
of the requirements for the degree of
Doctor of Philosophy
(Physics)
in the University of Michigan
2017

Doctoral committee:

Associate Professor Vanessa Sih, Chair
Professor Rachel S. Goldman
Assistant Professor Emmanouil Kioupakis
Professor Çagliyan Kurdak
Professor Roberto D. Merlin

Marta Luengo-Kovac

mluengo@umich.edu

ORCID iD: 0000-0003-4215-6284

© Marta Luengo-Kovac 2017

Acknowledgements

First, I would like to thank my advisor, Vanessa Sih, for the mentorship and opportunities she provided these last six years. I could not have asked for a more supportive advisor.

I appreciate all of the members of the group who taught me so much about research. For the work covered in this thesis, I am particularly grateful to Ben Norman and Chris Trowbridge for all their help in learning the experiment. I would also like to thank Brennan Pursley, for introducing me to research in this lab, and Michael MacMahon, for invaluable discussions. Although my research on quantum dots is not included in this thesis, I would like to thank Tim Saucer and Jieun Lee for all their help on that project. Best of luck to Xinlin Song, Joe Iafrate, and Spencer Batalden.

The work in this thesis could not have been done without the members of Professor Goldman's group who grew and characterized the samples: Simon Huang, Davide Del Gaudio, and Jordan Occena. I am also grateful to Roberto Raimondi, for all his theoretical discussion.

I would like to thank my committee members, Professors Emmanouil Kioupakis, Çagliyan Kurdak, and Roberto Merlin for their advice and help. In particular, I would like to thank Professor Goldman for her collaboration and guidance throughout the years.

Lastly, I would like to thank my family, especially my parents and my sisters, for their love, and Uttam, for his unwavering support and companionship.

This dissertation contains work supported by the Air Force Office of Scientific Research,

the National Science Foundation Award DMR 1607779, Materials Research Science and Engineering Center Program DMR 1120923, and the Rackham Graduate School. Sample fabrication was performed in the Lurie Nanofabrication Facility.

Contents

Acknowledgements **ii**

List of Figures **vii**

List of Tables **ix**

Abstract **x**

Chapter 1 Introduction **1**

1.1 Motivation 1

1.2 Organization 3

Chapter 2 Electronic and Optical Properties of Semiconductors **4**

2.1 Introduction 4

2.2 GaAs Crystal Structure 5

2.3 GaAs Bandstructure 6

2.3.1 Tight Binding Model 7

2.4 Optical Selection Rules 10

2.5 Faraday Rotation 13

2.5.1 Complex Permittivity Near the Band Edge 15

2.5.2 Circular Birefringence 16

2.6 Conclusion 18

Chapter 3 Spins in Semiconductors 19

3.1 Introduction 19

3.2 Spin Dynamics in Semiconductors 20

3.3 Spin-Orbit Fields 21

3.3.1 Bulk and Structural Inversion Asymmetry 21

3.3.2 Biaxial and Uniaxial Strain 23

3.3.3 Determining the Spin-Orbit Parameters 24

3.4 Spin Relaxation and Dephasing 27

3.4.1 D'yakonov-Perel' Dephasing 29

3.4.2 Elliot-Yafet Dephasing 30

3.4.3 Temperature Dependence 31

3.5 Spin Polarization Mechanisms 32

3.6 Conclusion 34

Chapter 4 Experimental Methods 35

4.1 Introduction 35

4.2 Materials and Sample Fabrication 36

4.3 Pump-Probe Optical Setup 38

4.4 Time-Resolved Faraday Rotation 44

4.5 Resonant Spin Amplification 44

4.6 Spin Drag for Measurement of the Spin-Orbit Fields 45

4.7 Current-Induced Spin Polarization Measurements 49

4.7.1 Converting Faraday rotation to spin densities 50

4.8 Hall and Van der Pauw Measurements 53

4.9 Conclusion 56

Chapter 5 Voltage Dependent g-Factor **57**
5.1 Motivation 57
5.2 Sample Structure and Experimental Methods 59
5.3 Temperature Dependence 65
5.3.1 Photoluminescence Measurements 65
5.4 Conclusion 68

Chapter 6 Current-Induced Spin Polarization as a Function of Indium and Doping Concentrations **69**
6.1 Motivation 69
6.2 Sample Structure and Experimental Methods 70
6.3 Current-Induced Spin Polarization vs Spin-Orbit Coupling 74
6.4 Current-Induced Spin Polarization vs Material Parameters 74
6.5 Current-Induced Spin Polarization in GaAs 77
6.6 Spin Dephasing Mechanisms 78
6.7 Proposed Spin Polarization Mechanisms 80
6.7.1 Edelstein Effect 80
6.7.2 Spin Polarization from a Spin Hall Current 81
6.7.3 Current-Induced Spin Polarization from Extrinsic Contributions 87
6.8 Conclusion and Future Work 92

Bibliography **95**

List of Figures

2.1 Unit cell for the zinc-blende crystal structure of GaAs 6

2.2 Tight binding calculations of the bandstructure of GaAs 9

2.3 Optical selection rules for transitions between the valence band and conduction band in III-V semiconductors 12

2.4 Faraday rotation in GaAs 17

3.1 Vector plot of the spin-orbit field for different momentum directions and for different values of $r = \alpha'/\beta'$ 25

3.2 Schematic of D'yakonov-Perel' and Elliot-Yafet dephasing mechanisms 30

4.1 Schematic of the cross-shaped channel 38

4.2 Simplified schematic for the optical setup used in pump-probe measurements 39

4.3 Faraday rotation as a function of the position of the pump relative to the probe 40

4.4 Two dimensional spatial scan of the Kerr rotation on a sample patterned with a cross channel 41

4.5 Time-resolved Faraday rotation and resonant spin amplification 43

4.6 Spin drag measurements 47

4.7 Fits for the spin orbit fields 48

4.8 Current induced spin polarization 51

4.9 Hall measurements with a Hall bar and cross channel 54

4.10 Mobility and carrier concentration of GaAs as a function of temperature 55

5.1 Channel geometry and magnetic field scans 59
5.2 Spin drag fits of the SO field and g factor 61
5.3 g factor and SO fields as a function of drift velocity 62
5.4 g factor versus temperature 64
5.5 Photoluminescence as a function of temperature and voltage 66

6.1 η (CISP) vs. κ (SO splitting) for all five InGaAs samples 75
6.2 CISP vs material parameters 76
6.3 CISP in GaAs 77
6.4 Temperature dependent fits of the spin dephasing rate 79
6.5 Spin polarization from a spin Hall current 82
6.6 Comparison of spin polarization from a spin Hall current to data 85
6.7 Dynamic nuclear polarization measurements 87
6.8 Comparison of CISP theory and experiment 89
6.9 Spin generation rate vs. carrier concentration 90
6.10 Spin generation rate vs. mobility 91
6.11 Spin generation rate vs. q and r 92

List of Tables

6.1 Material parameters for the InGaAs and GaAs samples 71

6.2 SO parameters and spin dephasing times for InGaAs and GaAs samples 73

6.3 Conversion between electrically induced spin density and Faraday angle for InGaAs samples 73

6.4 Material parameters for the InGaAs samples used to calculate the predicted electrical spin generation efficiency. 90

Abstract

In the development of a semiconductor spintronics device, a thorough understanding of spin dynamics in semiconductors is necessary. In particular, electrical control of electron spins is advantageous for its compatibility with present day electronics. In this thesis, we will discuss the electrical modification of the electron g-factor, which characterizes the strength of the interaction between a spin and a magnetic field, as well as investigate electrically generated spin polarizations as a function of various material parameters.

We report on the modification of the electron g-factor by an in-plane electric field in an $In_{0.03}Ga_{0.97}As$ epilayer. We performed external magnetic field scans of the Kerr rotation of the InGaAs film in order to measure the g-factor independently of the spin-orbit fields. The g-factor increases from -0.4473 $\pm$ 0.0001 at 0 V/cm to -0.4419 $\pm$ 0.0001 at 50 V/cm applied along the [110] crystal axis. A comparison of temperature and voltage dependent photoluminescence measurements indicate that minimal channel heating occurs at these voltages. Possible explanations for this g-factor modification are discussed, including an increase in the electron temperature that is independent of the lattice temperature and the modification of the donor-bound electron wave function by the electric field.

The current-induced spin polarization and momentum-dependent spin-orbit field were measured in $In_xGa_{1-x}As$ epilayers with varying indium concentrations and silicon doping densities. Samples with higher indium concentrations and carrier concentrations and lower mobilities were found to have larger electrical spin generation efficiencies. Furthermore,

current-induced spin polarization was detected in GaAs epilayers despite the absence of measurable spin-orbit fields, indicating that the spin polarization mechanism is extrinsic. Temperature-dependent measurements of the spin dephasing rates and mobilities were used to characterize the relative strengths of the intrinsic D'yakonov-Perel' and extrinsic Elliot-Yafet spin dephasing mechanisms. Proposed spin polarization mechanisms are discussed and compared with the experimental results.

Chapter 1

Introduction

1.1 Motivation

The idea of a spinning electron was proposed by Uhlenbeck and Goudsmit (who would both later come to the University of Michigan) in order to explain the fine structure of atomic spectra [1]. Although it turns out electrons are not literally spinning, they do carry an intrinsic angular momentum that is crucial in the explanation of many physical phenomena.

Since an electron has a spin of 1/2, it is a 2-state system consisting of a "spin-up" and a "spin-down" state. An electron's spin can therefore potentially be used to encode binary code. This idea led to the development of the field of spintronics, which has resulted in the proposal and implementation of several spin-based alternatives to traditional computing components.

One of the earliest developments in the field of spintronics was the discovery of giant magnetoresistance (GMR) in 1988, for which Grünberg and Fert received the Nobel prize in 2007 [2, 3]. Most commercially available spintronic devices, in particular hard drive read-heads and MRAM, make use of GMR. These devices are based on ferromagnetic materials. The use of semiconductors for spintronics has been of interest since the proposal of a spin

field effect transistor by Datta and Das [4]. An all-electrical, all-semiconductor spin field effect transistor was demonstrated recently [5].

Spin-based devices can offer several advantages over traditional charge-based devices. Dynamic random access memory (DRAM) makes up the majority of the memory in present-day computers. DRAM uses capacitors to store information; since capacitors discharge over time, the information must be refreshed several times a second, leading to high power consumption. Furthermore, DRAM is a volatile memory, so the information must be transferred to a different, long-term memory, such as the hard drive, before powering off the computer. On the other hand, a spin-based memory such as MRAM does not need to be refreshed and is non-volatile [6], while still having read and write times comparable to DRAM, making it suitable both for short-term and long-term memory [7].

Although commercially available spintronic devices are based on magnetic materials, an all-electrical, all-semiconductor device would be advantageous for its compatibility with complementary metal-oxide-semiconductor (CMOS) devices. Furthermore, semiconductor materials can be designed to control the properties of the electrons, such as the effective mass, density, and g-factor.

Such a spintronic device will require the electrical manipulation and generation of electron spin polarizations in semiconductors. In this dissertation, we will demonstrate electrical modification of the electron g-factor in InGaAs. We will also investigate current-induced spin polarization, in which an in-plane electric field produces a bulk spin polarization, in InGaAs and GaAs epilayers. Previous measurements showed that the crystal axes with the largest spin-orbit coupling had the smallest amount of spin polarization [8], contrary to predictions that the current-induced spin polarization should be proportional to the spin-orbit coupling [9]. Thus, the polarization mechanism remains an open question. We will investigate the effect of indium concentration and carrier concentration on the magnitude of the current-induced spin polarization. We will explore various proposed spin polarization

mechanisms in the context of the experimental results.

1.2 Organization

Chapter 2 will discuss the electronic and optical properties of III-V zinc-blende semiconductors. We will explain how these properties can be used to optically inject and detect a spin polarization. Chapter 3 will discuss spin dynamics in semiconductors, including spin-orbit coupling, spin dephasing, and spin polarization mechanisms. Chapter 4 will cover the experimental methods, beginning with the materials and sample fabrication, then the optical pump-probe measurements, and finally the electrical characterization of the samples. In Chapter 5, we demonstrate the modification of the electron g-factor in InGaAs epilayers by an electric field. In Chapter 6, we investigate the relationship between current-induced spin polarization and the spin-orbit fields in InGaAs and GaAs samples with varying indium and carrier concentrations. Since the mechanism behind CISP is still unknown, we will compare the results of our measurements to the predictions of proposed spin polarization mechanisms.

Chapter 2

Electronic and Optical Properties of Semiconductors

2.1 Introduction

The vast majority of commercial semiconductor devices are fabricated from silicon. However, gallium arsenide offers several advantages for certain applications. For example, GaAs has a negative differential resistance above a certain threshold voltage, resulting in high-frequency oscillations in current known as the Gunn effect [10] that can be used for microwave generation. Furthermore, GaAs has a direct bandgap, and absorbs and emits light much more efficiently than silicon, which has an indirect bandgap. Therefore, GaAs is of interest for optoelectronic applications, such as solar cells [11] and laser diodes [12].

In this chapter, we will discuss the crystal structure of GaAs. From that, we will calculate the structure of the energy bands in GaAs, which will also give us insight into the optical properties of GaAs. Finally, we will show how these optical properties can be used to both inject and measure a spin polarization in GaAs.

2.2 GaAs Crystal Structure

Semiconductors formed from a single element from Group IV of the periodic table (so called because the elements have four valence electrons) such as C, Si, and Ge form a diamond crystal structure, which consists of a face centered cubic (fcc) lattice with a two-atom basis.

If instead of two Group IV atoms per basis, we have one Group III and one Group V atom, the structure is now referred to as a zinc-blende crystal (Fig. 2.1), and the material may be referred to as a III-V semiconductor. For example, instead of two Si atoms, the basis may consist of one Ga and one As atom. This is the same crystal structure as Si, except the sites on the crystal lattice are alternately occupied by Ga and As atoms. The diamond lattice has inversion symmetry about a point halfway along the bond between two adjacent atoms. However, this inversion symmetry is broken when the adjacent atoms are not identical and the crystal structure of GaAs, unlike Si, is said to have bulk inversion asymmetry (BIA). This becomes important for the discussion of spin-orbit effects (Ch. 3).

Ternary semiconductor alloys, like $Al_xGa_{1-x}As$ and $In_xGa_{1-x}As$, have material parameters, such as the lattice constant, bandgap, and effective masses, that are in between the material parameters of the two constituent semiconductors. The lattice constant of the alloy is given by a linear interpolation of the endpoint values, i.e. a "rule of mixtures", often termed Vegard's law [13]:

$$a_{\text{alloy}} = x a_A + (1-x) a_B \tag{2.1}$$

where $a_{A,B}$ are the lattice constants of the two materials being alloyed together, and x is the composition of A relative to B.

The bandgap of the alloy is generally also a linear superposition of the bandgaps of the component materials, although in certain cases there may be a deviation from a linear interpolation, called "bowing", i.e. the bandgap has a quadratic dependence on the

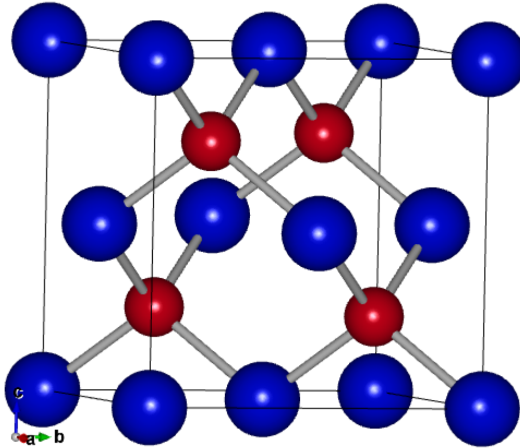

Figure 2.1: Unit cell for the zinc-blende crystal structure of GaAs. Blue and red spheres represent gallium and arsenic atoms respectively. Figure generated using Vesta software.

composition [14].

Most of the samples studied in this thesis are $In_xGa_{1-x}As$ alloys, where $x = 0.02 - 0.026$. This alloy has a lattice constant slightly larger than that of GaAs, with a misfit of 0.14% - 0.19%. The bandgap of the alloy is also slightly smaller than that of GaAs, by 22 meV - 28 meV. The effects of this are discussed in Section 4.2.

2.3 GaAs Bandstructure

The wavefunctions of the electrons in a semiconductor may be described by Schrödinger's equation:

$$\left[\frac{\hbar^2}{2m_0}\nabla^2 + U(\mathbf{r})\right]\psi(\mathbf{r}) = E\psi(\mathbf{r}) \tag{2.2}$$

where $U(\mathbf{r})$ is the potential. In a crystal structure such as a semiconductor, this potential is due to the lattice and is therefore periodic. Because of this, Bloch's theorem states that

the wavefunction of the electrons can be written as [15]

$$\psi_{\mathbf{k}}(\mathbf{r}) = e^{i\mathbf{k}\cdot\mathbf{r}} u_{\mathbf{k}}(\mathbf{r}) \tag{2.3}$$

where $u_{\mathbf{k}}(\mathbf{r})$ has the same periodicity as the potential, and $\mathbf{k}$ is the crystal momentum. This means that the wavefunction of an electron is an envelope function multiplied by a periodic function. In order to understand the behavior of an electron in a crystal, one need only calculate the envelope function, significantly simplifying calculations. This result also means that, given a perfectly periodic potential (i.e. no deformations or impurities), an electron will propagate without scattering.

Another consequence of the periodic potential is the appearance of an energy band gap. Because of the periodic boundary conditions, there are certain electron energies for which there are no solutions to the Schrödinger equation. The specific energy bandstructure for GaAs, including this bandgap, will be calculated in the next section using the tight-binding model.

2.3.1 Tight Binding Model

The tight binding model allows for the calculation of the bandstructure of a semiconductor starting from the wavefunctions for the individual atoms in that semiconductor. The Hamiltonian is assumed to be the sum of the Hamiltonians of each individual atom, plus some small correction in the regions where there is significant overlap in the wavefunctions from neighboring atoms:

$$H(\mathbf{r}) = \sum_{\mathbf{R}_n} H_{\mathrm{atom}}(\mathbf{r} - \mathbf{R}_n) + \Delta U(\mathbf{r}) \tag{2.4}$$

If the atoms in this crystal were completely independent ($\Delta U(\mathbf{r}) = 0$), then the electronic

wavefunctions could be written as a sum of the independent atomic orbitals:

$$\Psi_{\mathbf{k}}(\mathbf{r}) = \sum_{\mathbf{R}_n} a_n(\mathbf{R}_n)\psi_{\text{atom}}(\mathbf{r} - \mathbf{R}_n) \tag{2.5}$$

In order to satisfy Bloch's theorem, we must have $a_n(\mathbf{R}_n) = e^{i\mathbf{k}\cdot\mathbf{R}_n}$.

If, instead, we have a nonzero $\Delta U(\mathbf{r})$, we can replace the atomic wavefunctions in equation 2.5 with a linear combination of atomic orbitals, called Löwdin functions [16]:

$$\phi(\mathbf{r}) = \sum_{n=1}^{N} b_n \psi_{n,\text{atom}}(\mathbf{r}) \tag{2.6}$$

With some knowledge of the atomic structure of the individual atoms in the crystal, we can decide which atomic wavefunctions to sum over. For example, the valence electrons for Ga are $4s^2 4p^1$ and for As are $4s^2 4p^3$, so for calculations for GaAs we will choose an atomic basis with 16 functions: s, p_x, p_y, and p_z for each of the two basis atoms, times two to account for spin up and spin down electrons.

We can plug equations 2.4, 2.5, and 2.6 into Schrödinger's equation to give us an equation for the energies and wavefunctions. This equation cannot generally be solved analytically, except in very simple cases (e.g. only considering a single atomic s-level) or at high-symmetry points (e.g the Γ-point for the fcc lattice) [17]. Usually, the relevant matrix elements are not determined from first principles, but are left as fitting parameters matched to experimental data [18]. The bandstructure of GaAs, including the conduction and valence bands, is shown in Fig. 2.2.

If the tight-binding model is applied to GaAs, it turns out that the bottom of the conduction band is purely s-like ($l = 0$), and the top of the valence band is purely p-like ($l = 1$) (Fig. 2.2, right). If we include the spin of the electron, the total angular momentum of the system is $L = \frac{3}{2}$ and there are six states in the valence band: $\left|\frac{3}{2}, \pm\frac{3}{2}\right\rangle$, $\left|\frac{3}{2}, \pm\frac{1}{2}\right\rangle$, and $\left|\frac{1}{2}, \pm\frac{1}{2}\right\rangle$.

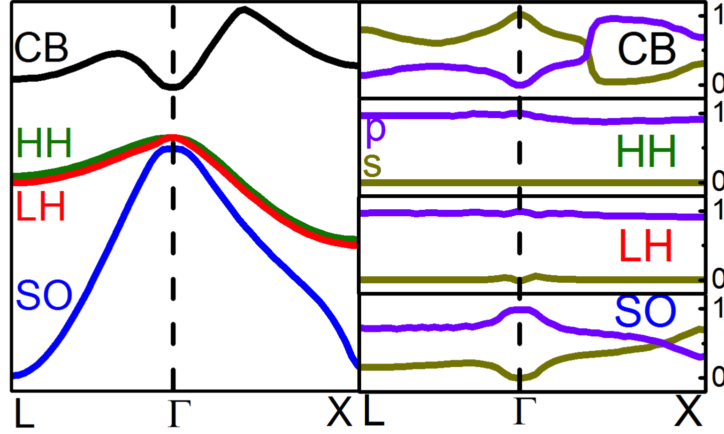

Figure 2.2: Tight binding calculations of the bandstructure of GaAs. Left: Bandstructure showing the conduction (black), heavy hole (red), light hole (green), and split-off (blue) bands. There is an energy gap between the heavy hole and conduction bands for which there are no states available to the electrons. Right: The percent p-type and s-type for each band. At the Γ point, the conduction band is purely s-type, and the valence bands are purely p-type. Code was developed by John Hinckley.

If we ignore spin-orbit effects, these three bands are degenerate at $\mathbf{k} = 0$. Including spin-orbit effects causes the $\left|\frac{1}{2}, \pm\frac{1}{2}\right\rangle$ band to have a slightly lower energy than the other two bands, and so this is referred to as the split-off band. Furthermore, the $\left|\frac{3}{2}, \pm\frac{3}{2}\right\rangle$ and $\left|\frac{3}{2}, \pm\frac{1}{2}\right\rangle$ bands are only degenerate at exactly $\mathbf{k} = \mathbf{0}$. For small $\mathbf{k}$, the dispersion relation can be approximated by the effective mass equation [19]:

$$E(\mathbf{k}) = E_0 + \frac{\hbar^2}{2m^*}k^2 \tag{2.7}$$

Since the $\left|\frac{3}{2}, \pm\frac{3}{2}\right\rangle$ and $\left|\frac{3}{2}, \pm\frac{1}{2}\right\rangle$ states have different curvatures about $\mathbf{k} = 0$, this results in a difference in effective mass, and so these two bands are referred to as the heavy and light hole bands respectively.

2.4 Optical Selection Rules

Now that we know the quantum states in the conduction and valence bands, we can discuss transitions between these states.

When the measurement time is much longer than the transition time, the rate of transition from one quantum state to another can be approximated using Fermi's golden rule:

$$W_{i\to f} = \frac{2\pi}{\hbar} \left|\langle f| H' |i\rangle\right|^2 \delta\left(E_f - E_i - \hbar\omega\right) \tag{2.8}$$

It can be derived from first-order time-dependent perturbation theory [20].

We will consider transitions for which a laser is tuned to the bandgap of the semiconductor, such that the transition matrix is given by

$$\langle\psi_c| \mathbf{D} |\psi_v\rangle \tag{2.9}$$

where $|\psi_{c,v}\rangle$ are the wavefunctions of the conduction and valence bands respectively, and $\mathbf{D}$ is the dipole moment operator. For left and right circularly polarized light, the dipole moment operators are given by:

$$\sigma^- = \frac{1}{\sqrt{2}}(p_x - ip_y) \tag{2.10}$$

$$\sigma^+ = \frac{1}{\sqrt{2}}(p_x + ip_y) \tag{2.11}$$

In the previous section, we found that the conduction band is s-like ($|\psi_{c\uparrow,\downarrow}\rangle = |s\rangle |\uparrow,\downarrow\rangle$), and therefore spherically symmetric.

The valence band states are given by $\left|\frac{3}{2}, \frac{\pm 3}{2}\right\rangle$ for the heavy hole band and $\left|\frac{3}{2}, \frac{\pm 1}{2}\right\rangle$ for the light hole band. These can be decomposed into the constituent angular momentum states using the Clebsch-Gordon coefficients [17].

The heavy hole states can be written as:

$$\begin{aligned}\left|\text{HH}^{+}\right\rangle &= \left|\frac{3}{2},\frac{3}{2}\right\rangle = -\frac{1}{\sqrt{2}}\left(|p_x\rangle + i\,|p_y\rangle\right)|\uparrow\rangle \\ \left|\text{HH}^{-}\right\rangle &= \left|\frac{3}{2},-\frac{3}{2}\right\rangle = \frac{1}{\sqrt{2}}\left(|p_x\rangle - i\,|p_y\rangle\right)|\downarrow\rangle\end{aligned} \tag{2.12}$$

and the light hole states can be written as:

$$\begin{aligned}\left|\text{LH}^{+}\right\rangle &= \left|\frac{3}{2},\frac{1}{2}\right\rangle = -\frac{1}{\sqrt{6}}\left(|p_x\rangle + i\,|p_y\rangle - 2\,|p_z\rangle\right)|\uparrow\rangle \\ \left|\text{LH}^{-}\right\rangle &= \left|\frac{3}{2},-\frac{1}{2}\right\rangle = \frac{1}{\sqrt{6}}\left(|p_x\rangle - i\,|p_y\rangle + 2\,|p_z\rangle\right)|\downarrow\rangle\end{aligned} \tag{2.13}$$

In calculating the transition matrices, symmetry considerations allow us to reduce the number of terms. Let us consider the following matrix element:

$$\langle s|\, p_x\, |p_y\rangle = \iiint_{-\infty}^{\infty} \psi_s p_x p_y \, dx\, dy\, dz \tag{2.14}$$

Under the transformation $x \to -x$, the integral over x becomes (recalling that ψ_s is spherically symmetric):

$$\begin{aligned}\int_{-\infty}^{\infty} \psi_s p_x p_y \, dx &= \int_{\infty}^{-\infty} \psi_s(-p_x)p_y(-\, dx) \\ &= -\int_{\infty}^{-\infty} \psi_s p_x p_y \, dx\end{aligned} \tag{2.15}$$

Clearly the integral, and therefore the matrix element, must be zero. In this way, the only nonzero elements are $\langle s|\, p_x\, |p_x\rangle$, $\langle s|\, p_y\, |p_y\rangle$, and $\langle s|\, p_z\, |p_z\rangle$. Considering the symmetry of the system again, it turns out these three matrix elements are equal, and so we can define:

$$p_{cv} = \langle s|\, p_x\, |p_x\rangle = \langle s|\, p_y\, |p_y\rangle = \langle s|\, p_z\, |p_z\rangle \tag{2.16}$$

With these simplifications in mind, the only nonzero transition matrices for transitions

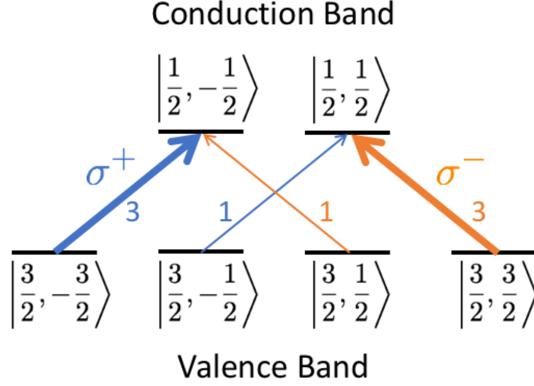

Figure 2.3: Optical selection rules for transitions between the valence band and conduction band in III-V semiconductors, for right (blue) and left (orange) circularly polarized light. The rate of transition from the heavy hole band to the conduction band is three times higher than the rate from the light hole band for a given circular polarization.

between each valence band state and the conduction band for right circularly polarized light (σ^+) are (using $\langle\uparrow|\uparrow\rangle = 1, \langle\uparrow|\downarrow\rangle = 0$):

$$\begin{aligned}
\langle\psi_{c\downarrow}|\,\sigma^+\,|\mathrm{HH}^-\rangle &= \langle\downarrow|\,\langle s|\left(\frac{1}{\sqrt{2}}(p_x + ip_y)\right)\left(\frac{1}{\sqrt{2}}\left(|p_x\rangle - i\,|p_y\rangle\right)|\downarrow\rangle\right) \\
&= p_{cv} \\
\langle\psi_{c\downarrow}|\,\sigma^+\,|\mathrm{LH}^-\rangle &= \frac{1}{\sqrt{3}}p_{cv}
\end{aligned} \tag{2.17}$$

and similarly for left circularly polarized light. Since the transition rate is proportional to the square of the transition matrix (Eq. 2.8), the rate for transitions from the heavy hole band is three times the rate from the light hole band. All the allowed transitions and their relative rates are shown in Fig. 2.3.

Due to this difference in transition rates, for excitation with right circularly polarized light, one will get three times as many spin-down electrons in the conduction band as spin-up electrons. The spin polarization is therefore:

$$P = \frac{n_\uparrow - n_\downarrow}{n_\uparrow + n_\downarrow} = \frac{1-3}{1+3} = -50\% \tag{2.18}$$

Similarly, excitation with left circularly polarized light results in a +50% spin polarization. Optical orientation of electron spin in GaAs in this way was first demonstrated by Zakharchenya *et al.* [21].

Optical pumping also results in a hole spin polarization in the valence band; however, this depolarizes very rapidly (after ~1 ps) [22]. When the spin-polarized electrons in the conduction band recombine with the depolarized holes, the optical selection rules apply again, and so the maximum polarization of the luminescence is 25%. The spin polarization can be measured through the measurement of the polarization of the photoluminescence [23]. However, spin lifetimes that exceed the recombination time cannot be measured in this way. For GaAs, the recombination time at 10 K is ~100 ps [24].

To avoid being limited by the recombination time, one can study n-doped materials, meaning that there is an equilibrium electron population in the conduction band. Since this equilibrium population is unpolarized, optical pumping results in a spin polarization of <50% in the conduction band. However, since the polarized and unpolarized electrons in the conduction band have an equal chance of recombining with a hole, this means that a spin-polarized population will remain in the conduction band after recombination. This can then be measuring using Faraday rotation, which will be discussed in the next section. In this way, one can measure the spin dynamics without being limited by the recombination time.

2.5 Faraday Rotation

The Faraday effect, discovered by Michael Faraday in 1845, is the rotation of the linear polarization of light as it passes through a material across which a magnetic field has been applied. A similar effect can be seen in spin-polarized GaAs: the difference in the populations of spin up and spin down electrons leads to a circular birefringence that can be measured

and used to calculate the spin polarization in the sample.

Again, we start with Fermi's golden rule (Eq. 2.8). We are interested in light-induced transitions, and so the Hamiltonian we will consider is

$$H = \frac{1}{2m}\left(\mathbf{p} + \frac{e}{c}\mathbf{A}\right)^2 - e\phi \tag{2.19}$$

We will take the gauge $\phi = 0$ and $\nabla \cdot \mathbf{A} = 0$. In this gauge, $\mathbf{E} = \frac{-1}{c}\frac{\partial \mathbf{A}}{\partial t}$, and so if we assume the form $\mathbf{A} = \mathbf{A}_0 e^{i(\mathbf{a}\cdot\mathbf{r} - \omega t)}$ we have $|\mathbf{A}_0|^2 = \frac{c^2}{\omega^2}|\mathbf{E}_0|^2$.

If we say $H = \frac{|\mathbf{p}|^2}{2m} + H'$, then the perturbing Hamiltonian we will use in Fermi's golden rule becomes:

$$H' = \frac{e}{2mc}\left(\mathbf{p}\cdot\mathbf{A} + \mathbf{A}\cdot\mathbf{p}\right) + \frac{e^2}{2mc^2}\left|\mathbf{A}\right|^2 \tag{2.20}$$

This last term can be ignored if $\frac{e}{c}|\mathbf{A}| \ll |\mathbf{p}|$, which is true except in the case of very strong fields. As $\mathbf{p} = -i\hbar\nabla$ is an operator, the commutative property does not apply and the two terms in the parenthesis cannot be combined.

The states $|i\rangle$ and $|f\rangle$ in Eq. 2.8 are, in this case, the valence and conduction band states, respectively, which can both be written as Bloch wavefunctions [25]:

$$\psi_i = \Omega^{-1/2} e^{i\mathbf{k}_i\cdot\mathbf{r}} U_i(\mathbf{k}_i) \tag{2.21}$$

$$\psi_f = \Omega^{-1/2} e^{i\mathbf{k}_f\cdot\mathbf{r}} U_f(\mathbf{k}_f) \tag{2.22}$$

where Ω is the volume element over which integration is performed and $U(\mathbf{k})$ has the same periodicity as the lattice structure . Using these wavefunctions, we get (following [26])

$$\langle f|\, H' \,|i\rangle = \int_\Omega \psi_f^* H' \psi_i d^3\mathbf{r} \tag{2.23}$$

$$= \frac{-ie}{4mc}|\mathbf{A}_0 \cdot \mathbf{p}_{if}| \tag{2.24}$$

where we have defined the matrix element $\mathbf{p}_{if} = \langle \mathbf{k}_f | \, \mathbf{p} \, | \mathbf{k}_i \rangle = \frac{-i\hbar}{\Omega} \int_\Omega U_f^*(\mathbf{k}_f) \nabla U_i(\mathbf{k}_i) d^3\mathbf{r}$. $E_p = \frac{|\mathbf{p_{if}}|^2}{2m_0}$ is a parameter that can be experimentally fit. For example, $E_p = 25.7$ eV for GaAs [27].

Plugging this into Eq. 2.8 and integrating over all values of k, we get

$$W_{\text{tot}} = \frac{2}{(2\pi)^3} \iiint\limits_{\text{BZ}} \frac{2\pi}{\hbar} \frac{e^2}{4m^2\omega^2} |\mathbf{E}_0|^2 |\mathbf{p}_{if}|^2 \delta(E_f - E_i - \hbar\omega) \, \mathrm{d}^3 V_k \tag{2.25}$$

$$= \frac{2\pi}{\hbar} \frac{e^2}{4m^2\omega^2} |\mathbf{E}_0|^2 |\mathbf{p}_{if}|^2 N_{cv}(E_f - E_i) \tag{2.26}$$

where $N_{cv}(E_f - E_i) = \frac{2}{(2\pi)^3} \iint\limits_S \frac{\mathrm{d}S_k}{\left|\nabla_\mathbf{k}(E_f - E_i)\right|}$ is the joint density of states and the integration is performed over the first Brillouin zone. The extra factor of 2 is to account for both spin up and spin down states.

2.5.1 Complex Permittivity Near the Band Edge

At this point, we have calculated the rate at which transitions occur when light impinges on a semiconductor. As each transition is associated with the absorption of a photon of energy $\hbar\omega$, we can calculate the absorption coefficient α, which is related to the complex permittivy $\epsilon_2 = \frac{n(\omega)c}{\omega}\alpha$. In this way, we get

$$\epsilon_2 = \frac{\pi e^2}{\epsilon_0 m^2 \omega^2} |\mathbf{p}_{if}|^2 N_{cv}(E_f - E_i) \tag{2.27}$$

Now let us look at the specific case of zinc-blende semiconductors, in which the conduction and valence bands have parabolic dispersion relations near the band-edge (Fig. 2.4a), and so the joint density of states is

$$N_{cv}(E_c - E_v) = \frac{1}{2\pi^2} \left(\frac{2\mu}{\hbar}\right)^{3/2} (\hbar\omega - E_g)^{1/2} \tag{2.28}$$

where μ is the reduced mass. Plugging this into equation 2.27 and using the Kramers-Kronig relations [26], we can calculate the real part of the permittivity:

$$\epsilon_1(\omega) = 1 + \frac{1}{\pi} P \int \frac{\epsilon_2(\omega')}{\omega' - \omega} \mathrm{d}\omega \tag{2.29}$$

$$= 1 + \frac{e^2 \left|\mathbf{p}_{if}\right|^2}{4\pi\epsilon_0 m^2 \omega^2 \sqrt{E_g}} \left(\frac{2\mu}{\hbar^2}\right)^{3/2} \left(2E_g - \hbar\omega - 2\sqrt{E_g(E_g - \hbar\omega)}\Theta(E_g - \hbar\omega)\right) \tag{2.30}$$

The index of refraction can then be calculated with $n = \sqrt{\epsilon_1}$ (Fig. 2.4b).

2.5.2 Circular Birefringence

If there is an unequal population of spin up and spin down electrons in the conduction band (i.e. a spin polarization), then the absorption edges for left circularly polarized light is shifted with respect to the absorption for right circularly polarized light (see section 2.4). This results in a difference in the index of refraction for left and right circularly polarized light, which is referred to as circular birefringence.

If linearly polarized light is transmitted through a sample with circular birefringence, the transmitted light will also be linearly polarized but with the axis of polarization rotated by some angle. We can see this by employing Jones calculus [28]. In Jones calculus, horizontally polarized light can be written as the sum of right and left circularly polarized components:

$$\mathbf{E}_i = E_0 \begin{pmatrix} 0 \\ 1 \end{pmatrix} = \frac{E_0}{\sqrt{2}} \left[\begin{pmatrix} 1 \\ -i \end{pmatrix} + \begin{pmatrix} 1 \\ i \end{pmatrix} \right] \tag{2.31}$$

Since the index of refraction is different for right and left circularly polarized light, each of these two components will pick up a different phase factor e^{-inkd}, where d is the thickness

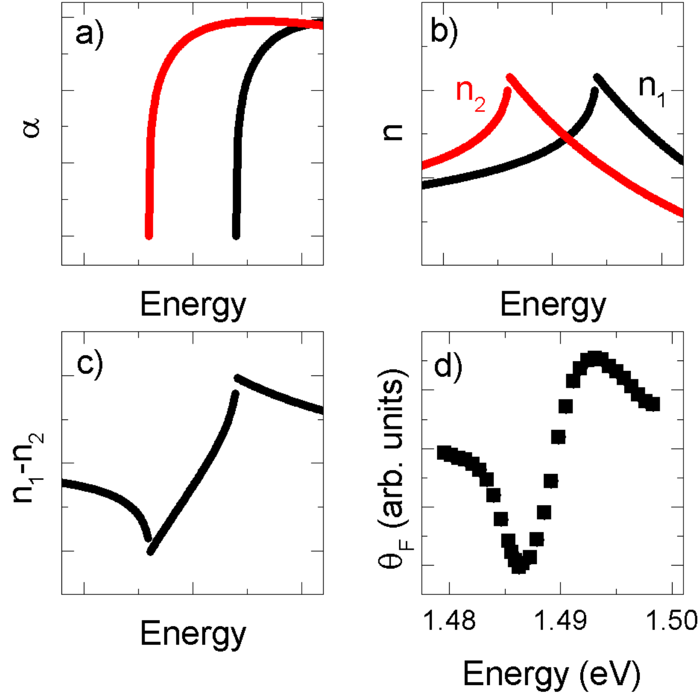

Figure 2.4: Faraday rotation in GaAs. (a) The absorption for a three dimensional semiconductor. (b) Unequal populations of spin-up and spin-down electrons results in different indices of refraction for left- and right-circularly polarized light. (c) The Faraday angle is proportional to the difference in indices of refraction. (d) Measured Faraday rotation as a function of wavelength for an $In_{0.026}Ga_{0.964}$ As sample at 10 K. The calculated bandgap for this material at 0 K is 1.49 eV.

of the sample through which the light is transmitted.

$$\mathbf{E}_f = \frac{E_0}{\sqrt{2}} \left[\begin{pmatrix} 1 \\ -i \end{pmatrix} e^{-in_R kd} + \begin{pmatrix} 1 \\ i \end{pmatrix} e^{-in_L kd} \right] \tag{2.32}$$

$$= E_0 \begin{pmatrix} \cos\left((n_R - n_L)kd\right) \\ -\sin\left((n_R - n_L)kd\right) \end{pmatrix} e^{-i(n_R+n_L)kd} \tag{2.33}$$

We can ignore the overall phase factor, as we are interested in the intensity, which is the square of the electric field. In this way, we arrive at

$$\mathbf{E}_f = R\left((n_R - n_L)kd\right)\mathbf{E}_i \tag{2.34}$$

where $R(\theta)$ is the rotation matrix. We can see that circular birefringence thus has the effect of rotating the polarization of the transmitted light by $\theta = (n_R - n_L)kd$ (Fig. 2.4c).

In a real material, the absorption does not cut off abruptly at $\hbar\omega = E_g$. Instead, below the bandgap there is an exponentially decaying tail called the Urbach tail [29], which arises due to disorder in the material. Including this contribution will have the effect of smoothing out the peaks in the index of refraction.

For small polarizations, the Faraday angle is proportional to the spin polarization along the direction of the laser propagation [30]. In this way, the spin polarization of a semiconductor can be optically measured.

The term Faraday rotation is generally used when the samples are measured in a transmission geometry. When measurements are done in the reflection geometry, the effect is generally referred to as Kerr rotation although the physical origin of the rotation is the same. Faraday rotation tends to have a better signal-to-noise ratio, as less pump scatter travels along the collection path in the transmission geometry. However, for some samples studied in this thesis, transmission measurements were not possible and so the reflection geometry was used instead.

2.6 Conclusion

In this chapter, we have discussed the band structure and optical properties of GaAs. We have discussed how optical pumping by circularly polarized light can result in up to a 50% spin polarization in GaAs, and how the spin polarization can be measured by the Faraday rotation of a linearly polarized probe beam. These methods will be combined in Ch. 4 to create a pump-probe optical setup to measure the spin dynamics in GaAs.

Chapter 3

Spins in Semiconductors

3.1 Introduction

Semiconductor spintronics, in which spins rather than charge are used to encode and manipulate data, is of interest as an alternative to traditional computing technologies [31]. In order to successfully create an all-electrical spintronic device, we must have a full understanding of the electrical generation and manipulation of spins, as well as the dephasing mechanisms that lead to a decay of the total spin polarization.

In this chapter, we will discuss spin dynamics in semiconductors, focusing mainly on n-type (001) GaAs. We will begin by describing spin-orbit coupling in zinc-blende semiconductors and how it may be thought of as an effective magnetic field. This will lead into a discussion of the dephasing mechanisms present in n-type GaAs. Finally, we will discuss different spin polarization mechanisms, focusing on the electrical generation of a spin polarization.

3.2 Spin Dynamics in Semiconductors

We will begin our discussion of the spin dynamics in semiconductors by considering a magnetic moment in a magnetic field. The torque on the magnetic moment is given by:

$$\mathbf{T} = \mathbf{B} \times \boldsymbol{\mu} \tag{3.1}$$

where $\boldsymbol{\mu} = g\frac{\mu_B}{\hbar}\mathbf{S}$ is the magnetic moment of the spin. The g factor for an electron is roughly 2.002319 in free space, but it can have a different, effective value in a material. For example, the effective g factor in GaAs at 0 K is approximately -0.45 [32].

The spin operator is $\mathbf{S} = \frac{1}{2}\sigma_i\hat{\mathbf{x}}_i$, where σ_i are the Pauli spin matrices, given by

$$\sigma_x = \begin{pmatrix} 0 & 1 \\ 1 & 0 \end{pmatrix}, \sigma_y = \begin{pmatrix} 0 & -i \\ i & 0 \end{pmatrix}, \sigma_z = \begin{pmatrix} 1 & 0 \\ 0 & -1 \end{pmatrix} \tag{3.2}$$

The torque is the rate of change of the angular momentum, which in this system is just the spin, so $\mathbf{T} = \frac{d\mathbf{S}}{dt}$. Combining all this, we arrive at the basic spin dynamics equation:

$$\frac{d\mathbf{S}}{dt} = \mathbf{\Omega_L} \times \mathbf{S} \tag{3.3}$$

where $\mathbf{\Omega_L} = \frac{g\mu_B}{\hbar}\mathbf{B}$ is the Larmor frequency. Therefore, in the presence of a magnetic field, an electron spin will precess about that magnetic field with frequency $\mathbf{\Omega_L}$.

Equation 3.3 implies that the magnitude of the spin polarization does not change over time. However, this equation only applies if there is one value for the Larmor frequency. In reality, fluctuations in the magnetic field will lead to spin relaxation and dephasing. In section 3.4, we will discuss spin relaxation and dephasing due to time-dependent and momentum-dependent magnetic fields. However, first we must discuss spin-orbit coupling in semiconductors.

3.3 Spin-Orbit Fields

Spin-orbit (SO) coupling is a relativistic effect in which a charged particle moving through an electric field "sees" an effective magnetic field. If the charged particle has spin, such as an electron, then the effective magnetic field will produce a torque on that spin.

Spin-orbit effects can also be thought of in terms of Kramer's degeneracy. In a system with space-inversion and time-reversal symmetry, we have

$$\begin{aligned} \epsilon_{\mathbf{k}\uparrow} &= \epsilon_{-\mathbf{k}\uparrow} \\ \epsilon_{-\mathbf{k}\uparrow} &= \epsilon_{\mathbf{k}\downarrow} \end{aligned} \tag{3.4}$$

so $\epsilon_{\mathbf{k}\uparrow} = \epsilon_{\mathbf{k}\downarrow}$ and the system is spin degenerate. However, if we were to break time-reversal symmetry (for example by applying an external magnetic field) or space-inversion symmetry, the spin states would no longer be spin degenerate. This spin splitting can be written in terms of an effective magnetic field called the spin-orbit field.

Spin-orbit fields are of interest as they allow for the coherent control of spin polarizations without the use of an external magnetic field [33, 34]. In the following sections, we will consider various effects that result in space-inversion asymmetry and therefore contribute to the total spin-orbit field.

3.3.1 Bulk and Structural Inversion Asymmetry

As discussed in section 2.2, due to the arrangement of Ga and As atoms in the crystal structure, GaAs has bulk inversion asymmetry (BIA). The spin-orbit field that arises from this bulk-inversion asymmetry is referred to as the Dresselhaus field [35], and the corresponding Hamiltonian can be written as:

$$H_D = \gamma_D \left[k_x(k_y^2 - k_z^2)\sigma_x + k_y(k_z^2 - k_x^2)\sigma_y + k_z(k_x^2 - k_y^2)\sigma_z\right] \tag{3.5}$$

where γ_D is the material-dependent Dresselhaus parameter, and x, y, and z are the [100], [010], and [001] crystal axes respectively.

In epilayers and quantum wells, if there is no net motion of the electrons along the [001] crystal axis, then $\langle k_z \rangle = 0$, and so Eq. 3.5 can be reduced to

$$\begin{aligned} H_D &= \gamma_D \left[k_x(k_y^2 - \langle k_z^2 \rangle)\sigma_x + k_y(\langle k_z^2 \rangle - k_x^2)\sigma_y \right] \\ &= -\gamma_D \left[(k_x\sigma_x - k_y\sigma_y) \langle k_z^2 \rangle + \left(k_y k_x^2 \sigma_y - k_x k_y^2 \sigma_x \right) \right] \end{aligned} \tag{3.6}$$

$\langle k_z^2 \rangle$ is nonzero for quantum wells, and increases as the well width decreases (i.e. the quantum confinement increases). However, in epilayers, $\langle k_z^2 \rangle$ is negligible, and so the linear component of eq. 3.6 can be ignored. This means the Dresselhaus spin-orbit field is expected to be cubic in momentum in zinc-blende epilayers. However, the spin-orbit field in InGaAs epilayers was found to be linear in momentum [36], meaning that the Dresselhaus spin-orbit field is negligible compared with other contributions to the spin-orbit field.

In addition to bulk inversion asymmetry, there is another space-inversion asymmetry called structural inversion asymmetry (SIA). This occurs in heterostructures, in which the change in the material along the growth axis results in space-inversion asymmetry. For a growth axis along the [001] crystal axis, the resulting spin-orbit field, called the Bychkov-Rashba or simply the Rashba field [37], is described by:

$$H_R = \alpha_R(\sigma_x k_y - \sigma_y k_x) \tag{3.7}$$

This effect is greatest for electrons that are close to the boundary of the heterojunction, and so dominates in quantum wells. In epilayers and bulk materials, where most of the electrons are not close to this boundary, the effect is smaller.

3.3.2 Biaxial and Uniaxial Strain

If an epilayer is grown on a substrate with a different lattice parameter (e.g. InGaAs grown on a GaAs substrate), the epilayer will be strained as it tries to match its in-plane lattice parameter to that of the substrate. This results in biaxial strain in the epilayer. However, there will also be strain relaxation in the epilayer, which can be described as uniaxial strain applied in the plane perpendicular to the growth axis. These two types of strain result in space-inversion asymmetry, and therefore contribute to the total spin-orbit field.

Uniaxial strain results in the Hamiltonian [38]:

$$H_1 = \frac{1}{2} C_3 \left[\sigma_x (\epsilon_{xy} k_y - \epsilon_{xz} k_z) + \sigma_y (\epsilon_{yz} k_z - \epsilon_{yx} k_x) + \sigma_z (\epsilon_{zx} k_x - \epsilon_{zy} k_y) \right] \tag{3.8}$$

where C_3 is a material constant, and ϵ_{ij} are the components of the strain tensor. For an epilayer grown along the (001) axis, this is simplified to:

$$H_1 = \frac{1}{2} C_3 \epsilon_{xy} \left(\sigma_x k_y - \sigma_y k_x \right) \tag{3.9}$$

which has the same form as the Rashba Hamiltonian (Eq. 3.7). Because of this, spin-orbit effects due to structural inversion asymmetry (SIA) (i.e. the Rashba Hamiltonian) and uniaxial strain can be combined into one Hamiltonian:

$$H_{\mathrm{SIA}} = \frac{1}{2} \alpha' (\sigma_x k_y - \sigma_y k_x) \tag{3.10}$$

Biaxial strain results in the Hamiltonian [39]:

$$H_2 = D[\sigma_x k_x (\epsilon_{zz} - \epsilon_{yy}) + \sigma_y k_y (\epsilon_{xx} - \epsilon_{zz}) + \sigma_z k_z (\epsilon_{yy} - \epsilon_{xx})] \tag{3.11}$$

where C_3 is a material constant. For an epilayer grown along the (001) axis, this is simplified

to:

$$H_2 = D(\epsilon_{zz} - \epsilon_{xx})(\sigma_x k_x - \sigma_y k_y) \tag{3.12}$$

which has the same form as the linear-Dresselhaus Hamiltonian (Eq. 3.6). Because of this, spin-orbit effects due to bulk inversion asymmetry (BIA) (i.e. the Dresselhaus Hamiltonian) and biaxial strain can be combined into one Hamiltonian:

$$H_{\text{BIA}} = \frac{1}{2}\beta'(\sigma_x k_x - \sigma_y k_y) \tag{3.13}$$

Combining Eqs. 3.10 and 3.13, we arrive at the expression for the total spin-orbit field:

$$H_{\text{SO}} = \frac{1}{2}(\alpha' k_y + \beta' k_x)\sigma_x - \frac{1}{2}(\alpha' k_x + \beta' k_y)\sigma_y \tag{3.14}$$

We can characterize the strength and crystal axis dependence of the spin-orbit field with the parameters α' and β'. The directional dependence of the spin-orbit field can also be characterized by the parameter $r = \alpha'/\beta'$. This dependence for different values of r is shown in Fig. 3.1. One can see that that, for momenta along the [110] and [1$\bar{1}$0] crystal axes, the spin-orbit field is purely perpendicular to the direction of the motion of the electrons.

A special case is $r = \pm 1$ (i.e. $\alpha' = \pm\beta'$), also referred to as a spin helix state [40]. Since the spin-orbit field is zero along the [1$\pm$10] crystal axis, spin dephasing is suppressed for electron momenta in that direction [41].

3.3.3 Determining the Spin-Orbit Parameters

The spin-orbit parameters α and β can be determined from measurements of the spin-orbit field along different crystal axes. For the Hamiltonian given in Eq. 3.14, the effective spin-

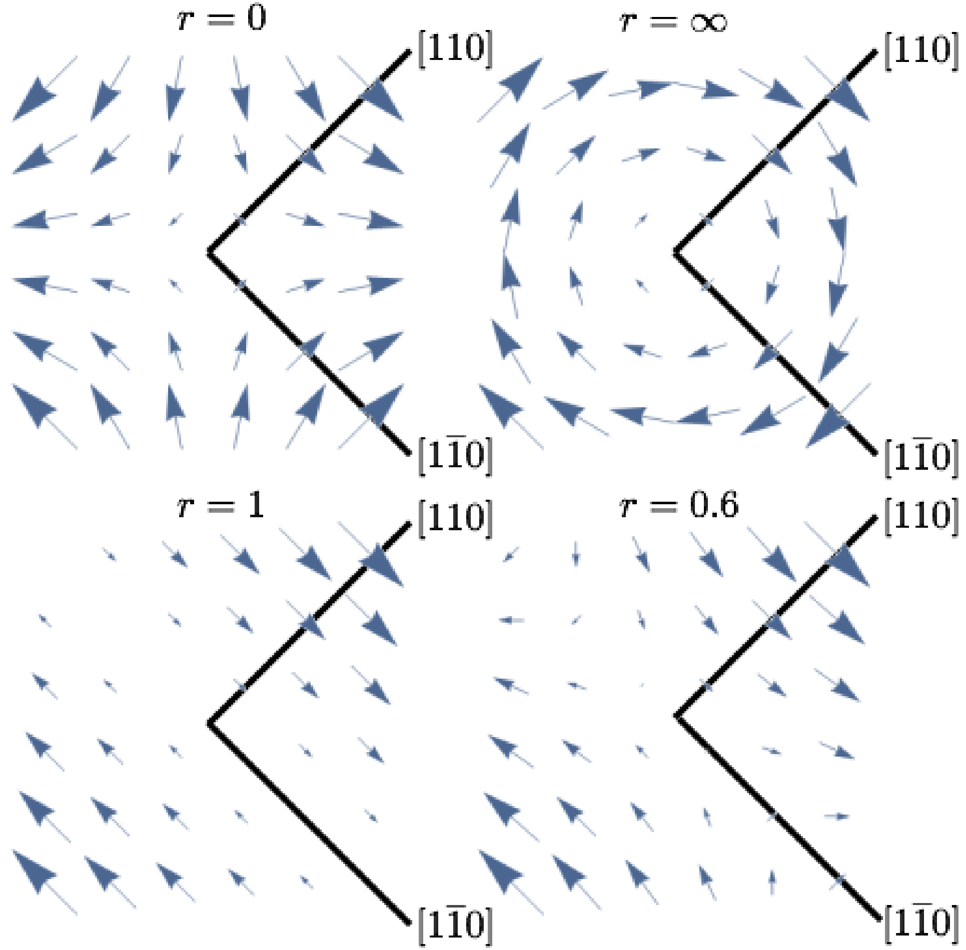

Figure 3.1: Vector plot of the spin-orbit field for different momentum directions and for different values of $r = \alpha'/\beta'$. $r = 0$ corresponds to a linear-Dresselhaus-like field (i.e. $\alpha' = 0$). $r = \infty$ corresponds to a Rashba-like field (i.e. $\beta' = 0$). $r = 1$ (i.e. $\alpha' = \beta'$) is a spin helix state. The r of a material usually does not correspond to one of these extreme cases, and may have an intermediate value, such as $r = 0.6$.

orbit magnetic field is

$$\mathbf{B}_{\mathrm{SO}} = \frac{\hbar}{g\mu_B}\left[(\alpha' k_y + \beta' k_x)\hat{\mathbf{x}} - (\alpha' k_x + \beta' k_y)\hat{\mathbf{y}}\right] \tag{3.15}$$

For $\mathbf{k} \parallel [110]$ and $\mathbf{k} \parallel [1\bar{1}0]$, the spin-orbit fields are:

$$\begin{aligned} \mathbf{B}_{[110]} &= \frac{\hbar}{g\mu_B} k \left[(\alpha' + \beta')\frac{\hat{\mathbf{x}} - \hat{\mathbf{y}}}{\sqrt{2}}\right] \\ \mathbf{B}_{[1-10]} &= \frac{\hbar}{g\mu_B} k \left[(-\alpha' + \beta')\frac{\hat{\mathbf{x}} + \hat{\mathbf{y}}}{\sqrt{2}}\right] \end{aligned} \tag{3.16}$$

that is, the spin-orbit field is oriented along the crystal axis perpendicular to the direction of the momentum, with magnitudes

$$\begin{aligned} B_{[110]} &= \frac{\hbar}{g\mu_B} k(\alpha' + \beta') \\ B_{[1-10]} &= \frac{\hbar}{g\mu_B} k(-\alpha' + \beta') \end{aligned} \tag{3.17}$$

where k can be determined from the measured drift velocity using $\hbar k = m^* v_d$. While β' is always positive, α' can be positive or negative, and so it is important to measure the sign of the spin-orbit field as well as its magnitude. With these equations, it is possible to determine the spin-orbit field parameters α' and β' once the magnitude of the spin-orbit field is known. This is the method discussed in Section 4.6.

Alternatively, if instead we consider $\mathbf{k} \parallel [100]$, the spin-orbit field is:

$$\mathbf{B}_{[100]} = \frac{\hbar}{g\mu_B} k \left[\beta' \hat{\mathbf{x}} - \alpha' \hat{\mathbf{y}}\right] \tag{3.18}$$

and so the component of the spin-orbit field parallel to the momentum of the electron is proportional to β', and the component perpendicular to the momentum is proportional to α'. This is the method used to determine the spin-orbit field coefficients by Norman *et al.*

in [36].

A quick note about units: α' and β' are defined such that $\alpha'/\hbar$ and $\beta'/\hbar$ are in units of velocity. In Chapter 6, α and β are used instead, and they are given in the units μm neV/μs. The conversion is simply $\alpha' = \frac{\hbar}{m^*}\alpha$ and similarly for β.

Now that we have some understanding of spin-orbit coupling and spin-orbit fields, we will discuss spin dephasing and inhomogenous broadening.

3.4 Spin Relaxation and Dephasing

In 1946, Felix Bloch proposed a modification to the spin dynamics equations to account for spin relaxation and dephasing [42]. Ignoring precession, the rate of change of the spin polarization is:

$$\begin{aligned} \frac{dS_z}{dt} &= -\frac{S_x}{T_2} \\ \frac{dS_y}{dt} &= -\frac{S_y}{T_2} \\ \frac{dS_z}{dt} &= -\frac{S_z - S_0}{T_1} \end{aligned} \tag{3.19}$$

where T_1 and T_2 are the relaxation and dephasing times respectively. Combining Eqs. 3.3 and 3.19 into a more compact form, we arrive at

$$\frac{d\mathbf{S}}{dt} = \mathbf{\Omega}_L \times \mathbf{S} - \Gamma \cdot \mathbf{S} + \frac{S_0}{T_1}\hat{\mathbf{z}} \tag{3.20}$$

where

$$\Gamma = \begin{pmatrix} \frac{1}{T_2} & 0 & 0 \\ 0 & \frac{1}{T_2} & 0 \\ 0 & 0 & \frac{1}{T_1} \end{pmatrix} \tag{3.21}$$

is the relaxation tensor.

Although Bloch's addition was based on phenomenological considerations, calculations

based on microscopic considerations yield the same results. Consider a single spin in a fluctuating time-dependent magnetic field with the Hamiltonian:

$$H = \frac{1}{2}[\Omega_0\hat{\mathbf{z}} + \mathbf{\Omega}(t)] \cdot \sigma \tag{3.22}$$

Using the Born-Markov approximation [43], we arrive at Eq. 3.19, with the spin relaxation and dephasing times given by:

$$\begin{aligned} \frac{1}{T_1} &= \frac{(\overline{\omega_x^2} + \overline{\omega_y^2})\tau_c}{1 + \omega_0^2\tau_c^2} \\ \frac{1}{T_2} &= \overline{\omega_z^2}\tau_c + \frac{(\overline{\omega_x^2} + \overline{\omega_y^2})\tau_c}{2(1 + \omega_0^2\tau_c^2)} \end{aligned} \tag{3.23}$$

where τ_c is the correlation time of the fluctuating magnetic field.

This means that even a single spin will experience irreversible relaxation and dephasing due to intrinsic fluctuation in the local magnetic field experienced by the spin. If instead we have an ensemble of spins, we must consider additional contributions to the spin dephasing that result from inhomogeneous broadening. These contributions in semiconductors include momentum-dependent spin-orbit coupling, which will be discussed in more detail in the following subsections, and a momentum- [44] or energy- [45] dependent g factor. Without scattering, these contributions to inhomogeneous broadening are reversible, and can be removed in a spin echo measurement [46]. Scattering has the effect of randomizing the spin precession, and so the inhomogeneous broadening becomes irreversible [45]. The total spin dephasing time including inhomogeneous broadening is denoted as T_2^*.

The two dominant dephasing mechanisms in the materials studied in this thesis are D'yakonov-Perel' and Elliot-Yafet dephasing, which will be discussed in more detail in the following sections.

3.4.1 D'yakonov-Perel' Dephasing

We saw in section 3.3 that the effective spin-orbit magnetic field depends on the direction of the electron's momentum. In an ensemble of electrons with different velocities, this means that each electron experiences a different spin-orbit field. Since each electron is precessing about a different magnetic field this results in dephasing of the total spin polarization. Scattering events have the effect of randomizing the electrons' motion and therefore the spin-orbit fields they experience, suppressing this dephasing mechanism.

This effect is called D'yakonov-Perel' dephasing [47]. The corresponding dephasing tensor is [48]

$$\Gamma_{\mathrm{DP}} = \tau_{\mathrm{DP}}^{-1} \begin{pmatrix} r^2+1 & 2r & 0 \\ 2r & r^2+1 & 0 \\ 0 & 0 & 2(r^2+1) \end{pmatrix} \tag{3.24}$$

in the {[100], [010], [001]} basis, where $\tau_{\mathrm{DP}}^{-1} = 2\tau\beta^2 v_F^2$, τ is the momentum scattering time, and v_F is the Fermi velocity.

The eigenaxes of this tensor are along the [1$\bar{1}$0], [110] and [001] crystal axis, and so this tensor can be diagonalized if we convert to the {[1$\bar{1}$0], [110], [001]} basis:

$$\Gamma_{\mathrm{DP}} = \tau_{\mathrm{DP}}^{-1} \begin{pmatrix} (r-1)^2 & 0 & 0 \\ 0 & (r+1)^2 & 0 \\ 0 & 0 & 2(r^2+1) \end{pmatrix} \tag{3.25}$$

In this form, we can clearly see that for the spin helix state ($r = \pm 1$), the spin dephasing is suppressed along the [1$\pm$10] crystal axis.

The dephasing rate Γ_{DP} is proportional to the momentum scattering time τ. Since D'yakonov-Perel' dephasing is due to precession of the spins *between* scattering events (Fig. 3.2a), the less time there is between scattering events, the lower the dephasing rate.

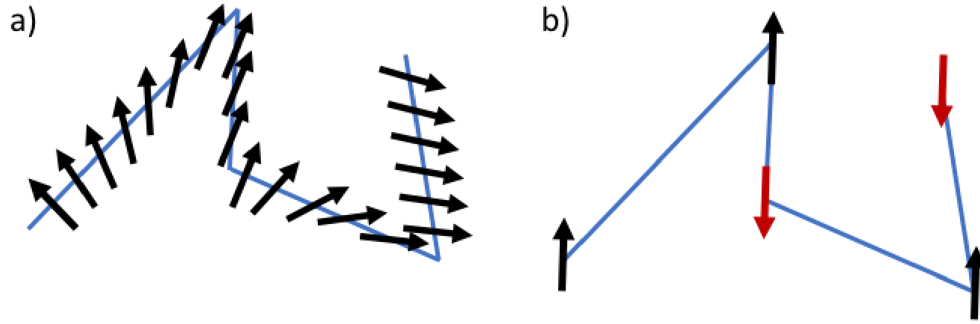

Figure 3.2: Schematic of (a) D'yakonov-Perel' and (b) Elliot-Yafet dephasing mechanisms. Adapted from [49].

The temperature dependence of the D'yakonov-Perel' dephasing rate goes as [47]:

$$\Gamma_{\mathrm{DP}} \propto \tau T^3 \tag{3.26}$$

where it is important to note that τ also has some temperature dependence (see Section 4.8 for more details on the temperature dependence of scattering mechanisms).

3.4.2 Elliot-Yafet Dephasing

Due to spin-orbit coupling, during a momentum scattering event, this is some probability of the electron's spin flipping. Over time, this results in a dephasing of the total spin polarization. This dephasing mechanism was first proposed by Elliott [50], and then expanded by Yafet [51] to include electron-phonon scattering, and so the mechanism is called Elliot-Yafet (EY) dephasing.

The tensor describing Elliot-Yafet dephasing is [52]:

$$\Gamma_{\mathrm{EY}} = \tau_{\mathrm{EY}}^{-1} \begin{pmatrix} 1 & 0 & 0 \\ 0 & 1 & 0 \\ 0 & 0 & 0 \end{pmatrix} \tag{3.27}$$

in the {[100], [010], [001]} basis, where $\tau_{\rm EY}^{-1} = \tau^{-1}\left(\pi\frac{v_F}{c}\right)^4$. One can see that the eigenaxes for the two dephasing tensors $\Gamma_{\rm DP}$ and $\Gamma_{\rm EY}$ are different.

The dephasing rate $\Gamma_{\rm EY}$ is inversely proportional to the momentum scattering time τ. Since dephasing occurs at scattering events (Fig. 3.2b), the less time there is between scattering events, the greater the dephasing rate.

The temperature dependence of the Elliot-Yafet dephasing rate goes as [48]:

$$\Gamma_{\rm EY} \propto \tau^{-1} T^2 \tag{3.28}$$

Again, it is important to note that τ also has some temperature dependence.

3.4.3 Temperature Dependence

Spins in an n-type III-V semiconductor will generally experience both D'yakonov-Perel' and Elliot-Yafet dephasing. In general, the way to separate the contributions from these two mechanisms to the total dephasing rate is to look at the temperature dependence.

Combining Eqs. 3.26 and 3.28, the total spin dephasing rate is:

$$\Gamma_{\rm s} = \Gamma_{\rm DP} + \Gamma_{\rm EY} = C_{\rm DP}\mu T^3 + C_{\rm EY}\mu^{-1}T^2 \tag{3.29}$$

where $\mu = \frac{q}{m^*}\tau$ is the electron mobility, and $C_{\rm DP}$ and $C_{\rm EY}$ are coefficients denoting the relative strength of the D'yakonov-Perel' and Elliot-Yafet dephasing mechanisms. Matters are complicated by the fact that there is an additional temperature dependence hidden in μ. This can be quantified by measuring the electron mobility at different temperatures.

If we have measured $\Gamma_{\rm s}$ and μ at different temperatures (see Chapter 4 for experimental methods), then we can use a two-independent-variable fit (with μ and T as the independent variables) to fit $\Gamma_{\rm s}$ to Eq. 3.29 and determine the coefficients $C_{\rm DP}$ and $C_{\rm EY}$.

The relative strength of the two dephasing mechanisms is then defined by:

$$q(T) = \frac{\Gamma_{\mathrm{EY}}}{\Gamma_{\mathrm{DP}}} = \frac{C_{\mathrm{EY}}}{C_{\mathrm{DP}}} \mu^{-2} T^{-1} \tag{3.30}$$

As we saw earlier, D'yakonov-Perel' and Elliot-Yafet dephasing have different eigenaxes, and so determining the relative strength of these two mechanisms is important to determine the steady-state behavior of the spin polarization.

3.5 Spin Polarization Mechanisms

In the previous section, we have discussed how the spin dynamics are affected by spin-orbit effects, including spin dephasing. However, in order for the spins to dephase, there must be a non-equilibrium spin polarization to begin with.

There are several ways to generate a spin polarization within a semiconductor. We have already discussed optical injection of a spin polarization in Section 2.4, in which circularly polarized light with energy matching the bandgap can be used to generate a spin polarization of up to 50%.

A very common method involves injecting a spin polarization into a semiconductor from a ferromagnetic material, in which the spins are already naturally polarized. This has been demonstrated for injection from ferromagnetic semiconductors [53] and ferromagnetic metals [54], and for injection into GaAs [54] and Si [55]. The spin polarization achievable through this method is typically 30% at 5 K without an external magnetic field for injection from a ferromagnetic metal into either GaAs [56, 57] or Si [55].

Although significant polarizations can be achieved using optical and ferromagnetic injection, an all-electrical, all-semiconductor method of spin polarization is of interest for spintronics applications [58]. Optical injection is clearly impractical for the development

of a spintronic device, and there are difficulties in integrating ferromagnetic materials in complementary metal-oxide-semiconductor (CMOS) devices, due to the inherent mismatch in material properties at the ferromagnet-semiconductor interface [59].

One possibility for all-electrical spin injection is the use of a quantum point contact (QPC) [60, 61], in which passing a electric current through a 1D constriction results in a spin-polarized current. A QPC can act as both a spin injector and detector with up to 100% efficiency [5].

The spin Hall effect is another means of electrically generating a spin polarization. The spin analogue to the conventional Hall effect, it results in the accumulation of spin-up and spin-down polarizations along opposite edges of an electrical channel. It was proposed by D'yakonov and Perel' [62], and first measured in semiconductors by Kato *et al.* [63]. The spin accumulations generated in this way are small ($<$10 spins/μm^{-3}) [63], but spin-polarized currents generated by the spin Hall effect were found to persist up to 40 μm away from the region with the electric field [64]. The spin Hall effect can therefore be used for both injection and detection of a spin-polarized current [65].

In this thesis, we will focus on current-induced spin polarization (CISP), in which an in-plane electric field produces a bulk spin polarization in a material. It has been observed in III-V zinc-blende semiconductors, including InGaAs epilayers [8,63], AlGaAs quantum wells [66], and InGaAs/InAlAs quantum wells [67], as well as in III-V wurtzite semiconductor GaN [68] and at room temperature in II-VI zinc-blende semiconductor ZnSe [69]. It is also referred to as the inverse spin-galvanic effect and the Edelstein (or sometimes Rashba-Edelstein) effect. This last name refers to a specific polarization mechanism that will be discussed in more detail in section 6.7.1.

3.6 Conclusion

In this chapter, we have discussed spin dynamics in semiconductors. We began by considering only precession, and then added the contributions due to spin-orbit fields and spin dephasing to the spin dynamics equation. Finally, we discussed several spin polarization mechanisms, ranging from optical to electrical injection.

Although electrical generation of a spin polarization has been measured in InGaAs epilayers, the polarization mechanism has not been determined, since the experimental relationship between the CISP and the spin-orbit fields are contrary to theoretical predictions [8]. In Chapter 6, we will show the results of our measurements of the CISP and the spin-orbit fields in n-type InGaAs and GaAs epilayers of varying indium and carrier concentrations. We will discuss several proposed polarization mechanisms and compare their predictions to the data in order to gain a better understanding of CISP.

Chapter 4

Experimental Methods

4.1 Introduction

In this chapter, we will describe the experimental methods used to measure electron spin dynamics in semiconductor devices. The (In)GaAs samples are patterned with a channel and electrical contacts for the application of an external voltage. A pump-probe optical setup is used for measuring the spin polarization. Finally, *in situ* Hall and Van der Pauw measurements are performed to determine the carrier concentration, resistivity, and mobility of the samples.

Optical measurements of spins are advantageous for a couple reasons: first, optical pumping is a straightforward way to inject a large (up to 50%) spin polarization into a zinc-blende semiconductor, and second, Faraday rotation is a very sensitive way to measure small spin polarizations, down to 1 polarized spin per cubic micron (by comparison, the carrier density is typically 10^4-10^5 μm^{-3}). Measurements can be performed both as a function of pump-probe time delay (time-resolved Faraday Rotation) and magnetic field (resonant spin amplification) in order to determine the spin dephasing time and electron g factor. When a voltage is applied in the plane of the sample, magnetic field scans can also be used to quantify the in-

ternal spin-orbit fields. In the absence of optical pumping, steady-state measurements of the spin polarization as a function of magnetic field are used to characterize the current-induced spin polarization.

4.2 Materials and Sample Fabrication

Although silicon is the most widely used semiconductor in commercial applications, it has an indirect bandgap, which results in low absorption and makes optical measurements difficult. On the other hand, direct band-gap semiconductors like GaAs and its alloys allow for the relatively straightforward measurement of spin dynamics using optical methods.

In this thesis, both GaAs and InGaAs sample were studied. Since indium and gallium are in the same column of the periodic table, indium atoms can simply replace gallium atoms in the crystal lattice. Therefore, InGaAs has the same crystal structure as GaAs, and many of the same properties, such as the bandstructure and optical selection rules. There are two advantages to using samples consisting of an InGaAs epilayer on a GaAs substrate: first, as the bandgap is smaller in InGaAs than in the GaAs substrate, light tuned to the absorption edge of the epilayer will not be absorbed by the substrate, allowing transmission measurements that tend to have better signal-to-noise ratios since much of the scatter from the pump beam is blocked. Second, the lattice constant mismatch between InGaAs and GaAs results in strain in the epilayer, which increases the spin-orbit coupling in the epilayer.

The GaAs samples are taken from commercially grown wafers, consisting of a 500 nm thick epilayer of silicon-doped n-GaAs grown on a (001) GaAs substrate, with an AlGaAs buffer layer in between the epilayer and substrate.

The InGaAs samples consist of a 500 nm thick epilayer of InGaAs grown on a (001) GaAs substrate by molecular beam epitaxy. Both the indium concentration and the concentration of silicon dopants can be varied during the growth process. Indium concentrations ranged

from 2.01 to 3.13 %, and carrier concentrations ranged from 2.7×10^{15} to 2.1×10^{17} cm^{-3} (measured at 30 K).

The InGaAs samples were grown and characterized using x-ray rocking curves by the Goldman group at the University of Michigan. The sample reference numbers are RMBE1129, RMBE1130, RMBE1132, RMBE1301, and RMBE1302.

The lattice constants a and c, parallel and perpendicular to the plane of the sample, are determined from X-ray rocking curves (XRC) [70]. Because InGaAs and GaAs have different lattice parameters, the epilayer will be strained as it tries to match its parallel lattice parameters to that of the substrate. The unstrained lattice constant can be derived from the measured lattice parameters using the Poisson ratio ν of InGaAs:

$$a_{\mathrm{unstrained}} = \frac{-(c(\nu - 1) - 2\nu a)}{1 + \nu} \tag{4.1}$$

The indium concentration x can then be calculated using Vegard's Law:

$$a_{\mathrm{unstrained}} = x a_{\mathrm{InAs}} + (1 - x) a_{\mathrm{GaAs}} \tag{4.2}$$

However, the Poisson ratio in eq. 4.1 is also dependant on the indium concentration x, and so one must iterate between calculating $a_{\mathrm{unstrained}}$ and x until one converges on a solution.

Once x is known, the correct value for $a_{\mathrm{unstrained}}$ can be calculated and compared to the measured a. In this way, the strain relaxation can be calculated:

$$\mathrm{Relaxation} = \frac{a - a_{\mathrm{GaAs}}}{a_{\mathrm{unstrained}} - a_{\mathrm{GaAs}}} \tag{4.3}$$

The InGaAs samples studied in this thesis were found to be nearly pseudomorphic with the substrate, i.e. they had minimal strain relaxation.

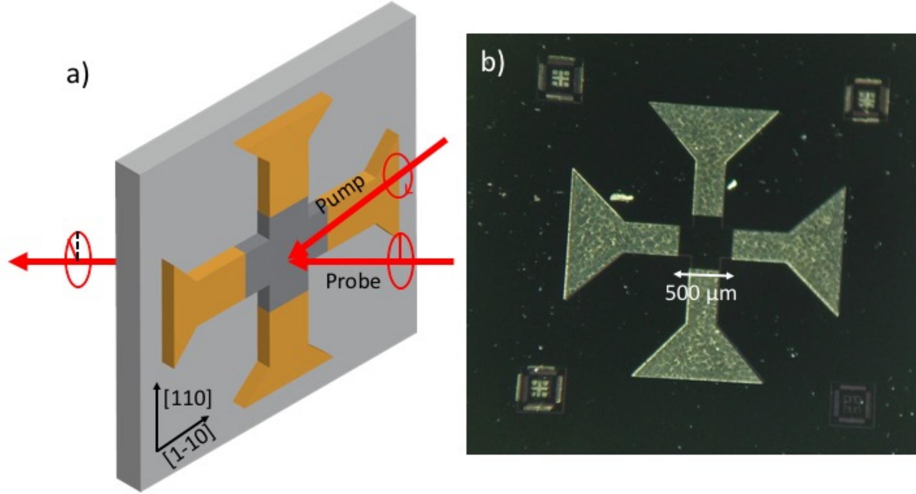

Figure 4.1: a) Schematic of the cross-shaped channel, showing the substrate (light gray), epilayer (dark gray), and contacts (gold). The arms of the cross are aligned along the [110] and [$1\bar{1}0$] crystal axes. The center cross channel is 500 μm in width. b) Photograph of the sample patterned with a cross channel. The features in the corner are alignment markers for photolithography.

The samples are patterned with a cross-shaped channel (Fig. 4.1) [8]. This geometry allows for the application of an electrical field along an arbitrary crystal axis while still optically probing the same spot on the sample. Probing the same spot is particularly important as the indium concentration in the epilayer increases, since the strain relaxation may be inhomogeneous throughout the wafer (see Fig. 5.10 and Table 5.1 in [71]).

Channels are defined on the samples for the application of a voltage in the plane of the sample using standard photolithography procedures and a wet etch. The center cross channel is 500 μm in width. Ohmic gold contacts are deposited and annealed onto the sample in order to attach wires connected to an external voltage source.

4.3 Pump-Probe Optical Setup

A pump-probe optical setup (Fig. 4.2) is used to measure the time-resolved spin dynamics in the samples under study. In short, a circularly polarized pump pulse optically creates a

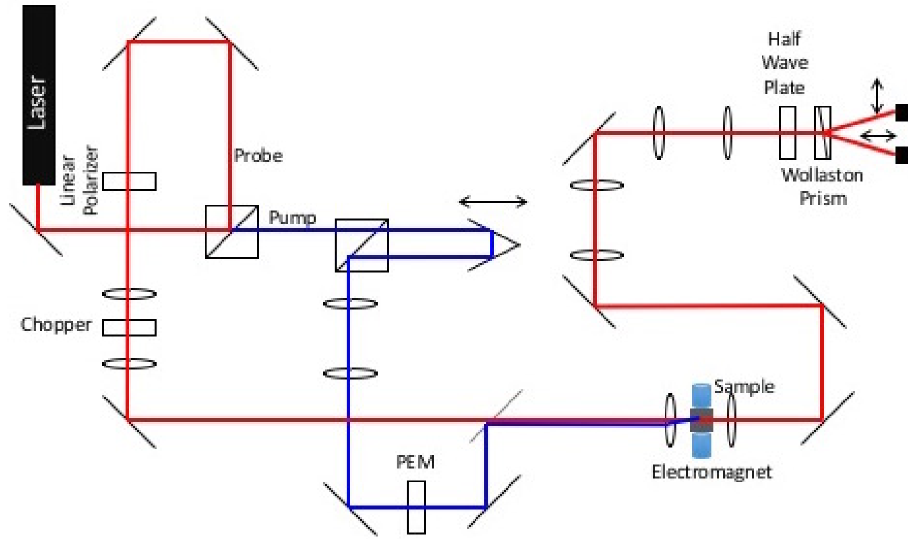

Figure 4.2: Simplified schematic for the optical setup used in pump-probe measurements. The pump (probe) is shown in blue (red).

spin polarization due to optical selection rules (section 2.4), and the Faraday rotation of a linearly polarizated probe beam is measured to determine the spin polarization (section 2.5).

We use a mode-locked tunable-wavelength Titanium:Sapphire laser with a repetition rate of 76 MHz, such that the time between pulses is 13.16 ns, and the temporal pulse width is approximately 3 ps. The wavelength is tuned to the semiconductor bandedge, which is approximately 1.50 eV for the materials studied in this thesis. The beam is split into pump and probe beams with a beamsplitter. The pump is sent along a double-pass mechanical delay line that can vary the time delay between the pump and probe pulses between -500 and 7000 ps. It is then passed through a photo-elastic modulator (PEM), which modulates the polarization of the pump beam between left and right circular polarization at a frequency of 50 kHz. A steering mirror in the path of the pump beam allows for fine control of the position of the pump spot relative to the probe spot, both for alignment purposes (Fig. 4.3) and for spatial scans (Fig. 4.6). Finally, the pump beam is focused onto the sample in order to optically inject a spin polarization.

After the beamsplitter, the probe beam is sent through a linear polarizer and an optical

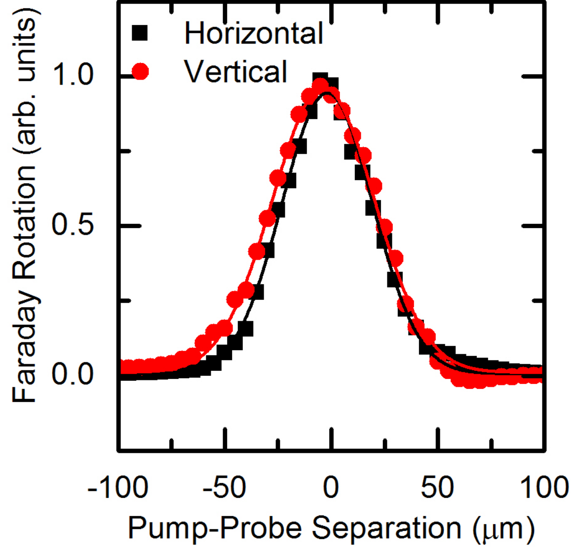

Figure 4.3: Faraday rotation as a function of the position of the pump relative to the probe, both along the horizontal and vertical axis. The curves are fit with Gaussian curves, where the center of the Gaussian gives the position with maximum pump-probe overlap, and the width is used in the conversion from Faraday angle to spin density (section 4.7.1).

chopper, which modulates the intensity of the beam at a frequency of 1370 Hz. The probe beam is then focused onto the sample, and, depending on the nature of the experiment, either the transmitted or reflected beam is collected.

The sample is mounted on the cold finger of a Janis ST-300 continuous flow cryostat. The cold finger has a hole in it to allow the transmission of light. The cryostat is mounted on a motorized three-axis translation stage for precise and repeatable positioning of the laser spot on the channel and of the sample at the focus of the laser. Figure 4.4 shows a scan of the Faraday rotation of the probe as the translation stage is scanned along the horizontal and vertical axes. Only the regions where the epilayer has not been etched away have non-zero Faraday rotation. By mapping out the channel in this way, we can repeatably find the center of the channel. The cold finger is placed between the poles of an electromagnet that can achieve fields up to 350 mT. For reflection measurements, the cryostat is rotated slightly so that the sample is not completely normal to the incident beam in order to spatially

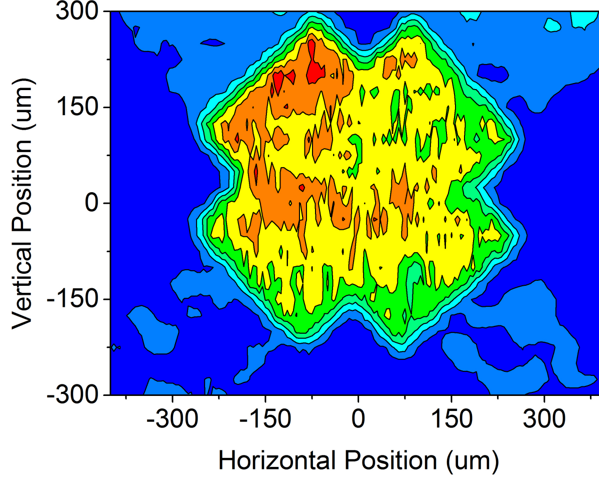

Figure 4.4: Two dimensional spatial scan of the Kerr rotation on a sample patterned with a cross channel. Dark blue areas are regions in which the epilayer has been etched away and so there is no induced Faraday rotation. The bright region in the center shows the cross-shapped channel. Light blue regions at the ends of the cross are regions where the epilayer has not been etched away but that are covered by gold contacts, which are highly reflective. The Kerr rotation is larger on the right side since the sample must be slightly tilted for reflection measurements.

separated the incident and reflected beams. A flip mirror in the collection path is used to change between the transmission and reflection geometries.

The vertical and horizontal components of the linearly polarized transmitted (reflected) probe beam are separated using a Wollaston prism and sent to two photodiodes. A half wave plate before the Wollaston prism is used to "balance" the photodiode bridge, i.e. to rotate the polarization of the light such that initially the vertical and horizontal components have equal intensity. In this way, the setup measures the Faraday angle as small fluctuations of the polarization about the polarization angle $\theta = \frac{\pi}{4}$.

Using Jones calculus, the polarization of the electric field of the transmitted probe light can be written as

$$\mathbf{E} = E_0 \begin{pmatrix} \cos(\theta_F + \frac{\pi}{4}) \\ \sin(\theta_F + \frac{\pi}{4}) \end{pmatrix} \tag{4.4}$$

where θ_F is the Faraday angle. The photodiodes measure the intensities of the vertical and

horizontal components:

$$I_x = I_0 \cos^2(\theta_F + \frac{\pi}{4}) = \frac{I_0}{2}(1 - \sin(2\theta_F)) \tag{4.5}$$

$$I_y = I_0 \sin^2(\theta_F + \frac{\pi}{4}) = \frac{I_0}{2}(1 + \sin(2\theta_F)) \tag{4.6}$$

And so we have

$$\sin(2\theta_F) = \frac{I_y - I_x}{I_y + I_x} \tag{4.7}$$

The Faraday angles we measure are very small (<100 μrad) and so the small angle approximation can be employed to give the final result

$$\theta_F = \frac{I_y - I_x}{2(I_y + I_x)} \tag{4.8}$$

A subtraction circuit is used to find the difference in the intensities $I_y - I_x$. The difference is then measured using a cascaded lock-in amplifier setup. The first lock-in filters the signal at the higher modulation frequency, i.e. the 50 kHz modulation from the PEM. The Fast X output of the first lock-in is then used as the input for the second lock-in, which filters the signal at the frequency of the optical chopper (1370 Hz). In this way, we only measure the component of the signal that is modulated by both the PEM and chopper. This cascaded lock-in detection technique improves the signal-to-noise ratio significantly, as well as allowing measurements to be performed with the room lights on.

Since the total intensity $I_y + I_x$ is constant, if the absolute amplitude of the Faraday angle is not important to the measurement, then we just need to measure the difference $I_y - I_x$. However, if we wish to know the Faraday angle in units of radians, e.g. to convert between the Faraday angle and a spin density (see section 4.7.1), then we must also measure I_x and I_y. To do this, the signal from each photodiode is measured using the analog-to-digital converters in the lock-in amplifier.

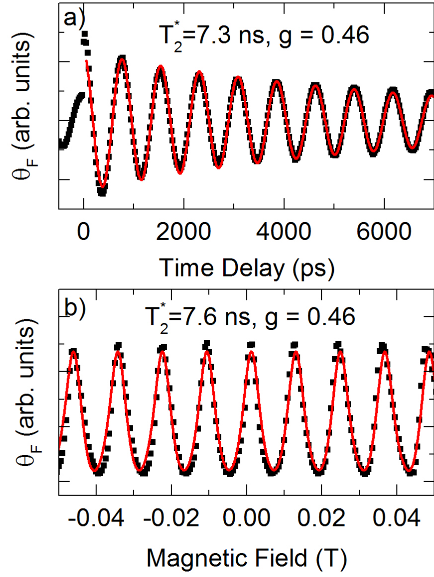

Figure 4.5: Time-resolved Faraday rotation and resonant spin amplification. (a) Time resolved Faraday rotation with an external magnetic field of 0.2 T. (b) Resonant spin amplification at a time delay of $\Delta t = -160$ ps. Both data sets are fit to eq. 4.9 in order to determine the g factor and dephasing time. Data from an $In_{0.02}Ga_{0.98}As$ sample with $n = 2.7 \times 10^{15}$ cm^{-3} at 30 K.

.

Neutral density filters in both the pump and probe paths are used to reduce the intensity of the beams. The probe beam is set to a low power (~100 μW) to minimize perturbations to the sample. Higher pump power gives greater signal; however, if the pump power is too high the pump has a higher chance of repolarizing spins from the previous pulse that have not yet completely dephased [72]. This results in an artificially low fit result for the lifetime from time delay scans. However, this does not affect magnetic field scan fits. This repolarization is only significant above a certain threshold power, and so care must be taken to set the pump power below this threshold. In our measurements, the pump power is usually set to 1 mW. When focused on the sample, the spot size of both the pump and probe beams is ~ 25 μm in diameter.

4.4 Time-Resolved Faraday Rotation

In time-resolved Faraday rotation (TRFR), the Faraday rotation is measured as a function of the time delay between the pump and probe pulses. This is described by the equation:

$$\theta_F(\Delta t, B) = \sum_n A e^{-(\Delta t + n t_{\mathrm{rep}})/T_2^*} \cos\left[\frac{g\mu_B}{\hbar} B(\Delta t + n t_{\mathrm{rep}})\right] \tag{4.9}$$

where A is the amplitude, Δt is the time delay between the pump and probe, t_{rep} is the time between laser pulses (13.16 ns), T_2^* is the dephasing time, g is the electron g factor, and B is the applied magnetic field. The total signal is a sum of n subsequent laser pulses as the spin polarizations from previous pump pulses may not have completely dephased by the time the next pump pulse hits (if the dephasing time is long enough). If the spin lifetime is comparable to, or greater than, the laser repetition rate, one must also take into account an effective phase shift due to the effect of the previous pump pulses [73].

Measurements are perfomed by fixing the external magentic field (usually at 0.2 T) and scanning the time delay between the pump and the probe pulses. From TRFR scans, we can determine the dephasing time of the spins from the decay of the signal, and the g-factor from the oscillation frequency.

4.5 Resonant Spin Amplification

In the previous section, the time delay was scanned while sitting at a fixed external magnetic field. Alternatively, the external magnetic field can be scanned while sitting at a fixed time delay [74]. When the magnetic field is such that the oscillations of the spins excited by the previous pump pulses are in phase with the oscillations of spins excited by the last pump pulse, the total signal is maximized. Conversely, if the oscillations are out of phase, the total signal is decreased. For this reason, magnetic field-dependent measurements of the Faraday

rotation are referred to as resonant spin amplification (RSA).

RSA can be described by the same equation as the time-domain measurements (Eq. 4.9). The dephasing time is determined from the width of the peaks (longer dephasing time results in sharper peaks) and the g-factor from the frequency of the peaks.

The peaks all have the same amplitude when $\Delta t = t_{\text{rep}}$, simplifying the fitting process. However, at $\Delta t = 0$ there may be additional effects not well described by Eq. 4.9 due to the pump pulse and carrier recombination. Therefore, RSA scans (and other magnetic field scans, like spin drag scans (section 4.6)) are usually taken at a slightly negative time delay of $\Delta t =$ -160 ps.

If the dephasing time of the spins is greater than the time delay accessible by the delay line, it becomes difficult to fit for the dephasing time using time-resolved scans. However, RSA scans do not have the same limitation. Therefore RSA scans are a more accurate way to measure long-lifetime samples.

4.6 Spin Drag for Measurement of the Spin-Orbit Fields

Magnetic field scans also have an advantage over time-resolved scans when performing voltage dependent measurements.

Since the pump beam has a spatial profile, it will produce a spin polarization only in a localized area. This localized spin polarization is referred to as a "spin packet". If we were to perform time-resolved measurements with an applied voltage, the spin packet would move out of the probe spot as the time delay is increased. Since magnetic field scans are performed at a fixed time delay, the spin packet sits at a fixed position throughout the measurement.

However, we do not necessarily know *where* the spin packet is centered, since we use these measurements to quantify the spin mobility. Therefore, the magnetic field scans are performed as a function of pump-probe spatial separation (Fig. 4.6). This set of measure-

ments is referred to as a "spin drag" measurement [75].

The spin drag data is fit to a modified version of Eq. 4.9.

$$\theta_F(\Delta t, B, x) = \sum_n A_n(x) \cos\left[\frac{g\mu_B}{\hbar} \left|\mathbf{B}_{\text{ext}} + \mathbf{B}_{\text{SO}}\right| (\Delta t + nt_{\text{rep}})\right] \tag{4.10}$$

Here the amplitude has been replaced with a spatial-dependent amplitude that is different for each previous pump pulse (as each previous pulse has had nt_{rep} more time to drift). The magnetic field has been replaced by the vector sum of the external magnetic field and the internal, spin-orbit magnetic field. If we write out this term, we get

$$\left|\mathbf{B}_{\text{ext}} + \mathbf{B}_{\text{SO}}\right| = \sqrt{(B_{\text{ext}} + B_{\text{SO},\,\parallel})^2 + B_{\text{SO},\,\perp}^2} \tag{4.11}$$

where $B_{\text{SO},\,\parallel}$ and $B_{\text{SO},\,\perp}$ are the components of the SO field that are parallel and perpendicular to the external magnetic field, respectively. The parallel component has the effect of shifting the entire curve horizontally, whereas the perpendicular component has the effect of decreasing the magnitude of the peak at $B_{\text{ext}} = 0$. One can also see that the sign of the magnetic field can only be determined for the parallel component of the SO field.

Since the positioning of our steering mirror is more repeatable in the horizontal direction, generally measurements for the magnitude of the SO field are performed with the channel oriented horizontally with respect to the lab frame and parallel to the external magnetic field. For the crystal axes being studied (i.e. the [110] and $[1\bar{1}0]$ crystal axes), the SO field is purely perpendicular to the external magnetic field (section 3.3). However, in order to correctly calculate the SO parameters α and β, it is important to know the sign of the SO field, and so measurements are also performed with the channel oriented vertically and perpendicular to the external magnetic field solely for this purpose.

A full spin drag scan as in Fig. 4.6 is repeated for several in-plane voltages, and the data is fit to Eq. 4.10 in order to get the values of $A_0(x)$, $g(x)$, $B_{\text{SO},\perp}(x)$, and $B_{\text{SO},\parallel}(x)$ for each

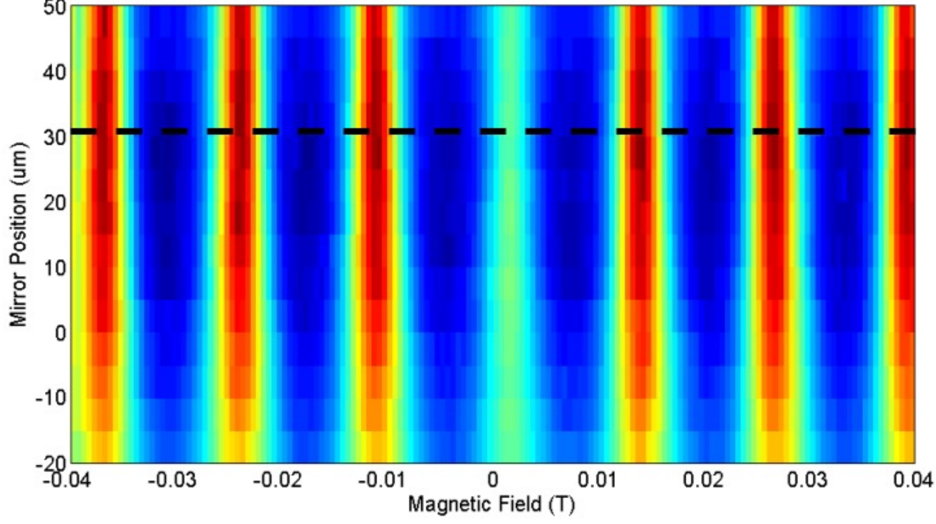

Figure 4.6: Spin drag measurements. Faraday rotation as a function of magnetic field and pump-probe spatial separation with a voltage applied in the plane of the sample. Dashed line indicates the center of the spin packet, which has drifted $\sim 30\ \mu$m due to the applied voltage. The decrease in the magnitude of the center peak is due to spin-orbit effects.

pump-probe separation x.

$A_0(x)$ vs x (Fig. 4.7a) can be fit with a Gaussian, where the center of the peak shifts as the voltage is increased due to the drift of the electrons. The center of the Gaussian, x_c, is the position of the spin packet at time Δt, which is set to 13 ns for this set of experiments. The drift velocity $v_d = x_c/(13\text{ ns})$ increases linearly with applied voltage (Fig. 4.7b), and so we can calculate the mobility μ from the slope. In general, the voltage-dependence of quantities such as the SO field and g factor will be given in terms of the change with drift velocity in order to account for differences in mobility between different samples.

$B_{\text{SO},\perp}(x)$ and $B_{\text{SO},\parallel}(x)$ have a linear dependence with x (Fig. 4.7c) [36]. This is because electrons in the leading edge of the spin packet have a velocity larger than the average, and so "see" a larger SO field. A linear fit of $B_{\text{SO}}(x)$ vs x is used to calculate $B_{\text{SO}}(x_c)$, the magnitude of the SO field at the center of the spin packet. This is the value used for the strength of the SO field $B_{\text{SO}}(v_d)$, the drift velocity corresponding to that x_c.

In these samples, $B_{\text{SO}}(v_d)$ is found to be linear in the drift velocity v_d (Fig. 4.7d),

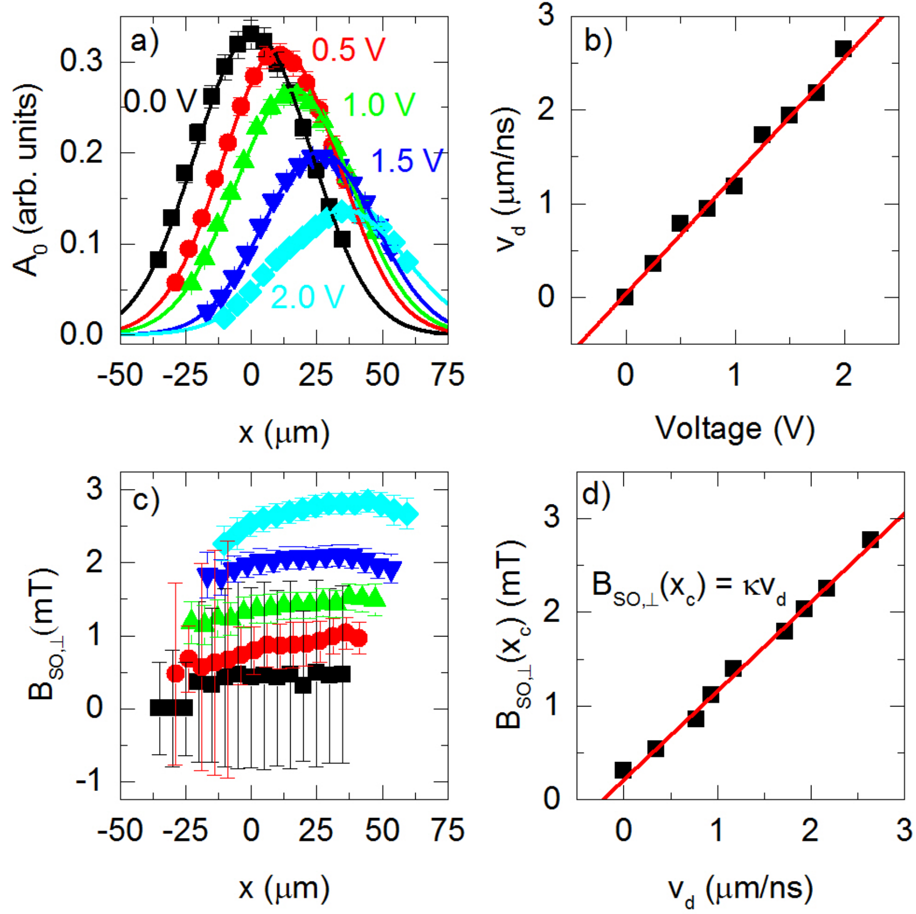

Figure 4.7: Fits for the spin orbit fields. (a) $A_0(x)$ vs x fit with a Gaussian curve in order to find the center of the spin packet x_c. (b) The drift velocity v_d for each applied voltage. (c) Fits for the perpendicular component of the spin-orbit field $B_{\text{SO},\perp}$ for each pump-probe separation at several applied voltage. (d) The magnitude of the SO field at the center of the spin packet $B_{\text{SO}}(x_c)$ for each corresponding drift velocity. The slope κ is used to characterize the strength of the spin orbit field.

indicating that the higher order terms in the SO Hamiltonian can be neglected. This data is fit to the equation $B_{\mathrm{SO}}(v_d) = \kappa v_d$, where κ is the parameter used to quantify the strength of the SO field. This measurement is repeated for voltages across different crystal axes in order to get the values of κ for the different crystal axes.

The SO parameters α and β can be calculated if κ is known for voltages along the [110] and [1$\bar{1}$0] crystal axes.

$$\alpha = \frac{g\mu_B}{2}(\kappa_{[110]} - \kappa_{[1\bar{1}0]}) \tag{4.12}$$

$$\beta = \frac{g\mu_B}{2}(\kappa_{[110]} + \kappa_{[1\bar{1}0]}) \tag{4.13}$$

From these equations, it is clear that it is important to determine the sign of the SO field, and therefore κ, in order to correctly calculate the values for α and β.

4.7 Current-Induced Spin Polarization Measurements

CISP is measured by the Faraday rotation induced in a sample by an electric field applied in the plane of the sample in the absence of optical pumping. The experimental setup is similar to that described in section 4.3 with a couple of modifications. The pump beam must be blocked, and the chopper is turned off in order to double the signal going into the photodiodes. Instead of a DC voltage, as in spin drag measurements, low frequency voltage is applied across the sample for lock-in detection.

For CISP, the spin polarization is generated in the plane of the sample, so that the cosine in the basic spin dynamic equation (Eq. 4.9) becomes a sine:

$$S_z(t) = \gamma e^{-t/\tau} \sin(\Omega_L t) \tag{4.14}$$

where $S(t)$ is the spin density along the probe axis, γ is the number of spins generated per unit time per unit volume, τ is the transverse spin lifetime, and Ω_L is the Larmor precession

frequency. Since the pump is blocked, there is no need to sum over successive pump pulses. The steady-state spin density along the probe axis is thus

$$\rho_z = \int_0^\infty \gamma e^{-t/\tau} \sin(\Omega_L t) dt = \frac{\rho_{\mathrm{el}} \Omega_L \tau}{(\Omega_L \tau)^2 + 1} \tag{4.15}$$

where $\rho_{\mathrm{el}} = \gamma\tau$ is the steady-state electrically generated spin density, and ρ_z is the steady state spin density along the probe axis. When magnetic field scans are performed, we see an odd-Lorentian curve in which the amplitude is related to the spin density and the width is related to the spin lifetime.

Measurements of CISP as a function of magnetic field are performed for various in-plane voltages. Generally, several magnetic field scans are performed and averaged over for each voltage since the CISP signal can be very small ($\sim 1\mu$rad).

The data is then fit with Eq. 4.15 in order to get the values of ρ_{el} and τ for each applied voltage. From these values, the spin generation rate γ can be calculated. As above, these values are plotted as a function of the drift velocity, not the voltage, in order to account for differences in mobility between samples. ρ_{el} increases with applied voltage up to a saturation point, and the spin lifetime τ decreases with applied voltage. γ has a linear dependence with drift velocity, and the slope η is used to characterize the electrical spin generation efficiency. This measurement is repeated for voltages across different crystal axes in order to get the values for η for the different crystal axes.

4.7.1 Converting Faraday rotation to spin densities

The spin polarizations are measured in terms of the Faraday rotation they induce in the transmitted probe beam. However, when comparing the CISP in different samples, it is important to convert from the Faraday angle to a spin density in order to account for the differences in optical properties of the samples.

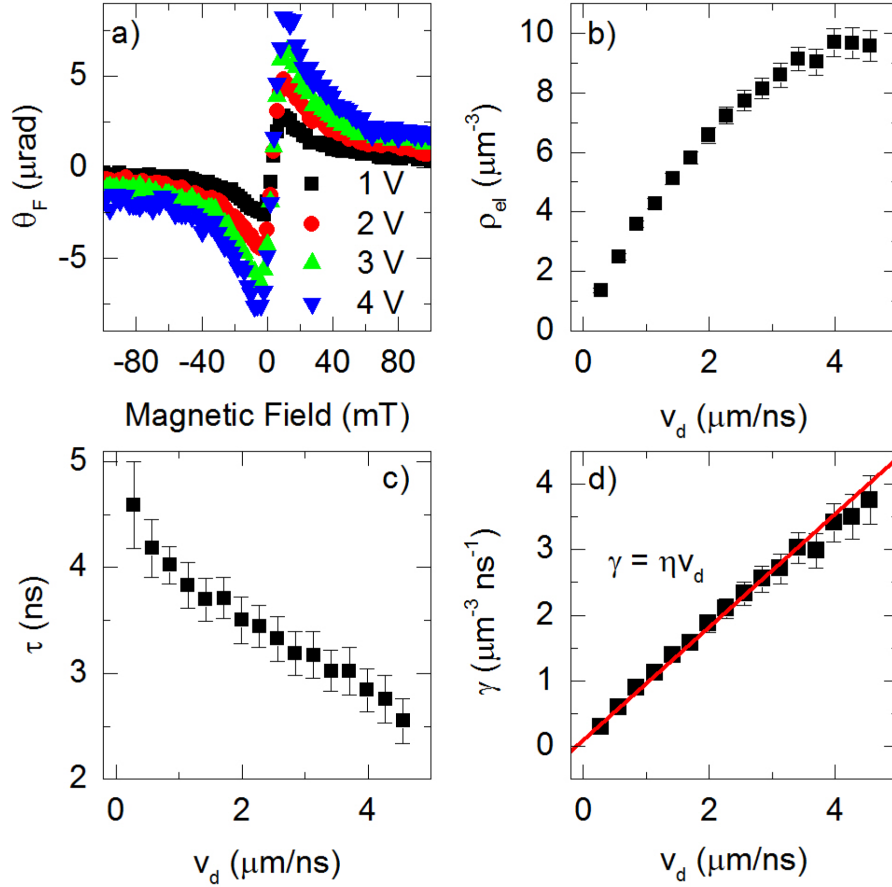

Figure 4.8: Current induced spin polarization. (a) Faraday rotation in the absence of optical pumping as a function of magnetic field for various in-plane voltages. The Faraday rotation is converted to a spin density and the CISP curves are fit to find (b) the steady state spin density ρ_{el} and (c) the transverse spin lifetime τ for the drift velocity corresponding to each applied voltage. (d) The spin density generated per unit time γ versus the drift velocity. The slope η is the spin generation efficiency.

The conversion factor between the Faraday angle and the spin density can be calculated by comparing electrical spin injection to optical spin injection [63].

As discussed in section 2.4, optical injection results in a 50% spin polarization. The total number of spins polarized per laser pulse is given by

$$n_{\text{op}} = \frac{1}{2}\alpha\left(\frac{P_{\text{pump}}}{f_{\text{rep}}}/2\pi\hbar\frac{c}{\lambda}\right) \tag{4.16}$$

where α is the absorption of the epilayer, P_{pump} is power of the pump spot, and f_{rep} and λ are the repetition rate and wavelength of the laser respectively. α is calculated by measuring the powers of the incident, transmitted, and reflected beams. In InGaAs samples, the bandgap of the epilayer is smaller than the bandgap of the GaAs substrate, and so a laser turned to the absorption edge of the epilayer will not be absorbed by the substrate. Therefore, all absorption of the incident laser can be attributed to the InGaAs epilayer. However, in the GaAs samples, the epilayer and substrate absorb at similar wavelengths. Because of this, we cannot calculate α for these samples and so data for those samples will be given only in terms of the Kerr angle, not the spin density.

The optically injected spin density is given by

$$\rho_{\text{op}} = n_{\text{op}}/\left(2\pi\sigma_x\sigma_y d\right) \tag{4.17}$$

where ρ_{op} is the density of optically polarized spins, σ_x and σ_y are the widths of the Gaussian profile of the pump spot (see Fig. 4.3), and d is the thickness of the epilayer.

The Faraday rotation due to optical injection is given by

$$\theta_{\text{op}} = Ad\iint\left[\rho_{\text{op}}e^{-\left(\frac{x^2}{2\sigma_x^2}+\frac{y^2}{2\sigma_y^2}\right)}e^{-\left(\frac{x^2}{2\sigma_x^2}+\frac{y^2}{2\sigma_y^2}\right)}\right]dxdy = \pi Ad\rho_{\text{op}}\sigma_x\sigma_y \tag{4.18}$$

where the two exponents account for the spatial profiles of the pump and probe beams,

and A is a proportionality factor.

Now we must find the relationship between the electrically injected spin density and Faraday rotation. The electrically induced Faraday rotation is given by

$$\theta_{\text{el}} = Ad \iint \left[\rho_{\text{el}} e^{-\frac{x^2}{2\sigma_x^2} - \frac{y^2}{2\sigma_y^2}} \right] dxdy = 2\pi Ad\rho_{\text{el}}\sigma_x\sigma_y \tag{4.19}$$

By equating the A in Eq. 4.18 and 4.19, we arrive at the relationship

$$\rho_{\text{el}} = \frac{\theta_{\text{el}}\rho_{\text{op}}}{2\theta_{\text{op}}} \tag{4.20}$$

where θ_{el} and θ_{op} are the measured Faraday angles, and ρ_{op} can be calculated using Eqs. 4.16 and 4.17.

4.8 Hall and Van der Pauw Measurements

We are interested in understanding the relationship between the electrical properties of a sample (namely its mobility and carrier concentration) and the electrical spin generation efficiency. Since the temperature and lighting conditions can have a large effect on the electrical properties of the materials, *in situ* Hall and Van der Pauw measurements allow us to measure these quantities under the same conditions in which the spin polarization is measured for a better comparison.

The Hall effect is the appearance of a transverse voltage when a magnetic field is applied perpendicular to an electrical current. It is a result of the cyclotron motion of electrons in a magnetic field.

In a traditional Hall bar, both the voltages transverse and parallel to the applied current can be measured at the same time (Fig. 4.9, left). The carrier concentration and resistivity

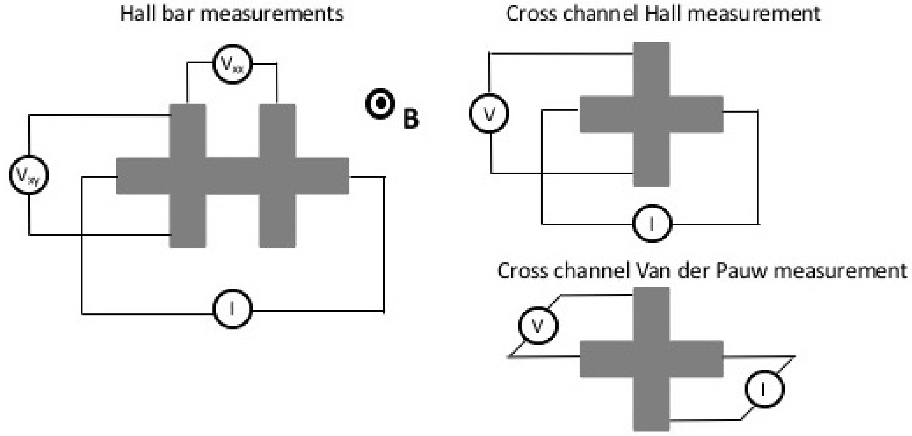

Figure 4.9: Hall measurements with a Hall bar and cross channel. Left: Traditional Hall bar, in which a current is applied across the horizontal channel, and both the transverse and parallel voltage can be measured at the same time. Right: For a cross-shaped channel, we must perform two separate measurements. In the Hall measurement, the voltage transverse to the applied current is measured, and in the Van der Pauw measurement, the voltage parallel to the applied current is measured. For the Hall bar measurement and the cross channel Hall measurement, an external magnetic field is applied out of the plane of the sample. There is no magnetic field applied during Van der Pauw measurements.

of the sample can be calculated from these two voltages:

$$n = \frac{IB}{V_{xy}ed} \tag{4.21}$$

$$\rho = \frac{V_{xx}}{I}\frac{A}{l} \tag{4.22}$$

where I is the applied current, V_{xx} and V_{xy} are the parallel and transverse voltages respectively, B is the external magnetic field, e is the carrier charge, and d, l, and A are the thickness, length, and area of the channel respectively.

The mobility can be calculated from these two quantities with the equation

$$\mu = \frac{1}{ne\rho} \tag{4.23}$$

In order to determine n, ρ, and μ for our cross channel samples, we must use two separate

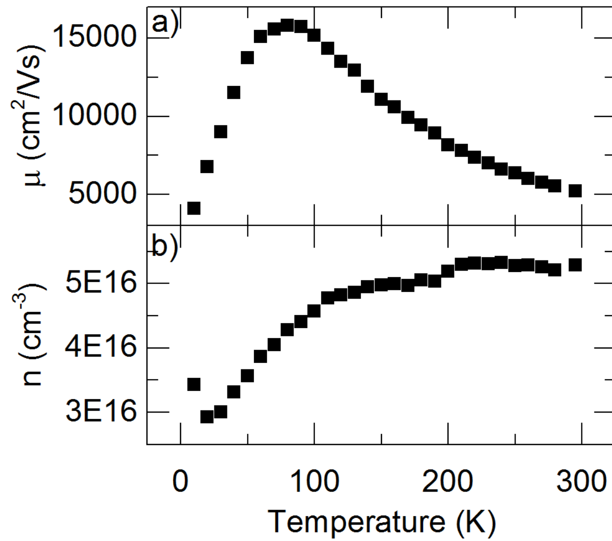

Figure 4.10: a) Mobility and b) carrier concentration of GaAs as a function of temperature, taken with the *in situ* automated Hall and Van der Pauw measurement system.

wiring configurations in order to measure V_{xx} and V_{xy} (Fig. 4.9, right). Furthermore, because of the symmetry of the cross channel, there are two equivalent wiring configurations for Hall measurements, and four equivalent wiring configurations for Van der Pauw measurements. In order to automatically switch between the six different wiring configurations, we employed a computer controlled switch board. A fully automated Hall measurement LabView program is used to switch the wirings between configurations, as well as repeat the measurements for positive and negative currents and magnetic fields, and for different magnitudes of current.

Figure 4.10 shows the result of these measurements for a GaAs sample etched with a cross channel as a function of temperature. The temperature dependence of the mobility (Fig. 4.10a) is affected by the temperature dependence of the dominant scattering mechanisms. Ionized impurity scattering dominates at low temperatures [76] and polar optical phonon scattering dominates at high temperatures [17]. The large change in mobility and carrier concentration over the temperature range spanning from 10 K to 295 K (room temperature) demonstrates the importance of measuring these quantities at the temperature at which the

spin measurements are performed.

4.9 Conclusion

In this chapter, we have covered the fabrication and characterization of the semiconductor samples under study, as well as the measurements of the spin dynamics, spin-orbit coupling, and current-induced spin polarization. In the following two chapters, we will use these techniques to demonstrate the electrical modification of the electron g factor in InGaAs epilayers, and to study the dependence of the current-induced spin polarization in InGaAs epilayers on indium and carrier concentrations.

Chapter 5

Voltage Dependent g-Factor

5.1 Motivation

As spin is essentially a magnetic property of electrons, the simplest way to manipulate an electron's spin is with a magnetic field. The strength of the interaction between the magnetic field and the spin is quantified by the g factor. Just as the effective mass of an electron varies from material to material, so does the electron g factor. Furthermore, the g factor changes as a function of magnetic field [74] and temperature [32]. In this chapter, we will report on the modification of the electron g factor by an in-plane electric field in bulk InGaAs. The work covered here was published in [77] (©2015 American Physical Society).

In the pursuit of a semiconductor spintronic device, local manipulation of the g factor allows for local control of spins. Electron spin resonance (ESR) was shown to induce spin flips in a quantum dot when the frequency of an oscillating magnetic field matched the resonance frequency of the spin in a perpendicular static magnetic field, $g\mu_B B_{\text{stat}} = hf_{\text{osc}}$ [78]. As this technique requires high magnitude, high frequency magnetic fields, alternative methods were developed that instead used an alternating electric field to produce the resonance, either by creating a oscillating spin-orbit (SO) field [79] or by electrically modulating the g-tensor,

called g-tensor modulation resonance (g-TMR) [33]. The use of an electric field also allows for more local manipulation than is possible with magnetic fields [80].

g-TMR requires electrical control of the g-factor, which has been demonstrated in quantum wells (QWs) [81] and quantum dots (QDs) [82], but not in bulk materials. In QWs and QDs, the change in the g factor is often attributed to an electric-field induced shift of the wave function into the barrier, which has a different g factor. In this chapter, we demonstrate electrical control of the g factor in a bulk $In_{0.026}Ga_{0.974}As$ epilayer. We characterize the g factor dependence on the in-plane electric field and drift velocity using magnetic field and spatially-resolved pump-probe Faraday rotation spectroscopy. Our data reveal an electric field dependence of the g factor in bulk InGaAs while distinguishing changes in the g-factor from changes in the spin-orbit field. This electric field dependence must be due to a different mechanism than the wave function shift responsible for the g factor tuning in QWs [81]. A change in the g factor with in-plane electric field was recently reported in a QW [83].

Understanding the change in the g factor as a function of the electric field is also important to correctly determine the magnitude of the internal fields produced by spin-orbit coupling and nuclear spin polarization. Fits for the internal fields from time-resolved Faraday/Kerr rotation data [84–86] assume that the g factor is constant in order to separate it from the effects of changes in the internal fields. In Ref. [87], the g factor is known not to change, but the precession frequency changes due to a change in the internal fields by an electric field. However, this is referred to as an effective tuning of the g factor, using the relationship $g_{\text{eff}}(E)B_{\text{ext}} = g\,[B_{\text{ext}} + B_{\text{int}}(E)]$. Our measurement technique enables us to distinguish between changes in the g factor from changes in the SO field.

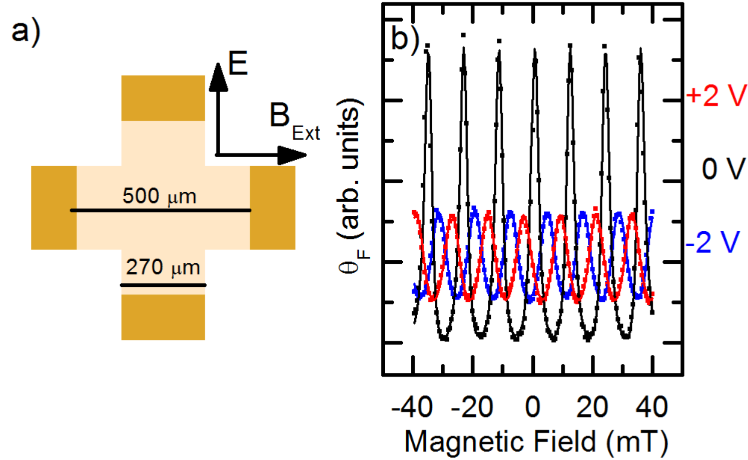

Figure 5.1: Channel geometry and magnetic field scans. (a) Cross pattern with arms along [110] and [1$\bar{1}$0] was etched on the sample, with contacts shown in gold. The electric field was always applied perpendicular to the external magnetic field. (b) Faraday rotation data as a function of external magnetic field for applied voltages of -2 V (blue), 0 V (black), and 2 V (red) and fits to Eq. 5.1.

5.2 Sample Structure and Experimental Methods

Measurements were performed on a 500 nm thick Si-doped $In_{0.024}Ga_{0.976}As$ epilayer. Hall measurements performed at 30 K determined that the carrier density is 1.6×10^{16} cm^{-3}. A cross-shaped channel with arms along the [110] and [1$\bar{1}$0] crystal axes was patterned onto the sample using standard photolithography techniques. Measurements were performed with the axis of interest oriented perpendicular to the external magnetic field, such that the internal SO field is expected to be purely parallel to the external field.

A pump-probe optical setup, as described in section 4.3, was used to measure the g factor of the spins. The laser was tuned to 839.43 nm, and measurements were performed at 30 K. A circularly polarized pump pulse optically injects a spin polarization, and after some time delay Δt, the Faraday rotation of a linearly polarized probe pulse is used to measure the spin polarization. Time-resolved Faraday rotation measurements are unable to distinguish between changes in the precession frequency due to changes in the g factor versus changes

due to changes in the SO fields. Thus, scans of the Faraday rotation as a function of external magnetic field were performed instead.

As explained in section 4.6, when an in-plane voltage is applied across the sample, magnetic field scans are performed at different pump-probe spatial separations in order to determine the position of the spin packet induced by the pump pulse. The data is then fit with the equation

$$\theta_k(B_{ext}, x) = \sum_n A_n(x) \cos\left[\frac{\mu_B}{\hbar}\sqrt{g_{\parallel}^2\left(\mathbf{B}_{\text{ext}} + \mathbf{B}_{\parallel}\right)^2 + g_{\perp}^2\mathbf{B}_{\perp}^2}(\Delta t + nt_{\text{rep}})\right] \tag{5.1}$$

where $\mathbf{B}_{\parallel}$ and $\mathbf{B}_{\perp}$ are the components of the internal field parallel and perpendicular to the external field, respectively. This equation is only valid if the parallel and perpendicular directions are eigenstates of the g factor tensor (i.e., [110] and $[1\bar{1}0]$).

Varying Δt at a fixed B_{ext} results in oscillations that are periodic in $\frac{g\mu_B}{\hbar}|\mathbf{B}_{\text{ext}} + \mathbf{B}_{\text{int}}|$. If instead Δt is fixed and B_{ext} is varied, then the oscillations are periodic in $\frac{g\mu_B}{\hbar}\Delta t$.

The components of the internal field parallel and perpendicular to the external field shift the curve (Fig. 5.1b) and decrease the magnitude of the center peak respectively, whereas the g-factor changes the frequency of the peaks. In this way, unlike in time-resolved measurements, we can separately determine the g factor and the SO field.

The average drift velocity (v_d) of the electrons can be calculated as a function of voltage from the center position (x_c) of the amplitude and the known temporal separation of the pump and probe pulses. From measurements of the drift velocity as a function of applied electric field, we determine the effective mobility, using the equation $\mu_{\text{eff}} = v_d/E_{\text{applied}}$, to be 6200 ± 200 cm^2/(V s) along the [110] direction and 5070 ± 20 cm^2 /(V s) along the $[1\bar{1}0]$ direction. The difference in mobilities along the two directions comes from a discrepancy between the total applied voltage and the actual voltage across the channel, as there is likely also a voltage drop across the contacts that is different for different contacts. As such, all

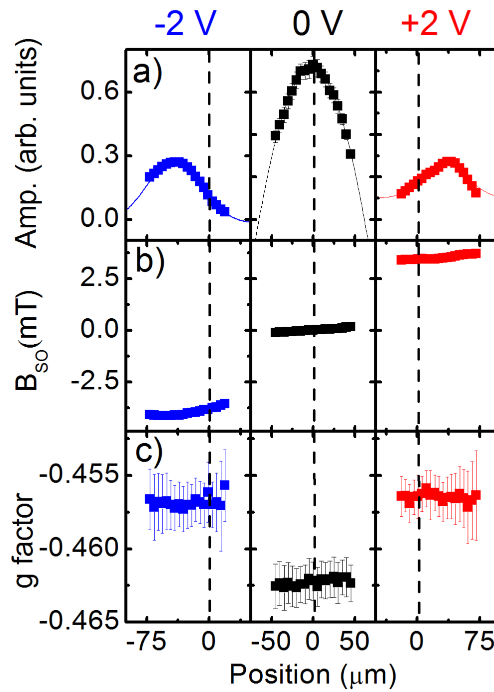

Figure 5.2: Spin drag fits of the SO field and g factor. (a) Amplitude of the Faraday rotation, (b) fits of the internal field, and (c) fits of the g factor as a function of pump-probe separation for -2 V, 0 V, and +2 V along [110].

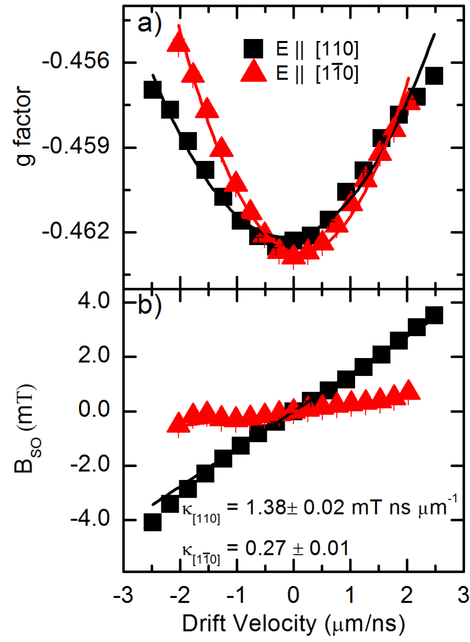

Figure 5.3: g factor and SO fields as a function of drift velocity. (a) g factor as a function of electric field (shown in terms of the drift velocity) for the [110] and [1$\bar{1}$0] directions. The parabolic fits to the g factor are a guide to the eye and are less accurate at higher drift velocities. (b) The internal field magnitude as a function of drift velocity. The slopes of the lines give the SO field proportionality constant κ.

electric field dependent measurements are presented in terms of the drift velocity, which we can measure directly.

The SO field was determined using the method described in Ref. [8]. Magnetic field scans of the Faraday rotation as a function of the external magnetic field, as shown in Fig. 5.1b, were fit with Eq. 5.1 in order to determine the amplitude of the spin packet, the magnitude of the SO field, and the magnitude of the g factor (Fig. 5.2). The internal fields were found to be perpendicular to the direction of the current for both [110] and [$1\bar{1}0$], as is expected for these directions. The SO field proportionality constants were found to be 1.38 ± 0.02 mT ns μm^{-1} for an electric field applied along [110] and 0.27 ± 0.01 mT ns μm^{-1} along [$1\bar{1}0$] [Fig. 5.3].

The g factor was also extracted from the external magnetic field scan at each pump-probe spatial separation [Fig. 5.2]. The g factor at the center of the spin packet is plotted versus the drift velocity v_d [Fig. 5.3]. Parabolic fits are shown as a guide to the eye. However, a numerical derivative shows that this fit is less accurate for larger drift velocities. Measurements conducted along the [110] and [$1\bar{1}0$] crystal axes show similar curvatures: $(1.05\pm0.62)\times10^{-3}/(\mu\text{m})^2$ for [110] and $(1.72\pm0.76)\times10^{-3}/(\mu\text{m})^2$ for [$1\bar{1}0$].

Reference [88] indicates that the energy dependence of the g factor in GaAs is given by $g^*(E) = g^* + 6.3\ \text{eV}^{-1}E$. If we assume a parabolic dispersion relation for our values of k, then our measured dependence on the energy, taken from electric-field dependent measurements, is more than 500 times larger.

Measurements for both positive and negative v_d show that the change in g factor is symmetric about zero drift velocity [Figs. 5.3a and 5.4a], and thus only depends on the magnitude of v_d , not the direction.

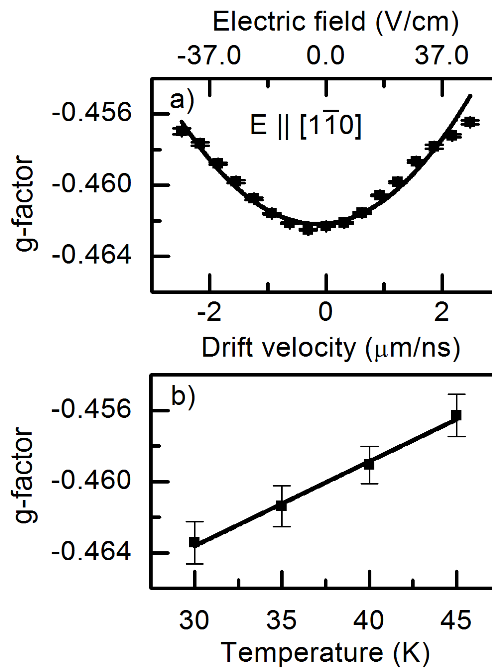

Figure 5.4: g factor versus temperature. (a) g factor as a function of drift velocity along [1$\bar{1}$0] at 30 K, with a parabolic fit as a guide to the eye. (b) Temperature dependence of the g factor for v_d = 0. The change in g factor due to an applied voltage of 2 V at 30 K corresponds to the change due to heating the sample by 15 K.

5.3 Temperature Dependence

Temperature-dependent measurements of the g factor [Fig. 5.4b] were performed on the same channel in order to compare the effects of temperature and electric field. The change in g factor due to an applied voltage of 2 V at 30 K is equivalent to the change due to the channel heating by 15 K. Since the channel is Ohmic, the power of heating is $P = V^2/R$, and according to Fourier's law of thermal conduction, $P = kA\frac{\Delta T}{\Delta x}$. Therefore the temperature gradient across the sample is

$$\Delta T = \frac{V^2}{R}\frac{\Delta x}{kA} \tag{5.2}$$

where V is the applied voltage, R is the resistance of the channel, $\Delta x = 500$ μm is the thickness of the sample, k is the thermal conductivity and $A = 5 \times 5$ mm^2 is the area of the sample.

The thermal conductivity of InGaAs changes as a function of temperature, indium concentration, dopant type, and dopant concentration, so we will use an estimate for the thermal conductivity based on measurements of similar materials. For Si doped n-GaAs with n = 1.4×10^{16}, the thermal conductivity is about 10 W/(cm K) [89]. At 30 K, the resistance of a channel patterned on $In_{0.03}Ga_{0.97}As$ with n = 3×10^{16} cm^{-3} was about 6 kΩ. Therefore, for 1 V applied across the channel, the temperature gradient between the top and bottom of the sample is 3×10^{-6} K. Therefore, the g factor dependence on voltage and temperature are likely distinct phenomena

5.3.1 Photoluminescence Measurements

To check whether the applied voltage was causing excessive channel heating, we performed temperature and voltage dependent photoluminescence (PL) measurements on a similar sample. For PL measurements, the sample was excited with a 633 nm HeNe laser. The

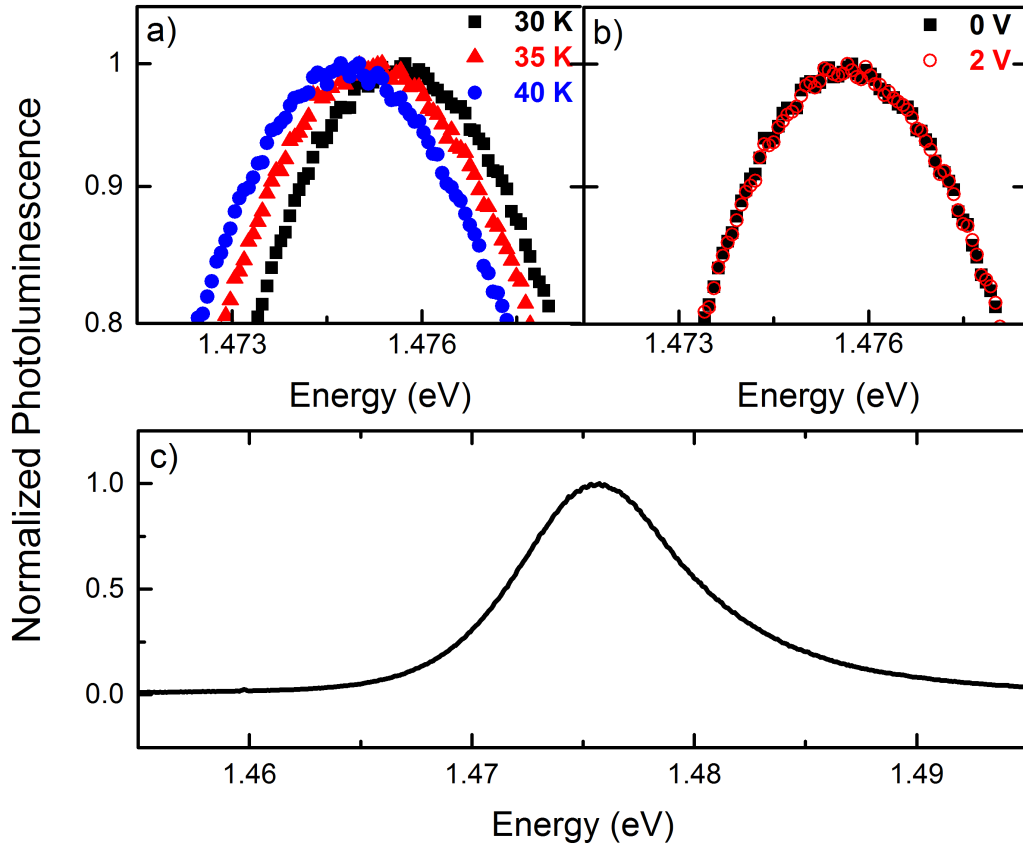

Figure 5.5: Photoluminescence as a function of temperature and voltage. (a) Photoluminescence of the $In_{0.03}Ga_{0.97}As$ epilayer, zoomed into the peak, at 30 K (black square), 35 K (red triangle), and 40 K (blue circle). There is a clear shift due to changes in the band gap with lattice temperature. (b) Photoluminescence for 0 V (black square) and 2 V (red circle) applied across the channel. There is no discernable shift. (c) Full normalized photoluminescence of the epilayer.

spectrum was analyzed using a spectrometer with a silicon CCD.

Figure 5.5 shows the PL from the sample while changing the temperature (a) and the voltage (b). The figure is zoomed into the peak in order to more clearly see the shift with temperature. From 30 K to 40 K, there was a clear shift in the energy of the peak due to the change in the band gap with lattice temperature. However, the PL for 0 V and 2 V had no discernible shift. Therefore, it is unlikely that the applied voltage is causing sufficient channel heating to account for the change in the g factor.

We expect the electron temperature to be significantly above the lattice temperature for

our range of applied electric fields, and one possible explanation for the change in g factor is that the g factor is dependent on the electron temperature. It was reported that in n-GaAs the electron temperature increased from 4.2 K at 0 V/cm to 38 K at 20 V/cm and 75 K at 50 V/cm [90]. The electron temperature was estimated from the high energy tail of the PL. We saw no change in the PL of our sample as a function of electric field. However, we expect the PL of our sample to have greater broadening due to it being an alloy [91]. The broadening due to alloy fluctuations could be overwhelming any changes due to the electric field.

The electron temperature can be estimated if the energy loss rate per electron is known, based on measurements performed on AlGaAs/GaAs heterostructures using PL [92], Shubnikov-de Haas oscillations [93], and far-infrared spectroscopy [94]. For an applied voltage of 2 V, we found the energy loss rate per electron in our samples to be 2×10^{-12} W, which corresponds to an electron temperature of about 50 K for a lattice temperature of 4.2 K.

Another possible explanation is that the applied electric field is modifying the wave function of donor-bound electrons, thus changing the g factor [95]. Calculations for a Si dopant in GaAs show that the relative magnitude change in the g factor is comparable to what we measure here. However, the sign of the change is opposite. Furthermore, for the doping density of the sample and at the temperatures considered here, contributions from donor-bound electrons are expected to be minimal. Therefore, we can rule out modification of donor-bound electron wave functions as the cause of the g factor modification.

The orbital contribution of spin-orbit induced circulating currents was shown to be significant in calculations of the g factor in quantum dots [96]. Similarly, the net drift velocity of the spins in our sample could be modifying the orbital contribution to the g factor.

5.4 Conclusion

We have performed electric-field dependent measurements of the g factor in a bulk Si-doped $In_{0.024}Ga_{0.976}As$ epilayer in a manner that distinguishes between changes in the g factor from changes in the spin-orbit field. Separate determination of these two quantities is important as their percent change with voltage is comparable. For example, for measurements along the [110] direction (Fig. 5.3), we found the g factor to be -0.4565 $\pm$ 0.0001 and the SO field to be 3.53 $\pm$ 0.01 mT for the largest drift velocity. If instead time-resolved measurements had been done to determine the SO field from the Larmor precession frequency with an applied magnetic field of 0.2 T assuming the zero field value of the g factor, the SO field would have been calculated to be only 0.965 $\pm$ 0.054 mT. However, more work is needed to develop a quantitative model for this phenomenon.

Chapter 6

Current-Induced Spin Polarization as a Function of Indium and Doping Concentrations

6.1 Motivation

Current-induced spin polarization (CISP) is a phenomenon in which a bulk electron spin polarization is generated by an electric field applied in the plane of the sample. It has been measured in semiconductor epilayers [8,63] and in two-dimensional electron gases [66,67], and is of interest for the development of an all-electrical, all-semiconductor spintronic device [58]. Indeed, all-electrical spin generation and spin manipulation has been demonstrated in n-InGaAs [34].

However, the polarization mechanism is still unclear. Although it was predicted that the spin polarization should be proportional to the spin-orbit (SO) splitting [9], measurements performed on InGaAs epilayers showed that the crystal axis with the smallest SO splitting had the largest CISP and vice versa [8]. In addition, CISP has been measured in GaN [68]

and ZnSe [69], which have weak SO coupling.

There are broadly two categories of spin polarization mechanisms [9]: intrinsic mechanisms, in which the spins are oriented by an effective magnetic field [97], and extrinsic mechanisms, in which spin dependent scattering results in a spin accumulation [98, 99].

In this chapter, we will report on measurements of CISP and SO fields in InGaAs epilayers with varying indium concentrations and doping densities in an effort to develop a phenomenological understanding of the factors that affect CISP. We also performed measurements of CISP on GaAs epilayers, in which the SO fields are smaller than what we can measure (<0.1 mT) and thus an intrinsic polarization mechanism seems unlikely. These results suggest that one muse consider extrinsic mechanisms in order to explain CISP. To understand the relative strength between intrinsic and extrinsic spin relaxation mechanisms in these samples, we performed measurements of the spin dephasing times as a function of temperature.

6.2 Sample Structure and Experimental Methods

Five InGaAs and two GaAs samples were studied, each consisting of a 500 nm epilayer grown by molecular beam epitaxy on a (001) GaAs substrate. All samples were Si-doped at different concentrations. The samples are etched into a cross-shaped channel with arms along the [110] and [$1\bar{1}0$] crystal axes. This allows for the application of an electric field along an arbitrary in-plane crystal axis [8].

Table 6.1 shows a summary of sample parameters. The indium concentrations are determined from x-ray rocking curves (XRC), which also show the epilayers to be pseudomorphic or nearly pseudomorphic with the substrate, i.e. the strain relaxation is minimal. The carrier concentrations are determined from Hall and van der Pauw measurements performed on the cross-shaped channels, and the mobilities are determined from spin drag measurements. All

Sample Name	x_{In} (%)	n (10^{16} cm^{-3})	μ (cm^2/Vs)
RMBE1129	0.026	20.8 ± 0.1	3200 ± 200
RMBE1130	0.026	15.5 ± 0.6	3400 ± 300
RMBE1132	0.024	1.58 ± 0.03	6500 ± 200
RMBE1302	0.020	2.93 ± 0.04	5100 ± 300
RMBE1301	0.020	0.270 ± 0.002	6600 ± 500
034XT	0.0	51.2 ± 0.2	2600 ± 200
033XT	0.0	3.00 ± 0.03	4600 ± 100

Table 6.1: Material parameters for the InGaAs and GaAs samples. Carrier concentration and mobility measured at 30 K.

values are measured at 30 K.

Spin-orbit coupling in semiconductors manifests as an effective internal magnetic field. In zinc-blende semiconductors, to first order in k, this is described by the Hamiltonian [86]

$$H_{\text{SO}} = \frac{1}{2}\frac{\hbar}{m^*}\left[\alpha(k_y\sigma_x - k_x\sigma_y) + \beta(k_x\sigma_x + k_y\sigma_y)\right] \tag{6.1}$$

for x $\|[1\bar{1}0]$ and y $\|[110]$, where α includes Rashba-like contributions from structural inversion asymmetry and uniaxial strain, and β includes linear Dresselhaus-like contributions from bulk inversion asymmetry and biaxial strain [36]. As these two components of the SO field have different crystal axis dependences, the anisotropy of the SO field is characterized by the parameter $r = \alpha/\beta$. In our InGaAs samples, the maximum SO field is along [110] and minimum along $[1\bar{1}0]$ crystal axes.

The SO fields are measured by performing pump-probe spin drag measurements on the samples [33]. Details of this measurement are discussed in Chapter 4. The InGaAs (GaAs) samples are measured in a transmission (reflection) geometry. Transmission measurements are not possible in the GaAs samples as the wavelength used to probe the epilayer is absorbed by the substrate.

When an electric field is applied across the sample, the electron spins precess about the

vector sum of the external and SO fields. The Faraday/Kerr rotation $\theta_{F,K}$ can be described by the equation

$$\theta_{F,K}(\mathbf{B}_{ext}, x) = \sum_n A_n(x) \cos\left[\frac{g\mu_B}{\hbar} |\mathbf{B}_{\text{ext}} + \mathbf{B}_{\text{int}}| (\Delta t + nt_{\text{rep}})\right] \tag{6.2}$$

where $A_n(x)$ is the amplitude due to successive pump pulses, g is the electron g-factor, μ_B is the Bohr magneton, $\mathbf{B}_{\text{ext}}$ is the external magnetic field, $\mathbf{B}_{\text{int}}$ is the internal SO field, Δt is the time delay between the pump and probe pulses, and $t_{\text{rep}} = 13.16$ ns is the time between laser pulses.

Spin drag measurements are performed with the electric field applied parallel to the external magnetic field along either the [110] or [$1\bar{1}0$] crystal axes and the time delay fixed to $\Delta t = 13$ ns. Measurements of the Faraday (Kerr) rotation as a function of magnetic field and pump-probe separation are fit to Eq. 6.2 in order to extract the spatial profile of the spin packet and the SO field. A summary of the measurement and fitting procedures for finding the drift velocity and SO field is given in Section 4.6.

The SO field is found to be linear with drift velocity, where the slope κ is used to characterize the strength of the SO field. Measurements of κ for voltages along the [110] and [$1\bar{1}0$] crystal axes allow us to extract the SO parameters α and β (Table 6.2). Also shown in Table 6.2 is the spin dephasing time T_2^*, which is determined from time-resolved Faraday rotation (TRFR) measurements.

CISP is measured with the Faraday rotation of the probe beam in the absence of optical pumping. This is described by the equation [63]

$$\theta_F = \theta_{\text{el}} \frac{\omega_L \tau}{(\omega_L \tau)^2 + 1} \tag{6.3}$$

where θ_{el} is the amplitude of the electrically induced Faraday rotation, ω_L is the Larmor precession frequency, and τ is the transverse spin lifetime.

	In conc. (%)	n (10^{16} cm^{-3})	α (ns neV/μm)	β (ns neV/μm)	r	T_2^* (ns)
InGaAs	2.6	20.8 ± 0.1	26 ± 5	27 ± 5	1.0 ± 0.3	5.1 ± 0.2
InGaAs	2.6	15.5 ± 0.6	39 ± 17	5.7 ± 17	6.9 ± 21	5.58 ± 0.07
InGaAs	2.4	1.58 ± 0.03	28 ± 13	2.9 ± 13	9.8 ± 43	7.67 ± 0.08
InGaAs	2.0	2.93 ± 0.04	-4.2 ± 16	28 ± 16	0.15 ± 0.6	17.9 ± 0.2
InGaAs	2.0	0.270 ± 0.002	13 ± 4	22 ± 4	0.61 ± 0.2	7.3 ± 0.1
GaAs	0.0	51.2 ± 0.2	-	-	-	6.8 ± 0.1
GaAs	0.0	3.00 ± 0.03	-	-	-	3.87 ± 0.06

Table 6.2: SO parameters and spin dephasing times for InGaAs and GaAs samples. Since the SO fields in the GaAs samples were very small, the SO parameters α, β, and r could not be determined.

In conc. (%)	n (10^{16} cm^{-3})	$\rho_{\rm el}/\theta_{\rm el}$ ([1$\bar{1}$0],[110]) (μm^{-3}/μrad)
2.6	20.8 ± 00.1	0.46, 0.73
2.6	1.55 ± 0.06	1.42, 1.40
2.4	1.58 ± 0.03	0.24, 0.27
2.0	2.93 ± 0.04	0.023, 0.022
2.0	0.270 ± 0.002	0.0043, 0.0043

Table 6.3: Conversion between electrically induced spin density and Faraday angle for the InGaAs samples, for measurements along the [110] and [1$\bar{1}$0] axes. As the absorption of the GaAs epilayers cannot be measured, the conversion between Faraday angle and spin density cannot be calculated.

It is possible to convert the electrically induced Faraday rotation $\theta_{\rm el}$ to a spin density by comparing the Faraday rotation due to optical polarization to the Faraday rotation due to electrical polarization [63]. In Section 4.7.1, we found that this relationship to be

$$\rho_{\rm el} = \frac{\theta_{\rm el}\rho_{\rm op}}{2\theta_{\rm op}} \tag{6.4}$$

where $\theta_{\rm el,op}$ is the Faraday rotation due to electrical and optical spin injection, and $\rho_{\rm op}$ is the density of optically polarized spins, assuming circularly polarized light results in a 50% spin polarization.

A summary of the CISP measurements and fitting procedures is given in Section 4.7.

The spin polarization generation rate $\gamma = \rho_{\rm el}/\tau$ is roughly linear in drift velocity ($\gamma = \eta v_{\rm d}$), and so the strength of the CISP is characterized by the slope η.

6.3 Current-Induced Spin Polarization vs Spin-Orbit Coupling

Measurements of κ, the SO field per unit drift velocity field, and η, the spin polarization rate per unit drift velocity, were performed for the [110] and [$1\bar{1}0$] crystal axes of the five InGaAs samples. The results are shown in Fig. 6.1, in which squares indicate the samples with higher (2.4-2.6%) indium concentration and triangles indicate samples with lower (2.0%) indium concentration. Carrier concentrations are indicated in the figure. For each sample, the ratio of Rashba-like to linear-Dresselhaus-like fields r is also shown.

In each InGaAs sample, we found that the [110] crystal axis had the largest SO field and the smallest magnitude of CISP, and the [$1\bar{1}0$] crystal axis had the smallest SO field and the largest magnitude of CISP. This is consistent with previous measurements performed by Norman *et al.* [8].

6.4 Current-Induced Spin Polarization vs Material Parameters

We are interested in how CISP is affected by the material, as this may give some insight into the polarization mechanism. Figure 6.2 shows η for the [$1\bar{1}0$] and [110] crystal axes as a function of the various sample parameters for the InGaAs samples. We found that samples with higher indium concentration had more CISP (Fig. 6.2a). Higher indium concentration causes more strain in the InGaAs epilayer due the lattice mismatch between InAs and the

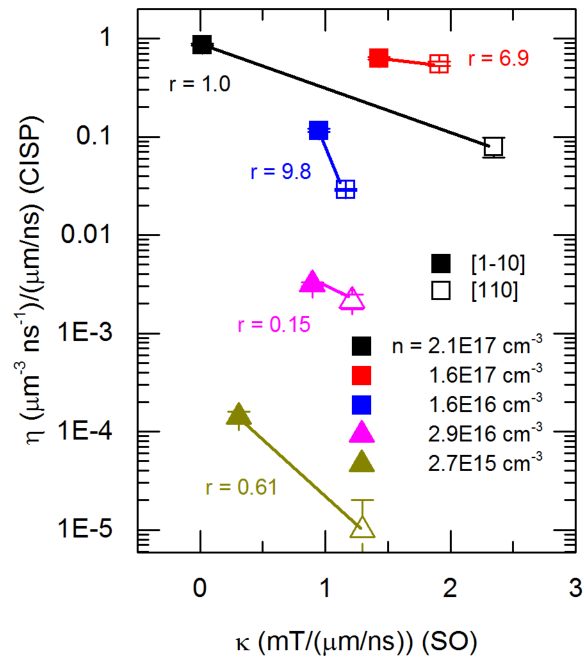

Figure 6.1: η (CISP) vs. κ (SO splitting) for all five InGaAs samples. Squares indicate samples with higher indium concentration (2.4%-2.6%) and triangles indicate samples with 2.0% indium. Filled in and open symbols are for measurements along the $[1\bar{1}0]$ and [110] crystal axes respectively. $r = \alpha/\beta$ characterizes the anisotropy of the SO field. There was a negative differential relationship observed between the two parameters in all five samples.

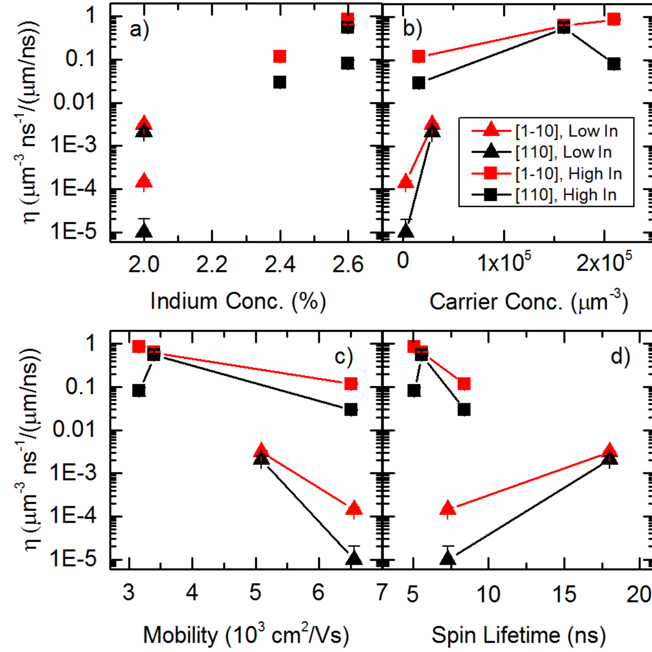

Figure 6.2: CISP vs material parameters. (a) η (CISP) for the $[1\bar{1}0]$ and [110] crystal axes as a function of (a) indium concentration, (b) carrier concentration, (c) mobility, and (d) spin lifetime. Black squares indicate samples with higher indium concentration (2.4%-2.6%) and red triangles indicate samples with 2.0% indium. Filled in and open symbols are for measurements along the $[1\bar{1}0]$ and [110] crystal axes respectively.

GaAs substrate. This in turn results in larger SO splitting in the epilayer. This suggests that the amount of SO splitting is related to the amount of CISP, albeit not in the direct way predicted by the Rashba-Edelstein equation [97].

Samples with higher carrier concentrations were found to have greater CISP (Fig. 6.2b). Assuming the same rate of spin polarization, this would result in a larger spin density given a larger carrier concentration. Furthermore, samples with lower mobility also had greater CISP (Fig. 6.2c). Since the mobility is proportional to the momentum scattering time, this indicates that samples with less time between scattering events had greater spin polarizations, and suggests that an extrinsic polarization mechanism dominates. There was no clear correlation between spin dephasing time and magnitude of CISP (Fig. 6.2d).

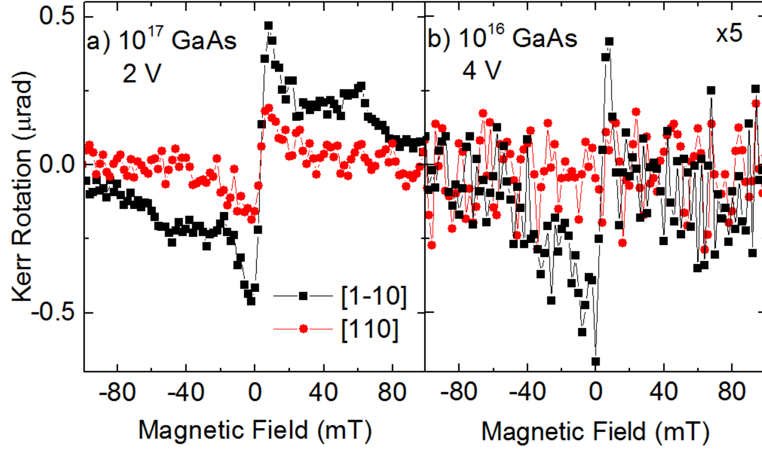

Figure 6.3: CISP in GaAs. CISP for (a) 2 V across the $n \sim 10^{17}$ cm^{-3} and (b) 4 V across the $n \sim 10^{16}$ cm^{-3} GaAs samples. The y-axis in (b) has been scaled by a factor of 5. Black squares and red circles indicate measurements along the $[1\bar{1}0]$ and [110] crystal axes respectively. There was no CISP detected in the $n = 10^{16}$ cm^{-3} GaAs sample along the [110] crystal axis. For both samples, CISP was greater along the $[1\bar{1}0]$ crystal axis. Furthermore, the sample with higher carrier concentration had greater CISP.

6.5 Current-Induced Spin Polarization in GaAs

In contrast to InGaAs grown on GaAs substrates, GaAs epilayers do not have strain induced spin-orbit fields. However, we also observed CISP in GaAs. Fig. 6.3a shows CISP for 2 V applied across the higher doped GaAs sample along both the $[1\bar{1}0]$ and the [110] crystal axes. Fig. 6.3b shows CISP for 4 V applied across the lower doped GaAs sample along the $[1\bar{1}0]$ and [110] crystal axes. There was no measurable CISP along the [110] axis in the lower doped GaAs sample. In the GaAs samples, the epilayer and substrate absorb at similar wavelengths, and so we cannot measure the absorption of only the epilayer in order to calculate the conversion factor A. Because of this, the CISP in the GaAs samples can only be reported in terms of μrad and the magnitude of CISP in these samples cannot be directly compared to the InGaAs samples.

As with the InGaAs samples, we found that the CISP was greater along the $[1\bar{1}0]$ axis than the [110] axis. Furthermore, we found that the GaAs sample with higher carrier concentration

had more CISP, consistent with the measurements in InGaAs.

The SO fields in the GaAs samples were very small (<0.1 mT) for both the [110] and $[1\bar{1}0]$ crystal axis. Since we were able to detect CISP despite the absence of measurable SO fields, this again suggests that the polarization mechanism is not consistent with the Rashba-Edelstein model.

6.6 Spin Dephasing Mechanisms

In this chapter, we found that the magnitude of the CISP decreases with increasing electron mobility, and that there is CISP in GaAs, which has immeasurably small SO fields. Norman *et al.* [8] found that the crystal axis with the largest magnitude of CISP did not correspond with the axis with the largest SO splitting, and that the orientation of the CISP was not necessarily parallel to the SO field. These results suggest that an extrinsic spin polarization mechanism dominates.

In order to further examine whether intrinsic or extrinsic mechanisms dominate in these samples, we can look at the spin dephasing. We expect to see two dephasing mechanisms in these materials: D'yakonov-Perel' (DP) dephasing [47], an intrinsic effect that is due to precession of the spins about momentum-dependent spin-orbit fields between scattering events, and Elliot-Yafet (EY) dephasing [50], an extrinsic effect that is due to spin flips at scattering events. The spin dephasing mechanisms that are relevant to us are discussed in more detail in Section 3.4.

The contributions to the total spin dephasing time from DP and EY contributions have different dependences on the mobility and temperature. The total spin dephasing time is given by [100]

$$\frac{1}{\tau_s} = \frac{1}{\tau_{\mathrm{EY}}} + \frac{1}{\tau_{\mathrm{DP}}} = C_{\mathrm{EY}}\mu^{-1}T^2 + C_{\mathrm{DP}}\mu T^3 \tag{6.5}$$

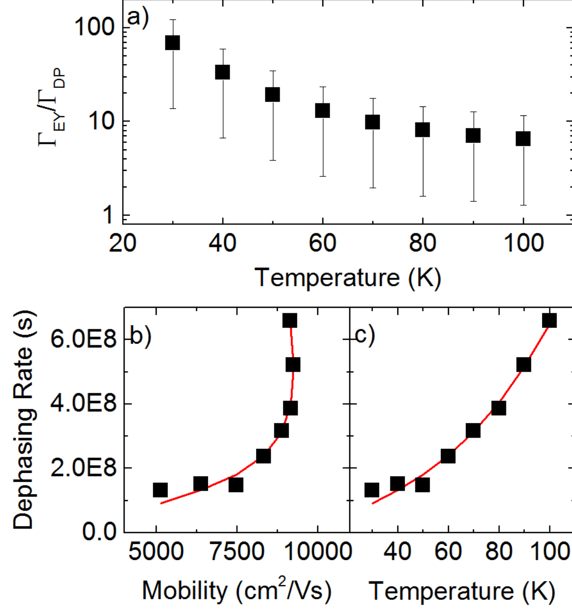

Figure 6.4: Temperature dependent fits of the spin dephasing rate. (a) Ratio of the dephasing rates due to the EY and DP dephasing mechanisms for the $In_{0.024}Ga_{0.976}As$ sample with $n = 1.58 \times 10^{16}$ cm^{-3}, calculated from results of a two-independent variable fit of the dephasing rate as a function of the temperature and the temperature-dependent mobility. $q > 1$ indicates that the extrinsic EY dephasing mechanism dominates at 30 K.

where T is the temperature, and C_{EY} and C_{DP} are coefficients denoting the relative strength of the EY and DP dephasing mechanisms.

We performed temperature dependent measurements of the spin dephasing time τ_s and mobility μ, in order to extract the relative strength of the EY and DP dephasing mechanisms.

We can fit for C_{EY} and C_{DP} in Eq. 6.5 using a two independent variable fit, with T and μ as the independent variables. The relative strength of the two dephasing mechanisms is then defined by

$$q(T) = \frac{\tau_{\mathrm{EY}}^{-1}}{\tau_{\mathrm{DP}}^{-1}} = \frac{C_{\mathrm{EY}}}{C_{\mathrm{DP}}}\mu^{-2}T^{-1} \tag{6.6}$$

The value of $q(T)$ calculated from the fits of the dephasing time and Eq. 6.6 is shown in Fig. 6.4a. The fits of the dephasing time versus mobility and temperature are shown in Fig.

6.4b,c for the sample with n = 1.6×10^{16} cm^{-3}.

At 30 K, the temperature at which all CISP and SO field measurements were performed, the extrinsic EY dephasing mechanism was found to be comparable to or dominant over the intrinsic DP dephasing mechanism for all samples.

6.7 Proposed Spin Polarization Mechanisms

There have been several proposed mechanisms that result in a bulk current-induced spin polarization. These mechanisms for CISP can be broadly separated into two categories [9]: intrinsic mechanisms, in which the spins are oriented by an effective magnetic field [97, 101], and extrinsic mechanisms, in which spin dependent scattering results in a spin accumulation [98, 99].

In the following, we will discuss three proposed polarization mechanisms, the predictions they make about the relationship between the spin-orbit fields and CISP, and how those predictions compare with measurements of CISP in InGaAs and GaAs epilayers.

6.7.1 Edelstein Effect

Edelstein originally proposed the spin polarization of electrons by an electric current while considering only a Rashba-like spin-orbit field [97]. Since Rashba-like fields are isotropic in the (001) plane, this would result in an isotropic spin polarization.

Edelstein's result was expanded by Trushin and Schliemann [102] to include both Rashba- and linear-Dresselhaus-like spin-orbit fields. Their result can be understood simply by starting from the Bloch equation.

Since we already discussed spin dephasing and spin-orbit fields in Ch. 3, we present an updated version of the Bloch equation. Ignoring extrinsic effects (i.e. effects due to

scattering, such as Elliot-Yafet dephasing), we have:

$$\frac{\partial S}{\partial t} = -\Gamma_{\mathrm{DP}} \left(\mathbf{S} - \mathbf{S}_{\mathrm{eq}}\right) + \mathbf{\Omega}_{\mathrm{tot}} \times \mathbf{S} \tag{6.7}$$

where $\mathbf{S}_{\mathrm{eq}}$ is the equilibrium spin polarization, given by $\mathbf{S}_{\mathrm{eq}} = \chi\hbar\mathbf{\Omega}_{\mathrm{tot}}$, where χ is the Pauli spin susceptibility [103], and $\mathbf{\Omega}_{\mathrm{tot}} = \mathbf{\Omega}_{\mathrm{ext}} + \mathbf{\Omega}_{\mathrm{SO}}$ is the Larmor frequency due to the total magnetic field.

The steady state solution to this equation is simply $\mathbf{S} = \mathbf{S}_{\mathrm{eq}}$. In the absence of an external magnetic field, this means that the equilibrium spin polarization aligns along the spin-orbit field, i.e.

$$\begin{aligned} \mathbf{S} &= \chi\hbar \begin{pmatrix} \alpha' k_y + \beta' k_x \\ -\alpha' k_x - \beta' k_y \end{pmatrix} \\ &= \chi\hbar \begin{pmatrix} \beta' & \alpha' \\ -\alpha' & -\beta' \end{pmatrix} \begin{pmatrix} k_x \\ k_y \end{pmatrix} \end{aligned} \tag{6.8}$$

which is the result arrived at by Trushin and Schliemann [102]. The spin polarization is therefore greatest along the crystal axis with the largest spin-orbit field and vice versa.

This result is contrary to the measurements by Norman *et al.* [8] and the measurements shown in this chapter, in which the crystal axis with the largest spin-orbit field has the smallest spin polarization. Furthermore, Norman *et al.* found that the spin polarization did not always align with the spin-orbit field, again in contradiction to what is predicted for the Edelstein effect. The presence of CISP in GaAs, despite the absence of measurable SO fields, also indicates that this theory is not a complete explanation for CISP.

6.7.2 Spin Polarization from a Spin Hall Current

It was proposed by Korenev [101] that the spin Hall current, which results in a transverse spin current and thus a spin accumulation along the edges of the channel, may also generate

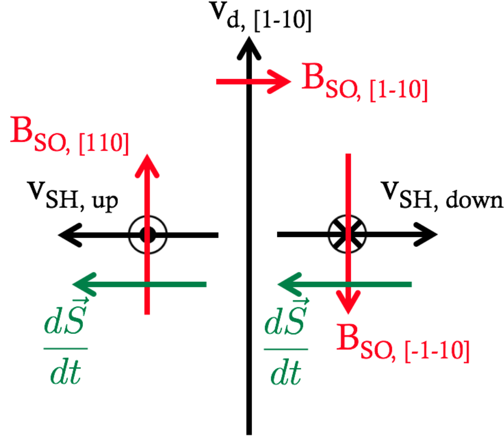

Figure 6.5: Spin polarization from a spin Hall current. A drift velocity along the $[1\bar{1}0]$ crystal axis results in a spin Hall current of spin up electrons moving towards the left and spin down electrons moving towards the right. The electrons in the spin Hall current precess about the corresponding SO field (red arrows), which is perpendicular to the spin Hall current. This results in the generation of a spin polarization (green arrows).

a bulk spin polarization.

The polarization mechanism is illustrated in Fig. 6.5. A voltage is applied along the $[1\bar{1}0]$ crystal axis, resulting in a drift velocity v_d along the $[1\bar{1}0]$ axis, as well as a spin Hall current perpendicular to the applied voltage. The spin Hall current is a result of the spin up electrons scattering to the left with net velocity $v_{\text{SH, up}}$ and spin down electrons scattering to the right with net velocity $v_{\text{SH, down}}$.

For the illustration, we have chosen a spin-orbit field in which the Rashba-like field dominates (i.e. $|r| > 1$) but with a non-zero linear-Dresselhaus-like field, such that the field is anisotropic. Both the spin up and spin down electrons in the spin Hall current will experience a spin-orbit field perpendicular to their motion. The rate of change of the spin polarization is given by $\mathbf{\Omega} \times \mathbf{S}$, so we have

$$\begin{aligned}\frac{d\mathbf{S}_{\mathrm{SH},\uparrow}}{dt} &= \mathbf{\Omega}_{\mathrm{SO},[110]} \times \mathbf{S}_{SH,\uparrow} \\ &\propto -\mathbf{B}_{\mathrm{SO},[110]} \times \mathbf{S}_{SH,\uparrow} \\ \frac{d\mathbf{S}_{\mathrm{SH},\downarrow}}{dt} &= \mathbf{\Omega}_{\mathrm{SO},[\overline{1}\overline{1}0]} \times \mathbf{S}_{SH,\downarrow} \\ &\propto -\mathbf{B}_{\mathrm{SO},[\overline{1}\overline{1}0]} \times \mathbf{S}_{SH,\downarrow}\end{aligned} \tag{6.9}$$

Here, we have used the fact that the g factor is negative in GaAs. Since $\mathbf{B}_{\mathrm{SO},[110]} = -\mathbf{B}_{\mathrm{SO},[\overline{1}\overline{1}0]}$ and $\mathbf{S}_{SH,\uparrow} = -\mathbf{S}_{SH,\downarrow}$, both the spin up and spin down components of the spin Hall current results in a net generation of a spin polarization along the same direction (green arrow in Fig. 6.5).

Korenev writes the spin-orbit interaction in terms of a second-rank pseudo-tensor $\hat{\mathbf{Q}}$, such that $\mathbf{B} = \frac{1}{g\mu_B}\hat{\mathbf{Q}}\mathbf{p}$. For the Rashba-like field, $\hat{\mathbf{Q}}_{SIA}$ is given by:

$$Q_{\alpha\beta} = \alpha' \epsilon_{\alpha\beta z} \tag{6.10}$$

where ϵ_{ijk} is the Levi-Civita symbol, and the linear-Dresselhaus-like field, $\hat{\mathbf{Q}}_{BIA}$ is given by

$$Q_{xx} = -Q_{yy} = \beta' \tag{6.11}$$

with all other terms zero.

The total spin generation rate given by Korenev is

$$\begin{aligned}\dot{\mathbf{S}}_g &= -Nm\mu_H\hat{\mathbf{Q}}^T\mathbf{E}/\hbar \\ &= \frac{N\mu_H}{\mu_d}(\mathbf{\Omega}_{\mathrm{BIA}} - \mathbf{\Omega}_{\mathrm{SIA}})\end{aligned} \tag{6.12}$$

where N is the electron concentration, m is the electron mass, μ_H and μ_d is the Hall and drift mobility, and $\mathbf{E}$ is the applied electric field.

If we define the angle ϕ as the direction of the electric field relative to the [100] crystal

axis, then the spin generation rate can be written as

$$
\begin{aligned}
\dot{\mathbf{S}}_g &= \frac{N\mu_H}{\mu_d}(\mathbf{\Omega}_{\text{BIA}} - \mathbf{\Omega}_{\text{SIA}}) \\
&= \frac{N\mu_H}{\mu_d}((\beta' k_x - \alpha' k_y)\hat{\mathbf{x}}) - (\beta' k_y - \alpha' k_x)\hat{\mathbf{y}}) \\
&= \frac{N\mu_H}{\mu_d}\beta' k((\cos\phi - r\sin\phi)\hat{\mathbf{x}} - (\sin\phi - r\cos\phi)\hat{\mathbf{y}})
\end{aligned}
\tag{6.13}
$$

Similarly, the spin-orbit field can be written as

$$
\begin{aligned}
\mathbf{B}_{\text{SO}} &= \frac{\hbar}{\mu_B g}(\mathbf{\Omega}_{\text{BIA}} + \mathbf{\Omega}_{\text{SIA}}) \\
&= \frac{\hbar}{\mu_B g}\beta' k((\cos\phi + r\sin\phi)\hat{\mathbf{x}} - (\sin\phi + r\cos\phi)\hat{\mathbf{y}})
\end{aligned}
\tag{6.14}
$$

The strengths of the electrically generated spin polarization and the spin-orbit field are quantified by the parameters

$$
\begin{aligned}
\eta &= \left|\frac{\dot{\mathbf{S}}_g}{v_d}\right| = \frac{m^* N\mu_H}{\hbar\mu_d}\beta'\sqrt{1 + r^2 - 2r\sin 2\phi} \\
\kappa &= \left|\frac{\mathbf{B}_{\text{SO}}}{v_d}\right| = \frac{m^*}{\mu_B g}\beta'\sqrt{1 + r^2 + 2r\sin 2\phi}
\end{aligned}
\tag{6.15}
$$

where $v_d = \frac{\hbar}{m^*}k$ is the drift velocity.

Figure 6.6(a) shows the data taken by Norman et al. [8] for the relationship between CISP and the spin-orbit splitting for two pieces of $In_{0.04}Ga_{0.96}As$ taken from the same wafer. Inhomogeneous strain relaxation resulted in a different value of r for the two pieces. Figure 6.6(b) shows the predicted relationship between CISP and the spin-orbit splitting for spin polarization by a spin Hall current. Although this theory predicts that the crystal axes with the smaller spin-orbit splitting have the largest CISP, in agreement with the measurement, the exact shape of the curve does not match the data, i.e. the concavity is different. Furthermore, for the two different values of r, the theory predicts the relationship between CISP and

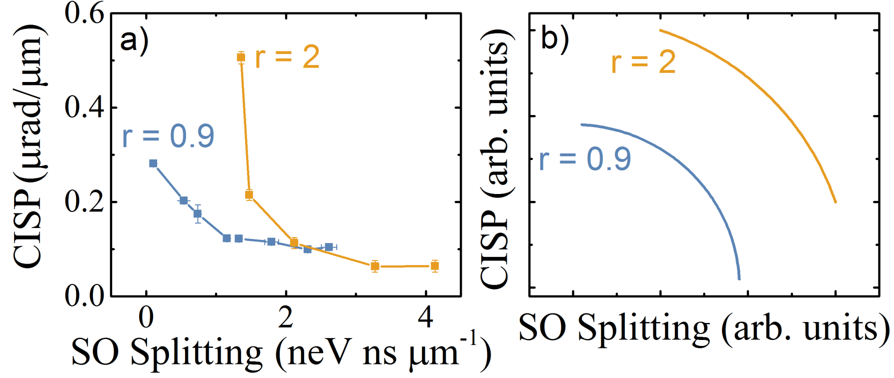

Figure 6.6: Comparison of spin polarization from a spin Hall current to data. (a) CISP vs spin-orbit splitting for two $In_{0.04}Ga_{0.96}As$ samples from the same wafer. Each point corresponds to measurements along a different crystal axis. Due to inhomogeneous strain relaxation, the value of r is different for the two pieces. Data taken by B. M. Norman [8]. (b) Predicted relationship between CISP and the spin-orbit splitting for a spin polarization from a spin Hall current. Although there is also a negative differential relationship between these two quantities, the exact shapes of the curve do not match the experimental results.

the spin-orbit coupling should lie on the same curve, whereas the data shows that the two curves intersect. The only way for the theory to predict intersecting curves is if the effective mass, carrier concentration, or mobility is significantly different between the two samples. However, the data shown in Fig. 6.6 are taken from two pieces from the same wafer, and so all material parameters are expected to be the same except the strain relaxation, and therefore r.

Norman *et al.* also found that the CISP did not necessarily align along the same direction as the spin-orbit field. They explained this misalignment using a phenomenological model based on anisotropic dephasing rates. They derived the angle ζ between the steady-state spin polarization and the SO field to be

$$\zeta = \tan^{-1}\left[\frac{2r(\cos^2\phi - \sin^2\phi)}{1-r^2}\right] \tag{6.16}$$

Now let us calculate the same angle for the bulk spin polarization generated by a spin Hall current. The steady state spin polarization is $\mathbf{S} = \dot{\mathbf{S}}_g\tau_s$ [101], where τ_s is the spin

dephasing time, so ζ is defined by

$$\begin{aligned}\cos\zeta &= \frac{\mathbf{S}\cdot\mathbf{B}_{\mathrm{SO}}}{|\mathbf{S}|\,|\mathbf{B}_{\mathrm{SO}}|} \\ &= \frac{1-r^2}{\left((1+r^2)^2-4r^2\sin^2 2\phi\right)^{1/2}}\end{aligned} \tag{6.17}$$

Using the relation $\tan(\cos^{-1}x) = \frac{\sqrt{1-x^2}}{x}$, we arrive at the same result as Norman *et al.* (Eq. 6.16).

Therefore, the theory of a bulk spin polarization generated by a spin Hall current matches several of the features measured by Norman *et al.*, namely that the crystal axis with the largest CISP has the smallest spin-orbit field and vice versa, and that the CISP is misaligned from the spin-orbit field by an angle ζ, described by equation 6.16.

However, the shape of the curve for the relationship between the CISP and spin-orbit field does not match the shape measured by Norman *et al.* (i.e. the concavity is different). Furthermore, if the Rashba-like field dominates, the spin orbit field corresponding to the direction of the applied current ($\mathrm{B}_{\mathrm{SO},\,[1\bar{1}0]}$ in Fig. 6.5) *anti*-aligns with the spin generation $\frac{d\mathbf{S}}{dt}$. The relative orientation of the CISP and the spin-orbit field can be determined using measurements of the nuclear spin polarization.

Coupling between the current-induced electron spin polarization and the lattice nuclei has been shown to result in dynamic nuclear polarization (DNP) [85]. The nuclear polarization gives rise to a magnetic field B_N, and so the electron spins will precess about the total magnetic field $B_{\mathrm{total}} = B_{\mathrm{ext}} + B_{\mathrm{SO}} + B_{\mathrm{N}}$ (Fig. 6.7(a)). However, the nuclear field has a much longer saturation time ($\sim$100 s) than the spin-orbit field, and so if we were to measure the precession frequency as a function of lab time, the precession frequency would change abruptly when a voltage is turned on due to the spin-orbit effects, and then experience a slower change due to the nuclear field.

Details of this measurement are discussed in [85]. The results are shown in Fig. 6.7(b).

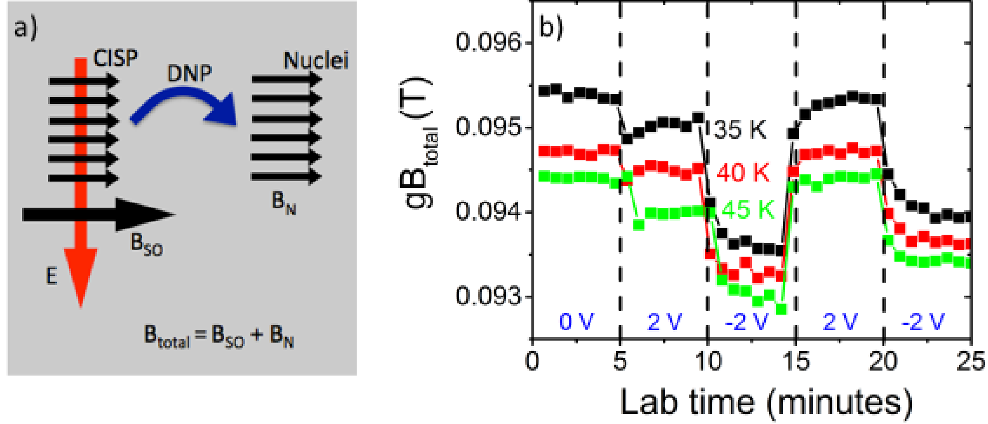

Figure 6.7: Dynamic nuclear polarization measurements. (a) An electric field is applied across a sample, resulting in a spin-orbit field and current-induced electron spin polarization. The electron spin polarization results in dynamic nuclear polarization, which gives rise to a magnetic field B_{N}. The electron spins will precess about the total magnetic field. (b) Measurements of the precession frequency $\Omega_L \propto gB_{\mathrm{total}}$ as a function of lab time. The times at which the applied voltage is changed are shown with dashed lines. The change in voltage results in a sudden change in the precession frequency due to changes in the spin-orbit field, followed by a slow change due to saturation of the nuclear field. From this data, we can see that the spin-orbit field is aligned along the nuclear field, and therefore the current-induced electron spin polarization.

The saturation due to the nuclear field is in the same direction as the jump in precession frequency due to the spin-orbit field, so we can conclude that the current-induced electron spin polarization is aligned, not anti-aligned, with the spin-orbit field. This is further evidence that the electron spin polarization in our samples is not produced by the mechanism proposed by Korenev.

6.7.3 Current-Induced Spin Polarization from Extrinsic Contributions

Gorini *et al.* derived the Bloch equation including both intrinsic and extrinsic contributions to the spin dephasing, the spin Hall effect, and the Rashba-Edelstein effect [103]. The change in the total spin polarization over time is given as:

$$\frac{\partial \mathbf{S}}{\partial t} = -(\Gamma_{\mathrm{DP}}+\Gamma_{\mathrm{EY}})\left(\mathbf{S}-\frac{N_0}{2}\mathbf{B}_{\mathrm{ext}}\right)-(\mathbf{B}_{\mathrm{ext}}+\mathbf{B}_{\mathrm{SO}})\times\mathbf{S}+(\Gamma_{\mathrm{DP}}-\Gamma_{\mathrm{EY}})\frac{N_0}{2}\mathbf{B}_{\mathrm{SO}}+\frac{\theta_{\mathrm{SH}}^{\mathrm{ext}}}{\theta_{\mathrm{SH}}^{\mathrm{int}}}\Gamma_{\mathrm{DP}}\frac{N_0}{2}\mathbf{B}_{\mathrm{SO}} \tag{6.18}$$

where N_0 is the density of states, and $\theta_{\mathrm{SH}}^{\mathrm{int(ext)}}$ is the spin Hall angle due to intrinsic (extrinsic) contributions. The first term is due to spin dephasing, with contributions from DP and EY mechanisms. The second term is due to spin precession, the third term is a spin generation term, and the fourth term is for spin Hall contributions.

In the absence of the EY dephasing mechanism and spin Hall effect, this equation reduces to the Rashba-Edelstein equation (Section 6.7.1).

One should also note that the DP and EY dephasing rates are added together in the first term, but subtracted in the third term. This can be explained as follows. The SO coupling results in spin-splitting of the conduction band. This means that, at the Fermi level, the electrons in the lower-energy spin-split band have higher momentum than the electrons in the higher-energy band. The EY mechanism results in faster dephasing of spins with higher momentum, and so the EY mechanisms decreases the spin polarization caused by the SO field. For this reason, there is a minus sign in front of the EY dephasing rate in the third term of Eq. 6.18.

It is important to keep in mind that this equation was derived for a 2-dimensional electron gas (2DEG). In order to compare the predictions of this theory to our measurements in bulk materials, a more complete treatment would require a re-derivation of these equation in order to take into account all 3-dimensional effects. This will change the form of the EY dephasing tensor; however, this will mainly affect the crystal axes besides the [110] and [$1\bar{1}0$] crystal axes. Therefore, we will only do calculations of the predicted steady-state spin density for electric fields along the [110] and [$1\bar{1}0$] crystal axes, as we expect the results to be similar for the 2D and 3D cases. In addition, we will substitute N_0 with the 3-dimensional density

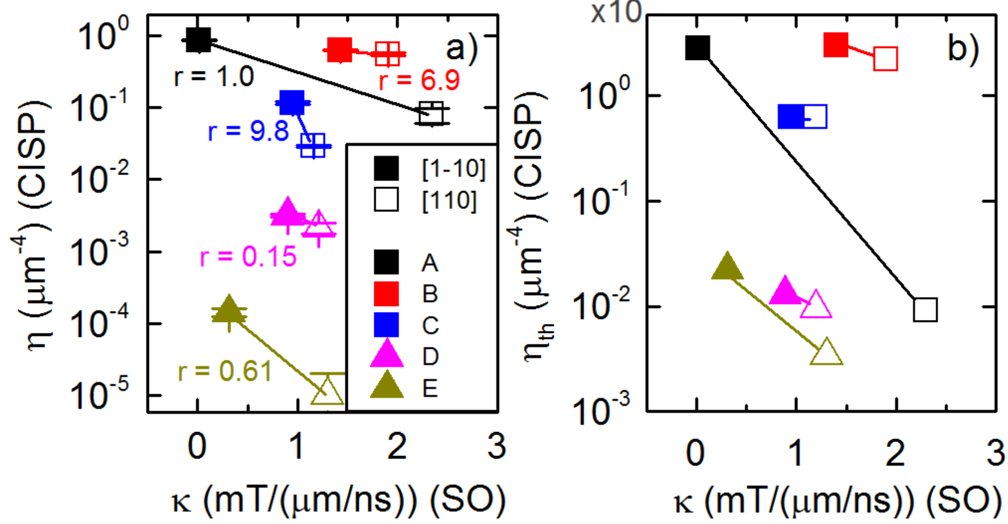

Figure 6.8: Comparison of CISP theory and experiment. Left: Experimental values for η vs. κ. Right: Theoretical predictions for η (CISP) vs. κ (SO splitting) based on the material parameters of four InGaAs samples.

of states. This will allow for at least preliminary comparison of the theory with experiment.

Equation 6.18 can be solved in the steady-state (i.e. $\frac{\partial \mathbf{S}}{\partial t} = 0$). We can then compare the dependence of the steady-state spin polarization on the spin-orbit field with the measurements, as well as compare the calculated magnitude of the steady-state spin polarization with the measured values.

Figure 6.8 (right) shows the calculated spin generation rate per unit drift velocity η versus the spin-orbit splitting κ. The two points correspond to the [110] and the [1$\bar{1}$0] crystal axes. The values of η were calculated using the material parameters of four of the InGaAs samples (sample names shown in the figure), namely the strength of the SO fields α and β, the ratio of the dephasing rates q, the carrier concentration n, and the mobility μ. Since our experimental setup does not have the spatial resolution to measure the spin Hall effect, we used the value for the spin Hall conductivity measured by Kato *et al.* in $In_{0.07}Ga_{0.93}As$ epilayers [33], which was 0.5 Ω^{-1}m^{-1}. This value is consistent with the calculation by Engel *et al.* for GaAs epilayers [104], and so we expect it to be valid for our samples despite their lower indium concentration. We corrected for differences in the carrier concentration, since the spin Hall

Sample Name	q	θ_{SH}^{ext}	θ_{SH}^{int}
RMBE1129	10	4.7×10^{-4}	1.4×10^{-8}
RMBE1130	0.1	5.9×10^{-4}	7.8×10^{-7}
RMBE1132	70	3.0×10^{-5}	7.9×10^{-7}
RMBE1302	20	2.7×10^{-4}	4.7×10^{-7}
RMBE1301	10	1.7×10^{-5}	3.0×10^{-7}

Table 6.4: Material parameters for the InGaAs samples used to calculate the predicted electrical spin generation efficiency.

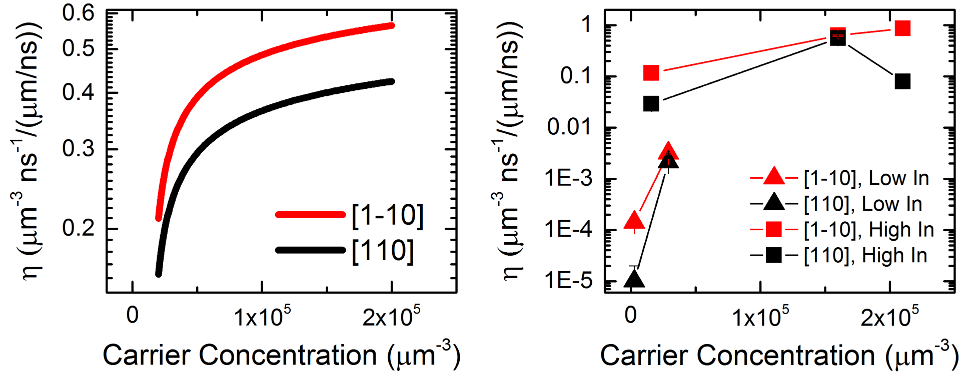

Figure 6.9: Spin generation rate vs. carrier concentration. Left: Theoretical predictions for η (CISP) vs. carrier concentration based on the material parameters of RMBE1302. Right: Experimental values for η vs. carrier concentration. Each point corresponds to a different sample.

conductivity is proportional to the carrier concentration [104]. The intrinsic spin Hall angle is given by $\theta_{SH}^{int} = m\tau(\beta^2 - \alpha^2)$. The specific parameters used for the calculations are given in Table 6.4.

One can see that, for the given material parameters, the theory predicts a negative differential relationship between the CISP and the SO splitting, consistent with our measurements. Furthermore, the theoretical results qualitatively match several features of the experimental data (Fig. 6.8 (left)), including the relative magnitude of the spin densities for orthogonal crystal axes of the same sample, and the relative magnitude of the spin densities of different samples.

The theory does predict spin densities an order of magnitude larger than those measured. This may be due to experimental limitations in determining material parameters, such as

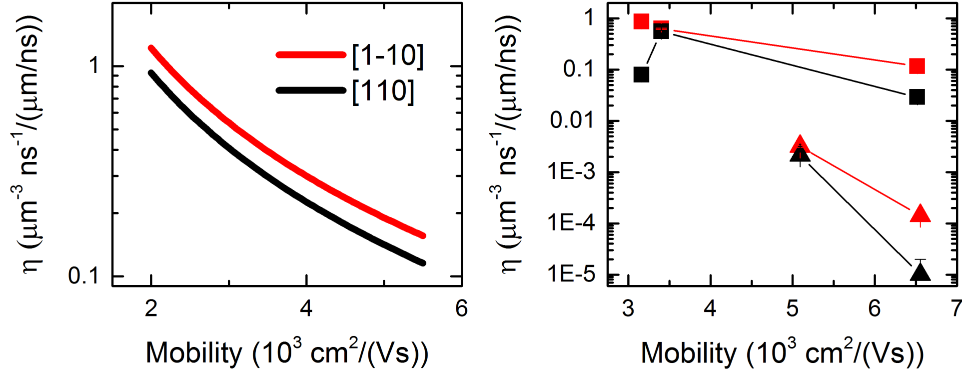

Figure 6.10: Spin generation rate vs. mobility. Left: Theoretical predictions for η (CISP) vs. mobility based on the material parameters of RMBE1302. Right: Experimental values for η vs. mobility. Each point corresponds to a different sample.

the extrinsic spin Hall angles. It may also be due to the fact that the theory is for a 2DEG, while the experiment was performed on 3D materials.

We can also examine the predicted dependence of the spin density on different material parameters, such as the carrier concentration n, the mobility μ, ratio of spin dephasing rates q, and the ratio of spin-orbit fields r. In order to do this, we will take the material parameters from one sample (RMBE1302) and vary them one at a time.

The results for the spin generation rate per unit drift velocity η as a function of carrier concentration are shown in Fig. 6.9 (left). The spin generation rate increases with carrier concentration, consistent with experiment (Fig. 6.9 (right)). It should be noted that each point in Fig. 6.9, right, corresponds to a different sample, and so other material parameters in addition to the carrier concentration are different for each sample. However, the general trend is consistent with the theoretical calculation.

We have also calculated the spin generation rate per unit drift velocity η as a function of mobility (Fig. 6.10 (left)). The spin generation rate is highest in samples with the lowest mobility, consistent with the experimental results (Fig. 6.10 (right)). Again, each point in the experimental results corresponds to a different sample, and so the two plots cannot be directly compared. However, the theoretical and experimental results are qualitatively

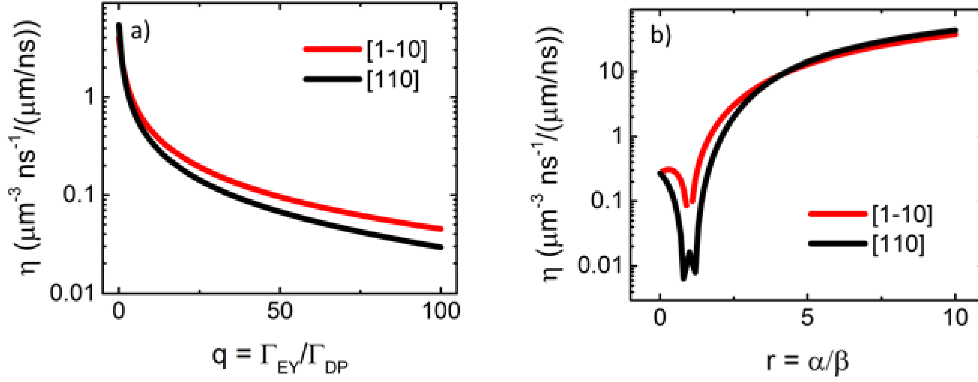

Figure 6.11: Spin generation rate vs. q and r. Theoretical predictions for η (CISP) vs. (a) q and (b) r based on the material parameters of RMBE1302.

similar.

We can also look at the theoretical dependence of the spin generation rate on the ratio of the spin dephasing times q and the ratio of the spin-orbit fields r. The spin generation rate is largest when q is smallest (Fig. 6.11(a)), i.e. when the DP dephasing mechanism dominates.

Figure 6.11(b) shows the spin generation rate as a function of the ratio of the Rashba-like to Dresselhaus-like spin-orbit fields r. Although the spin generation rate is lowest at $r = 1$, the anisotropy between the [$1\bar{1}0$] and [110] is greatest for that value of r. Experimentally, the value of r can be tuned within a single sample, providing a way of directly comparing this theory to experimental results. For example, mechanical strain can be used to tune the spin-orbit field while the carrier concentration and indium concentration remain the same [105].

6.8 Conclusion and Future Work

We performed measurements of CISP and SO splitting along the [110] and [$1\bar{1}0$] crystal axes in seven $In_xGa_{1-x}As$ samples with different Indium concentrations and doping densities. In

all samples, we found a negative differential relationship between the magnitude of the CISP and SO splitting. Since this is contrary to what is predicted by the Rashba-Edelstein equation, which includes only intrinsic SO contributions, we conclude that extrinsic polarization mechanisms are also necessary to include to explain the trends that are observed in the experiment. This is corroborated by temperature dependent spin dephasing time measurements, which show that the contribution from the extrinsic EY dephasing mechanism is comparable to or greater than the contribution from the intrinsic DP dephasing mechanism. It is also consistent with measurements performed on GaAs, where we measured CISP despite the samples having SO fields smaller than our measurement resolution of <0.1 mT.

We discussed three proposed polarization mechanisms. The first two are the Edelstein effect, in which spins align along the SO field, and a mechanism in which precession of spins in the transverse spin Hall current results in a spin polarization. Neither of these mechanisms fully explain the experimental results, so we then consider a spin dynamics equation that includes extrinsic contributions to spin dephasing and the spin Hall effect. This last model gives results that are qualitatively similar to our experimental results. However, more work must be done in order to make a direct comparison.

The spin dynamics equation that includes extrinsic contributions was derived for a 2DEG, whereas the samples under study in this thesis are bulk epilayers. Further theoretical work must be done in order to take into account all the effects of a 3D system.

In the theoretical calculations presented here, we assumed a value for the spin Hall angle based on reported values for GaAs since our experimental setup does not have the spatial resolution to measure the spin Hall effect directly. In the future, an optical pump-probe setup with a microscope objective can be used to reduce the spot size of the laser on the sample, allowing for the spatial resolution of the spin Hall effect. This will allow us to quantify the interplay between the effects due to spin-orbit fields, spin dephasing, and the spin Hall effect, since the current-induced spin polarization is likely dependent on all these

phenomena.

The theory also makes predictions about the dependence of the spin generation rate as a function of the spin-orbit parameter r. We can tune the spin-orbit field of a sample by applying mechanical strain, which will provide a more direction comparison between theory and experiment. In general, tuning the spin-orbit field will allow for a more systematic study of the effects of the spin-orbit fields on the current-induced spin polarization independent of the indium concentration, carrier concentration, and mobility.

Bibliography

[1] G. E. Uhlenbeck and S. Goudsmit, "Spinning electrons and the structure of spectra," *Nature*, vol. 117, p. 264, 1926.

[2] M. N. Baibich, J. M. Broto, A. Fert, F. N. V. Dau, F. Petroff, P. Etienne, G. Creuzet, A. Friederich, and J. Chazelas, "Giant magnetoresistance of (001)Fe/(001)Cr magnetic supperlattices," *Phys. Rev. Lett.*, vol. 61, p. 2472, 1988.

[3] G. Binasch, P. Grünberg, F. Saurenbach, and W. Zinn, "Enhanced magnetoresistance in layered magnetic structures with antiferromagnetic interlayer exchange," *Phys. Rev. B*, vol. 39, p. 4828, 1989.

[4] S. Datta and B. Das, "Electronic analog of the electro-optical modulator," *Appl. Phys. Lett.*, vol. 56, p. 665, 1990.

[5] P. Chuang, S.-C. Ho, L. W. Smith, F. Sfigakis, M. Pepper, C.-H. Chen, J.-C. Fan, J. P. Griffiths, I. Farrer, H. E. Beere, G. A. C. Jones, D. A. Ritchie, and T.-M. Chen, "All-electric all-semiconductor spin field-effect transistors," *Nature Nanotechnology*, vol. 10, p. 35, 2014.

[6] K. Ando, S. Fujita, J. Ito, S. Yuasa, Y. Suzuki, Y. Nakatani, T. Miyazaki, and H. Yoda, "Spin-transfer torque magnetoresistive random-access memory technologies for normally off computing," *J. Appl. Phys.*, vol. 115, p. 172607, 2014.

[7] J. Åkerman, "Toward a universal memory," *Science*, vol. 308, p. 508, 2005.

[8] B. M. Norman, C. J. Trowbridge, D. D. Awschalom, and V. Sih, "Current-induced spin polarization in anisotropic spin-orbit fields," *Phys. Rev. Lett.*, vol. 112, p. 056601, 2014.

[9] A. G. Aranov, Y. B. Lyanda-Geller, and G. E. Pikus, "Spin polarization of electrons by an electric current," *Sov. Phys. JETP*, vol. 73, p. 537, 1991.

[10] J. B. Gunn, "Microwave oscillations of current in III-V semiconductors," *Solid State Commun.*, vol. 1, p. 88, 1963.

[11] Z. I. Alferov, V. M. Andreev, M. B. Kagan, I. I. Protasov, and V. G. Trofim, "Solar-energy converters based on p-n $Al_xGa_{1-x}As$ - GaAs heterojunctions," *Sov. Phys. Semicond.*, vol. 4, p. 2047, 1971.

[12] R. N. Hall, G. E. Fenner, J. D. Kingsley, T. J. Soltys, and R. O. Carlson, "Coherent light emission from GaAs junctions," *Phys. Rev. Lett.*, vol. 9, p. 366, 1962.

[13] L. Vegard, "Die konstitution der mischkristalle und die raumfüllung der atome," *Z. Phys.*, vol. 94, p. 5, 1921.

[14] S. R. Lee, A. F. Wright, M. H. Crawford, G. A. Petersen, J. Han, and R. M. Biefeld, "The band-gap bowing of $Al_xGa_{1-x}n$ alloys," *App. Phys. Lett.*, vol. 74, p. 3344, 1999.

[15] C. Kittel, *Introduction to Solid State Physics.* John Wiley and Sons, Inc., 1996.

[16] P. Löwdin, "On the non-orthogonality problem connected with the use of atomic wave functions in the theory of molecules and crystals," *J. Chem. Phys.*, vol. 18, p. 365, 1950.

[17] J. Singh, *Electronic and Optoelectronic Properties of Semiconductor Structures.* Cambridge University Press, 2003.

[18] J. C. Slater and G. F. Koster, "Simplified lcao method for the periodic potential problem," *Phys. Rev.*, vol. 94, p. 1498, 1954.

[19] J. M. Luttinger and W. Kohn, "Motion of electrons and holes in perturbed fields," *Phys. Rev.*, vol. 97, p. 869, 1955.

[20] E. Merzbacher, *Quantum Mechanics.* John Wiley & Sons, Inc., 1998.

[21] B. P. Zakharchenya, V. G. Fleisher, R. I. Dzhioev, Y. P. Veshchunov, and I. B. Rusanov, "Effect of optical orientation of electron spins in a GaAs crystal," *JETP Lett.*, vol. 13, p. 137, 1971.

[22] F. Meier and B. P. Zakharchenya, eds., *Optical Orientation.* Elsevier, 1984.

[23] B. Pursley, M. Luengo-Kovac, G. Vardar, R. S. Goldman, and V. Sih, "Spin lifetime measurements in GaAsBi thin films," *Appl. Phys. Lett.*, vol. 102, p. 022420, 2013.

[24] C. J. Trowbridge. Ph.D. thesis, University of Michigan, 2015.

[25] N. W. Ashcroft and N. D. Mermin, *Solid State Physics.* Brooks/Cole, 1976.

[26] M. Dressel and G. Grüner, *Electrodynamics of Solids.* Cambridge University Press, 2002.

[27] P. Lawaetz, "Valence-band parameters in cubic semiconductors," *Phys. Rev. B*, vol. 4, pp. 3460–3467, 1971.

[28] A. Yariv and P. Yeh, *Optical Waves in Crystals.* John Wiley & Sons, Inc., 1984.

[29] S. John, C. Soukoulis, M. H. Cohen, and E. N. Economou, "Theory of electron band tails and the urbach optical-absorption edge," *Phys. Rev. Lett.*, vol. 57, pp. 1777–1780, 1986.

[30] A. G. Aronov and E. L. Ivchenko, "Dichroism and optical anisotropy of media with oriented spins of free electrons," *Sov. Phys. Solid State*, vol. 15, p. 160, 1973.

[31] D. D. Awschalom and M. E. Flatté, "Challenges for semiconductor spintronics," *Nature Physics*, vol. 3, p. 153, 2007.

[32] W. Zawadzki, P. Pfeffer, R. Braschitsch, Z. Chen, S. T. Cundiff, and B. N. Murdin, "Temperature dependence of the electron g factor in GaAs," *Phys. Rev. B*, vol. 78, p. 245203, 2008.

[33] Y. Kato, R. C. Myers, A. C. Gossard, and D. D. Awschalom, "Coherent spin manipulation without magnetic fields in strained semiconductors," *Nature*, vol. 427, p. 50, 2004.

[34] I. Stepanov, S. Kuhlen, M. Ersfeld, M. Lepsa, and B. Beschoten, "All-electrical time-resolved spin generation and spin manipulation in n-InGaAs," *Appl. Phys. Lett.*, vol. 104, p. 062406, 2014.

[35] G. Dresselhaus, "Spin-orbit coupling effects in zinc blende structures," *Phys. Rev.*, vol. 100, p. 580, 1955.

[36] B. M. Norman, C. J. Trowbridge, J. Stephens, A. C. Gossard, D. D. Awschalom, and V. Sih, "Mapping spin-orbit splitting in strained (In,Ga)As epilayers," *Phys. Rev. B*, vol. 82, p. 081304(R), 2010.

[37] Y. A. Bychov and E. I. Rashba, "Oscillatory effects and the magnetic susceptibility of carriers in inversion layers," *J. Phys. C*, vol. 17, p. 6039, 1984.

[38] G. C. La Rocca, N. Kim, and S. Rodriguez, "Effect of uniaxial stress on the electron spin resonance in zinc-blende semiconductors," *Phys. Rev. B*, vol. 38, p. 7595, 1988.

[39] B. A. Bernevig and S.-C. Zhang, "Spin splitting and spin current in strained bulk semiconductors," *Phys. Rev. B*, vol. 72, p. 115204, 2005.

[40] B. A. Bernevig, J. Orenstein, and S.-C. Zhang, "Exact SU(2) symmetry and persistent spin helix in a spin-orbit coupled system," *Phys. Rev. Lett.*, vol. 97, p. 236601, 2006.

[41] N. S. Averkiev and L. E. Golub, "Giant spin relaxation anisotropy in zinc-blende heterostuctures," *Phys. Rev. B*, vol. 60, p. 15582, 1999.

[42] F. Bloch, "Nuclear induction," *Phys. Rev.*, vol. 70, p. 460, 1946.

[43] E. Y. Tsymbal and I. Ẑutić, eds., *Handbook of Spin Transport and Magnetism*. CRC Press, 2012.

[44] A. D. Margulis and V. A. Margulis, "Spin relaxation of conduction electrons in semiconductors in a strong magnetic field. the precession mechanism," *Sov. Phys. Solid State*, vol. 25, p. 918, 1983.

[45] M. W. Wu and C. Z. Ning, "A novel mechanism for spin dephasing due to spin-conserving scatterings," *Eur. Phys. J. B*, vol. 18, p. 373, 2000.

[46] E. L. Hahn, "Spin echoes," *Phys. Rev.*, vol. 80, p. 580, 1950.

[47] M. I. D'yakonov and V. I. Perel', "Spin relaxation of conduction electrons in noncentrosymmetric semiconductors," *Sov. Phys. Solid State*, vol. 13, p. 3023, 1971.

[48] F. Meier and B. P. Zakharchenya, eds., *Optical Orientation*. Amsterdam: Elsevier Science, 1984.

[49] J. Fabian and S. Das Sarma, "Spin relaxation of conduction electrons," *JVST B*, vol. 17, p. 1708, 1999.

[50] R. J. Elliot, "Theory of the effect of spin-orbit coupling on magnetic resonance in some semiconductors," *Phys. Rev.*, vol. 96, p. 266, 1954.

[51] Y. Yafet, *Solid State Physics: g Factors and spin-lattice relaxation of conduction electrons*. Academic Press Inc., 1963.

[52] K. Shen, R. Raimondi, and G. Vignale, "Theory of coupled spin-charge transport due to spin-orbit interaction in inhomogeneous two-dimensional electron liquids," *Phys. Rev. B*, vol. 90, p. 245302, 2014.

[53] Y. Ohno, D. K. Young, B. Beschoten, F. Matsukura, H. Ohno, and D. D. Awschalom, "Electrical spin injection in a ferromagnetic semiconductor heterostructure," *Nature*, vol. 402, p. 790, 1999.

[54] H. J. Zhu, M. Ramsteiner, H. Kostial, M. Wassermeier, H.-P. Schönherr, and K. H. Ploog, "Room-temperature spin injection from Fe into GaAs," *Phys. Rev. Lett*, vol. 87, p. 016601, 2001.

[55] B. T. Jonker, G. Kioseoglou, A. T. Hanbicki, C. H. Li, and P. E. Thompson, "Electrical spin-injection into silicon from a ferromagnetic metal/tunnel barrier contact," *Nature Physics*, vol. 3, p. 542, 2007.

[56] A. T. Hanbicki, O. M. J. van 't Erve, R. Magno, G. Kioseoglou, C. H. Li, B. T. Jonker, G. Itskos, R. Mallory, M. Yassar, and A. Petrou, "Analysis of the transport process providing spin injection through an Fe/AlGaAs Schottky barrier," *Appl. Phys. Lett.*, vol. 82, p. 4092, 2003.

[57] O. M. J. van 't Erve, G. Kioseoglou, A. T. Hanbicki, C. H. Li, B. T. Jonker, R. Mallory, M. Yassar, and A. Petrou, "Comparison of Fe/Schottky and Fe/Al_2O_3 tunnel barrier contacts for electrical spin injection into GaAs," *Appl. Phys. Lett.*, vol. 84, p. 4334, 2004.

[58] D. Awschalom and N. Samarth, "Spintronics without magnetism," *Physics*, vol. 2, p. 50, 2009.

[59] E. I. Rashba, "Theory of electrical spin injection: Tunnel contacts as a solution of conductivity mismatch problem," *Phys. Rev. B*, vol. 62, p. R16267(R), 2000.

[60] K. J. Thomas, J. T. Nicholls, M. Y. Simmons, M. Pepper, D. R. Mace, and D. A. Ritchie, "Possible spin polarization in a one-dimensional electron gas," *Phys. Rev. Lett.*, vol. 77, p. 135, 1996.

[61] P. Debray, S. M. S. Rahman, J. Wan, R. S. Newrock, M. Cahay, A. T. Ngo, S. E. Ulloa, S. T. Herbert, M. Muhammad, and M. Johnson, "All-electrical quantum point contact spin-polarizer," *Nature Nanotechnology*, vol. 4, p. 759, 2009.

[62] M. I. D'yakonov and V. I. Perel', "Possibility of orienting electron spins with current," *Sov. Phys. JETP Lett.*, vol. 13, p. 467, 1971.

[63] Y. K. Kato, R. C. Myers, A. C. Gossard, and D. D. Awschalom, "Current-induced spin polarization in strained semiconductors," *Phys. Rev. Lett.*, vol. 93, p. 176601, 2004.

[64] V. Sih, W. H. Lau, R. C. Myers, V. R. Horowitz, A. C. Gossard, and D. D. Awschalom, "Generating spin currents in semiconductors with the spin Hall effect," *Phys. Rev. Lett*, vol. 97, p. 096605, 2006.

[65] W. Y. Choi, H.-J. Kim, J. Chang, S. H. Han, H. C. Koo, and M. Johnson, "Electrical detection of coherent spin precession using the ballistic intrinsic spin Hall effect," *Nature Nanotechnology*, vol. 10, p. 666, 2015.

[66] V. Sih, R. C. Myers, Y. K. Kato, W. H. Lau, A. C. Gossard, and D. D. Awschalom, "Spatial imaging of the spin Hall effect and current-induced polarization in two-dimensional electron gases," *Nat. Phys.*, vol. 1, p. 31, 2005.

[67] C. L. Yang, H. T. He, L. Ding, L. J. Cui, Y. P. Zeng, J. N. Wang, and W. K. Ge, "Spectral dependence of spin photocurrent and current-induced spin polarization in an InGaAs/InAlAs two-dimensional electron gas," *Phys. Rev. Lett.*, vol. 96, p. 186605, 2006.

[68] W. F. Koehl, M. H. Wong, C. Poblenz, B. Swenson, U. K. Mishra, J. S. Speck, and D. D. Awschalom, "Current-induced spin polarization in galllium nitride," *Appl. Phys. Lett.*, vol. 95, p. 072110, 2009.

[69] N. P. Stern, S. Ghosh, G. Xiang, M. Zhu, N. Samarth, and D. D. Awschalom, "Current-induced polarization and the spin Hall effect at room temperature," *Phys. Rev. Lett.*, vol. 97, p. 126603, 2006.

[70] R. L. Field III. Ph.D. thesis, University of Michigan, 2015.

[71] B. Norman. Ph.D. thesis, University of Michigan, 2014.

[72] S. Kuhlen, R. Ledesch, R. de Winter, M. Althammer, S. T. B. Gönnenwein, M. Opel, R. Gross, T. A. Wassner, M. S. Brandt, and B. Beschoten, "Unambiguous determination of spin dephasing times in ZnO by time-resolved magneto-optical pump-probe experiments," *Phs. Status Solidi B*, vol. 251, pp. 1861–1871, 2014.

[73] C. J. Trowbridge and V. Sih, "Phase effects due to previous pulses in time-resolved faraday rotation measurements," *J. Appl. Phy.*, vol. 117, p. 063906, 2015.

[74] J. M. Kikkawa and D. D. Awschalom, "Resonant spin amplification of n-type GaAs," *Phys. Rev. Lett.*, vol. 80, p. 4313, 1998.

[75] J. M. Kikkawa and D. D. Awschalom, "Lateral drag of spin coherence in gallium arsenide," *Nature*, vol. 397, p. 139, 1999.

[76] D. Chattopadhyay and H. J. Queisser, "Electron scattering by ionized impurities in semiconductors," *Rev. Mod. Phys.*, vol. 53, p. 745, 1981.

[77] M. Luengo-Kovac, M. Macmahon, S. Huang, R. S. Goldman, and V. Sih, "g-factor modification in a bulk InGaAs epilayer by an in-plane electric field," *Phys. Rev. B*, vol. 91, p. 201110(R), 2015.

[78] F. H. L. Koppens, C. Buizert, K. J. Tielrooij, I. T. Vink, K. C. Nowack, T. Meunier, L. P. Kouwenhoven, and L. M. K. Vandersypen, "Driven coherent oscillations of a single electron spin in a quantum dot," *Nature*, vol. 442, p. 766, 2006.

[79] M. Schulte, J. G. S. Lok, G. Denninger, and W. Dietsche, "Electron spin resonance on a two-dimensional electron gas in a single AlAs quantum well," *Phys. Rev. Lett.*, vol. 94, p. 137601, 2005.

[80] K. C. Nowack, F. H. L. Koppens, Y. V. Nazarov, and L. M. K. Vandersypen, "Coherent control of a single electron spin with electric fields," *Science*, vol. 318, p. 1430, 2007.

[81] G. Salis, Y. Kato, K. Ensslin, D. C. Driscoll, A. C. Gossard, and D. D. Awschalom, "Electrical control of spin coherence in semiconductor nanostructures," *Nature*, vol. 414, p. 619, 2001.

[82] R. S. Deacon, Y. Kanai, S. Takahashi, A. Oiwa, K. Yoshida, K. Shibata, K. Hirakawa, Y. Tokura, and S. Tarucha, "Electrically tuned g tensor in an InAs self-assembled quantum dot," *Phys. Rev. B.*, vol. 84, p. 041302(R), 2011.

[83] Y. S. Chen, S. Fält, W. Wegscheider, and G. Salis, "Unidirectional spin-orbit interaction and spin-helix state in a (110)-oriented GaAs/(Al,Ga)As quantum well," *Phys. Rev. B*, vol. 90, p. 121304(R), 2014.

[84] M. Studer, M. P. Walser, S. Baer, H. Rusterholz, S. Schön, W. W. D. Schuh, K. Ensslin, and G. Salis, "Role of linear and cubic terms for drift-induced Dresselhaus spin-orbit splitting in a two-dimensional electron gas," *Phys. Rev. B*, vol. 82, p. 235320, 2010.

[85] C. J. Trowbridge, B. M. Norman, Y. K. Kato, D. D. Awschalom, and V. Sih, "Dynamic nuclear polarization from current-induced electron spin polarization," *Phys. Rev. B*, vol. 90, p. 085122, 2014.

[86] L. Meier, G. Salis, I. Shorubalko, E. Gini, S. Schön, and K. Ensslin, "Measurement of Rashba and Dresselhaus spin-orbit magnetic fields," *Nature Phys.*, vol. 3, p. 650, 2007.

[87] Z. Wilamowski, H. Malissa, F. Schäffler, and W. Jantsch, "g-factor tuning and manipulation of spins by an electric current," *Phys. Rev. Lett.*, vol. 98, p. 187203, 2007.

[88] J. Hübner, S. Döhrmann, D. Hägele, and M. Oestreich, "Temperature-dependent electron Landé g factor and the interband matrix element of GaAs," *Phys. Rev. B.*, vol. 79, p. 193307, 2009.

[89] R. O. Carlson, G. A. Slack, and S. J. Silverman, "Thermal conductivity of GaAs and $GaAs_{1-x}P_x$ laser semiconductors," *J. Appl. Phys.*, vol. 36, p. 505, 1965.

[90] K. Aoki, Y. Okuyama, T. Kobayashi, and K. Yamamoto, "Hot electrons and exciton-electron collision in GaAs under external electric field," *Solid State Commun.*, vol. 25, p. 717, 1978.

[91] E. G. Schubert, E. O. Göbel, Y. Horikoshi, K. Ploog, and H. J. Queisser, "Alloy broadening in photoluminescence spectra of $Al_xGa_{1-x}As$," *Phys. Rev. B*, vol. 30, p. 813, 1984.

[92] J. Shah, A. Pinczuk, H. L. Störmer, A. C. Gossard, and W. Wiegmann, "Electric field induced heating of high mobility electrons in modulation-doped GaAs-AlGaAs heterostructures," *Appl. Phys. Lett.*, vol. 42, p. 55, 1983.

[93] H. Sakaki, K. Hirakawa, J. Yoshino, S. P. Svensson, Y. Sekiguchi, T. Hotta, and S. Nichii, "Effects of electron heating on the two-dimensional magnetotransport in AlGaAs/GaAs heterostructures," *Surf. Sci.*, vol. 142, p. 306, 1984.

[94] K. Hirakawa, M. Grayson, D. C. Tsui, and Ç. Kurdak, "Blackbody radiation from hot two-dimensional electrons in $Al_xGa_{1-x}As$/GaAs heterojunctions," *Phys. Rev. B*, vol. 47, p. 16651(R), 1993.

[95] A. De, C. E. Pryor, and M. E. Flatté, "Electric-field control of a hydrogenic donor's spin in a semiconductor," *Phys. Rev. Lett.*, vol. 102, p. 017603, 2009.

[96] J. van Bree, A. Y. Silov, P. M. Koenraad, and M. E. Flatté, “Spin-orbit-induced circulating currents in a semiconductor nanostructure,” *Phys. Rev. Lett.*, vol. 112, p. 187201, 2014.

[97] V. M. Edelstein, “Spin polarization of conduction electrons induced by electric current in two-dimensional asymmetric electron systems,” *Solid State Comm.*, vol. 73, p. 233, 1990.

[98] A. G. Aranov and Y. B. Lyanda-Geller, “Nuclear electric resonance and orientation of carrier spins by an electric field,” *JETP Lett.*, vol. 50, p. 431, 1989.

[99] S. A. Tarasenko, “Spin orientation of free carriers by dc and high-frequency electric field in quantum wells,” *Physica E*, vol. 40, p. 1614, 2007.

[100] J. M. Kikkawa. Ph.D. thesis, University of California, Santa Barbara, 1997.

[101] V. L. Korenev, “Bulk electron spin polarization generated by the spin Hall current,” *Phys. Rev. B*, vol. 74, p. 041308(R), 2006.

[102] M. Trushin and J. Schliemann, “Anisotropic current-induced spin accumulation in the two-dimensional electron gas with spin-orbit coupling,” *Phys. Rev. B*, vol. 75, p. 155323, 2007.

[103] C. Gorini, A. Maleki, K. Shen, I. V. Tokatly, G. Vignale, and R. Raimondi, “Theory of current-induced spin polarizations in an electron gas,” *arXiv:1702.04887*, 2017.

[104] H.-A. Engel, B. I. Halperin, and E. I. Rashba, “Theory of spin Hall conductivity in n-doped GaAs,” *Phys. Rev. Lett.*, vol. 95, p. 166605, 2005.

[105] V. Sih, H. Knotz, J. Stephens, V. R. Horowitz, A. C. Gossard, and D. D. Awschalom, “Mechanical control of spin-orbit splitting in GaAs and $In_{0.04}Ga_{0.96}As$ epilayers,” *Phys. Rev. B*, vol. 73, p. 241316(R), 2006.